Utrecht University, the Netherlands
Faculty of Science
Institute of Theoretical Physics

Master's Thesis

Topological Superconductivity in Rashba Superlattices

Student:
Barbara Ferretti

Supervisors:
Dr. Carmine Ortix
Dr. Niccolò Scopigno

December 9, 2018

Utrecht University

Abstract

Recent studies have shown that low dimensional semiconducting nanomaterials with a non trivial geometry possess interesting topological properties. In fact, as a consequence of the curved geometry, non trivial insulating phases can arise in those systems.
In this thesis we analyse the influence of the curvature properties on the topological superconducting phase. We start by considering a model designed to reproduce topological superconductivity in a straight 1D semiconducting nanowire. Superconductivity is induced by proximity with a conventional superconductor and the presence of Rashba spin orbit coupling and an external magnetic field in orthogonal directions allows for the realization of a topological superconducting phase in the semiconductor. Consequently, we analyse the dynamical properties of an electron moving in a curved nanowire, showing that they result in a local spin orbit coupling, inducing a local canting of the electron spin. Finally, we study the robustness of the topological phase of the system against the perturbation introduced by the curvature, and we find that the topological phase is suppressed as a result of the presence of the local spin orbit coupling.

Contents

Chapter 1

Introduction

1.1 Topological states of Matter

Quantum theory of matter predicts the existence of a great variety of phases such as superconductivity, superfluidity, ferromagnetism, charge density waves and many others. These phases can be explained by the phenomenological Landau-Ginzburg theory for phase transitions which implies the existence of a local order parameter that changes from zero to a finite value when the system is driven in the higher ordered phase (an example is the magnetization in the case of a ferromagnet).
However, the discovery of the integer Quantum Hall Effect (QHE) in 1980 [1] paved the way for the study of new phases of matter which do not seem to find an explanation in the framework of the Landau-Ginzburg theory, the *topological phases*.
The integer QHE occurs when electrons are confined to move in a two dimensional surface in presence of an external magnetic field perpendicular to that surface.

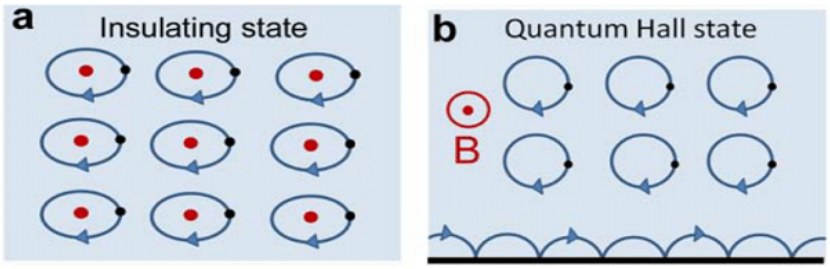

Figure 1.1: The figure on the left shows a trivial atomic insulator, whereas the figure on the right shows the Hall state, in which we see that the particle localized at the edge and constrained to rotate clockwise by the magnetic field, are bounced back by the edge and therefore are circulating counterclockwise along the edges of the 2D material. Considering only one isolated edge, we have a 1D system with only one chiral mode, which cannot be obtained in a conventional one dimensional wire. This figure has been taken from [2]

As shown in picture 1.1, the difference between a conventional insulator and the QH state is manifested at the edges of the system. In fact, as a typical insulator, the integer QH has a gap in the bulk spectrum separating the highest occupied and the lowest empty energy levels, but it has gapless states at the edges. We can take the preceding as a first definition of a topological material implying that the latter is a material with a gapped bulk spectrum (like an insulator or a superconductor) and conducting edges. The concept of topological ordered states of matter was firstly introduced by Kosterlitz and Thouless in [3, 4] and, later, Thouless, Kohmoto Nightingale and den Nijs (TKNN) derived the quantized Hall conductance by means of topological considerations [5].
As the name already suggests, there is a deep connection between topological states of matter and the bunch of mathematics called topology. In mathematical topology, two topological spaces are

said to be equivalent if they can be *continuously deformed* one into the other [6]. For example, a ball can be continuously deformed into a pot, but it cannot be deformed into a doughnut without cutting a hole in it , whereas the latter can be continuously deformed into a mug. In topology, the continuous deformation that divides the topological spaces into equivalence classes is called *homeomorphism* and the quantity which is invariant under homeomorphism goes under the name of ***topological invariant***. It follows that if two spaces have different topological invariant, they belong to two different topological classes.
In the same way topological spaces are insensitive to smooth transformations, the properties of a topological phase of matter do not depend on the local smooth variation of the parameters of the system: the system does not change unless it undergoes a topological phase transition.
That is, the QH state cannot be driven into a trivial insulating phase by smoothly changing the parameters in the Hamiltonian describing the system. These topologically distinct phases of the system are individuated by the topological invariant which is determined by the symmetries of the system and it can be individuated by looking at the bulk band spectrum only [7, 8]. This remarkable property that allows one to establish the presence or absence of conducting edge states by having informations only regarding the bulk of the system, goes under the name of ***bulk-edge correspondence*** [9, 10].

Ever since their discovery, topological materials have been studied intensively. The main reason is that the conducting states situated at the edge (or surface for a three dimensional material) exhibit unique properties that arise from these states being at the boundary of a higher dimensional material, and which cannot be recovered in a purely 1D or 2D system. In the QH state for example, each one dimensional edge, hosts one chiral mode, moving in one direction. In a purely one dimensional system, it is not possible to have only one chiral state as for each Fermi energy one always has two chiral (left and right-moving) states. These exotic properties of the boundary states have opened up the way for engineering new technologically advanced materials[11, 12]. Of particular interest, are the zero energy excitation arising at the boundaries of topological superconducting materials [13, 14, 15], which can potentially be the new frontier for topological quantum computation[16, 17].

1.2 Majorana Modes in Condensed Matter

In relativistic quantum field theory, fermions are described by the Dirac equation

$$(i\gamma^\mu \partial_\mu - m)\psi = 0 \tag{1.1}$$

where the index $\mu = 0, 1, 2, 3$, and the matrices $\gamma^{\mu\nu}$, obeying the anticommutation relation $\{\gamma^\mu, \gamma^\nu\} = 2g^{\mu\nu}$(with $g^{\mu\nu}$ Minkowski metric), have complex elements. The general solutions of the equation $\psi(x)$ are complex Dirac spinors which are not symmetric under charge conjugation. In fact, since charge conjugation operator sends $\psi \to \psi^*$, (that is, it sends a particle in its antiparticle: a particle with same mass and spin but opposite charge), eigenstates of the charge conjugation must be real solutions of the 1.1.
The Majorana particles are defined as particles which are their own antiparticles. Thus, they are individuated as real solutions of the Dirac equation. Although Majorana introduced the concept almost one century ago, chargeless fermions are still central topic in modern high energy physics research, and in the last decades, Majorana's idea started being explored also in solid states systems by condensed matter physicists.
However, unlike Majorana particles in high energy physics, the ones pursued in condensed matter are not fundamental particles (as the fundamental constituents of a solid system are electrons and ions) but rather quasiparticles excitations over a many-body system ground state [18].

The quasiparticles excitation of a superconducting ground state, the Bogoliubov quasiparticles, are a superposition of opposite charges: for this reason, superconducting systems are regarded as natural grounds for pursuing Majorana quasiparticles in solid states systems. Nevertheless, the operator annihilating a Bogoliubov quasiparticles in conventional superconductors (the microscopic theory for those superconductors is the well-known BCS theory) is $\gamma = uc^\dagger_\uparrow + vc_\downarrow$,

which is physically distinct from $\gamma^\dagger = v^* c_\downarrow^\dagger + u^* c_\uparrow$ as in fact Cooper pairing occurs between electrons carrying opposite spin (note that the pairing in conventional superconductors is referred to as s- wave pairing since, as the electrons are paired up in a singlet state, the spatial wavefunction in symmetric).
In order to circumvent this problem, one needs then to consider electronic systems with only one active spin projection, or 'spinless' systems . Superconducting pairing in those systems must occur with antisymmetric spatial wavefunction due to Pauli exclusion principle, which results into p-wave and, possibly, in $p_x + ip_y$ superconductivity in one and two dimensions respectively. Those superconductors are special, as they manifest topological superconductivity, with zero energy modes at their boundaries (ends for 1D superconductors) and topological defects [15].
Indeed, if Majorana modes are to appear in such a 'spinless' superconductor, they have to be zero energy Bogoliubov excitations as Bogoliubov quasiparticles operators are still symmetric under particle-hole, that is $\gamma_E^\dagger = \gamma_{-E}$ (creating a particle at energy E is identical to annihilate a hole at energy -E), which constrains the Majorana modes to zero energy, with $\gamma_0^\dagger = \gamma_0$ and $\gamma_0^2 = 1$.
Therefore, Majorana modes (or Majorana quasipartciles excitations) are chargeless, spinless and massless excitations, localised at the boundaries of the topological superconductor.
We have introduced the Majorana operators, but we have not mentioned an important part of the story yet. Indeed, in order to obtain a usual fermionic operator with a well-defined occupation number, we need to combine two of the Majorana operators above: $f = \frac{1}{2}(\gamma_1 + i\gamma_2)$ (we omitted the subscript zero as it is clear now that the operators refer to the zero energy modes), thus Majorana modes should be rather regarded as 'half' a fermion.
Despite being a regular fermionic operator, f is quite special since the two modes combining into a fermion can be situated very far apart, yielding a highly non-local fermion, and, if that is the case, the ground state of the system is two-fold degenerate as one can add or remove this fermion to the system with no energy cost.
The non-locality of the fermionic state also leads to another fundamental characteristics: the 'topological protection'. The zero-energy fermionic state is immune to any local perturbation (i.e perturbations that do not couple the two Majorana modes), and the two modes stay localised at the boundaries as long as the system is in its topological phase, that is, as long as the superconducting bulk gap stays open.
Furthermore, it has been shown that the zero energy modes obey non-Abelian statistics [19], which highly increased the interest in probing Majorana modes, since non-Abelian anyons are regarded as potential elementary units of fault tolerant quantum computation [20].

Given the high interest in the field and the astonishing consequences that observation of Majorana end modes would have, much effort has been put in designing systems which can host Majorana fermions[21, 22]. Among all, it has been proved that two dimensional semiconducting thin films and one dimensional semiconducting nanowires with external applied magnetic field and s-wave superconductivity induced by proximity, can host Majorana fermions at their boundaries and defect (e.g the impurities for electron or hole-doped semiconductors)[23]. As we shall see later on in the thesis, in order to obtain topological superconductivity in such structures, the spin orbit coupling in semiconductors plays a crucial role.
In this thesis, we will be concerned with Majorana modes emerging in the topological phase of the 1D superconductor-semiconductor heterostructure.

1.3 Nanomaterials with non Trivial Geometry

A primary role in the designing of topological materials, is played by semiconducting nanomaterials in low dimensions [24, 25, 26]. In the last decades, the progress in nanostructuring techniques, has allowed to engineer new nanostructures with complex curved geometric shapes like nanotubes or nanohelics, like the ones showed in 1.2 which retain many potential applications in nanoelectronics [27, 28, 29]. Furthermore, semiconducting nanostructures with non

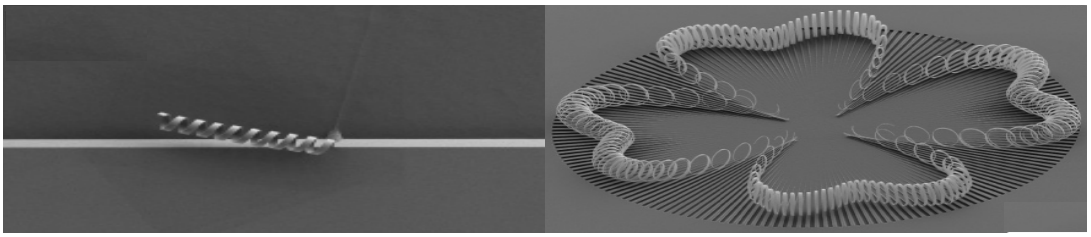

Figure 1.2: Figure shows examples of curved nanostructures that can be engineered in nowadays nanoelectronics. The images have been taken by Zhang et al. Nano Letters 6, 1311 (2006).

trivial geometry, are considered as suitable candidates for being employed in biological system [30]. As a consequence of the growing interest on these semiconducting materials, in recent years, their electronic properties have been studied, and it has been shown that the quantum mechanical properties of electrons confined in a curved low dimensional material can influence the topology of the ground state of the system [31].
A legitimate question that arises, concerns therefore the influence of the curvature induced transport properties of the electrons in the semiconducting wire, and the topological superconducting phase hosting Majorana zero modes at the ends.

1.4 In this thesis

The purpose of this thesis is to attempt to answer the question proposed above, in particular we propose to verify if the topological phase of the system is robust against the local perturbation induced in real space by a 1D semiconducting system in a curved geometry.

The structure of this thesis is the following. In chapter two we revise the fundamental model for a one dimensional topological superconductor: the Kitaev chain. In order to fully understand the model, we firstly recall the BCS theory for a conventional superconductor. Furthermore, we add some basic notions on topological classes and topological invariants to be able to show that in the Kitaev model there are two distinct superconducting phases: the trivial phase (characterised by a certain topological invariant) and the topological phase (characterised by a different topological invariant).
In order to experimentally reproduce the topological superconducting phase predicted in the theoretical Kitaev model, many systems have been engineered. Among those, we focus on the one introduced in [23]. In the last part of chapter two, we therefore provide a detailed analysis of the features of this model, since the work done in this thesis is based on the latter. In fact, in this model, topological superconductivity is obtained in a 'conventional' semiconducting nanowire, where with conventional we mean that the wire is thought to have a trivial geometric shape. Therefore, our work consists in considering a bent nanowire rather than straight, and analyse the interplay of the curvature in real space and the topological order of the system.
In chapter three we thus derive the effective one dimensional Hamiltonian describing the motion of the electron in the curved semiconducting wire in presence of spin orbit coupling (SOC), showing that it leads to a local canting of the electron spins due to the curvature induced locally varying SOC. Given its important role in the description of the system, we dedicate the first part of chapter three to revise the origin of spin orbit coupling and to discuss the SOC in semiconductors.
Finally, the last two chapters of the thesis, will be devoted to the study of the stability of the topological superconducting phase of the model introduced in chapter two, against the perturbation introduced by the curved shape of the wire. As mentioned above, the effect of the curvature, can be incorporated in the effective 1D Hamiltonian by including a local SOC. Therefore, in chapter four, we first consider a simplified 'toy' model to better understand the effect of a modulated SOC. In this model, the semiconducting wire has a trivial geometric shape, and the locally varying SOC is introduced by externally modulating the electric field generating the

SOC. In chapter five, we then proceed with the analysis of the model with a curved nanowire, for which we choose a periodic serpentine-like shape.

Chapter 2

From Conventional Superconductivity to Majorana End Modes

.

2.1 Superconductivity

It was April 1911 when Kammerlingh Onnes found that the resistivity of Mercury (Hg) when cooled down at 4 K drops to zero [32]. Electrical resistivity dropping to zero at low temperatures, the existence of persistent currents (i.e currents circulating without energy dissipation) and the expulsion of the magnetic flux from the bulk of the material (also called *perfect diamagnetism*) in many kinds of metals (or alloys) are the hallmark of superconductivity.
The superconducting phase of the system, realised below a critical temperature T_c, is characterised by a long range phase coherence of the macroscopic ground state wave function, robust to any local perturbation.

The first theory succeeding in explaining what is now called *conventional superconductivity* or *s-wave superconductivity* was formulated in 1957 by Bardeen-Cooper-Schrieffer, and, named after its creators, it is renown as BCS theory of superconductivity.
The BCS theory describes a many body system and it includes the interactions among electrons by making use of the mean field approximation, as we shall briefly see in what follows.
The starting point of BCS theory is the Cooper problem. Basing his analysis on Frölich and Bardeen's work, Cooper analysed the spectrum of a pair of electrons interacting attractively, above a quiescent Fermi sphere [33]. The latter forbids the scattering of the electron pairs in states with momenta $k < k_F$ smaller than the Fermi momentum. From his study, Cooper concluded that, among the possible final states of the process, there is a low energy state being a bound state between the two electrons. The Fermi sphere is thus unstable towards the formation of such electron pairs.

The starting point to investigate a system involving a macroscopic number of electron pairs is the BCS Hamiltonian

$$H_{BCS} = \sum_{\boldsymbol{k},\sigma} \epsilon_{\boldsymbol{k}} c^{\dagger}_{\boldsymbol{k},\sigma} c_{\boldsymbol{k},\sigma} + \sum_{\boldsymbol{k},\boldsymbol{k}'} V_{\boldsymbol{k},\boldsymbol{k}'} c^{\dagger}_{\boldsymbol{k}',\uparrow} c^{\dagger}_{-\boldsymbol{k}'\downarrow} c_{-\boldsymbol{k},\downarrow} c_{\boldsymbol{k},\uparrow} \tag{2.1}$$

where the operators $c^{\dagger}_{\boldsymbol{k},\sigma}$ and $c_{\boldsymbol{k},\sigma}$ are fermionic creation and annihilation operators. Note the interaction term in the above involves scattering between time-reversed states, as the initial (and consequently final) states have opposite momenta and opposite spins. In 2.1, the matrix elements $V_{k,k'}$ are negative and non vanishing only in the interval $\epsilon_F \pm \omega_D$. For simplicity we furthermore assume the interaction coupling to be constant, setting $V_{k,k'} = -V_0$ in the whole range $\epsilon_F \pm \omega_D$.
In order to decouple the quartic interaction term, we then proceed via mean field approximation,

defining the order parameter Δ through the expectation value of electron pairs on the ground state as

$$\begin{aligned}\Delta &= -\sum_{\boldsymbol{k}} V_0 \langle c_{-\boldsymbol{k},\downarrow} c_{\boldsymbol{k},\uparrow} \rangle \\ \Delta^* &= -\sum_{\boldsymbol{k}} V_0 \langle c^\dagger_{\boldsymbol{k},\uparrow} c^\dagger_{-\boldsymbol{k},\downarrow} \rangle\end{aligned} \tag{2.2}$$

where, as said above, V_0 is only non-zero in the ring $\epsilon_F \pm \omega_D$. Thus we can write the pair creation and annihilation operators as their mean value plus small fluctuations $\delta_{c_{-\boldsymbol{k},\downarrow} c_{\boldsymbol{k},\uparrow}}$ as

$$\begin{aligned}c_{-\boldsymbol{k},\downarrow} c_{\boldsymbol{k},\uparrow} &= \langle c_{-\boldsymbol{k},\downarrow} c_{\boldsymbol{k},\uparrow} \rangle + \delta_{c_{-\boldsymbol{k},\downarrow} c_{\boldsymbol{k},\uparrow}} \\ c^\dagger_{\boldsymbol{k}',\uparrow} c^\dagger_{-\boldsymbol{k}',\downarrow} &= \langle c^\dagger_{\boldsymbol{k}',\uparrow} c^\dagger_{-\boldsymbol{k}',\downarrow} \rangle + \delta_{c^\dagger_{\boldsymbol{k}',\uparrow} c^\dagger_{\boldsymbol{k}',\downarrow}}\end{aligned} \tag{2.3}$$

Plugging the 2.3 in 2.1, neglecting second order terms in fluctuations, and then replacing back $\delta_{c_{-\boldsymbol{k},\downarrow} c_{\boldsymbol{k},\uparrow}}$ and $\delta_{c^\dagger_{\boldsymbol{k}',\uparrow} c^\dagger_{\boldsymbol{k}',\downarrow}}$ by inverting relations 2.3, we get the BCS Mean Field Hamiltonian

$$\begin{aligned}H_{BCS} = \sum_{\boldsymbol{k},\sigma} \epsilon_{\boldsymbol{k}} c^\dagger_{\boldsymbol{k},\sigma} c_{\boldsymbol{k},\sigma} + \sum_{\boldsymbol{k}} \Delta c^\dagger_{\boldsymbol{k},\uparrow} c^\dagger_{-\boldsymbol{k},\downarrow} \\ + \sum_{\boldsymbol{k}} \Delta^* c_{-\boldsymbol{k},\downarrow} c_{\boldsymbol{k},\uparrow} - V_0 \sum_{\boldsymbol{k},\boldsymbol{k}'} \langle c^\dagger_{\boldsymbol{k}',\uparrow} c^\dagger_{-\boldsymbol{k}',\downarrow} \rangle \langle c_{-\boldsymbol{k},\downarrow} c_{\boldsymbol{k},\uparrow} \rangle.\end{aligned} \tag{2.4}$$

In the above, the last term is a constant shift in Energy that we will neglect in the following. We are now left with a quadratic Hamiltonian, which is nevertheless non diagonal in particle creation and annihilation operators in momentum space.
The 2.4 is known as **Bogoliubov-de Gennes Hamiltonian** (or **Bogoliubov Gor'kov** in Russian literature).
We can write the equation in matrix form as follows

$$H_{BdG} = \sum_{\boldsymbol{k}} \begin{pmatrix} c^\dagger_{\boldsymbol{k},\uparrow} & c_{-\boldsymbol{k},\downarrow} \end{pmatrix} \begin{pmatrix} \epsilon_{\boldsymbol{k}} & \Delta \\ \Delta^* & -\epsilon_{\boldsymbol{k}} \end{pmatrix} \begin{pmatrix} c_{\boldsymbol{k},\uparrow} \\ c^\dagger_{-\boldsymbol{k},\downarrow} \end{pmatrix}.$$

Introducing Nambu Spinor notation

$$\boldsymbol{\Psi}^\dagger_{\boldsymbol{k}} = \begin{pmatrix} c^\dagger_{\boldsymbol{k},\uparrow} & c_{-\boldsymbol{k},\downarrow} \end{pmatrix}, \boldsymbol{\Psi}_{\boldsymbol{k}} = \begin{pmatrix} c_{\boldsymbol{k},\uparrow} \\ c^\dagger_{-\boldsymbol{k},\downarrow} \end{pmatrix},$$

we finally write the equation in the compact form

$$H_{BdG} = \sum_{\boldsymbol{k}} \boldsymbol{\Psi}^\dagger_{\boldsymbol{k}} \boldsymbol{H}_{\boldsymbol{k}} \boldsymbol{\Psi}_{\boldsymbol{k}}. \tag{2.5}$$

The aim now is to diagonalize this Hamiltonian. In order to do so, we introduce the new operators $\alpha_{\boldsymbol{k}}$ and $\alpha^\dagger_{\boldsymbol{k}}$ and a canonical transformation which goes under the name of Bogoliubov transformation (as he first applied this transformation for bosonic operator in his treatment of super fluid Helium). The transformation in terms of those operators reads

$$\begin{pmatrix} \alpha_{\boldsymbol{k},\uparrow} \\ \alpha^\dagger_{-\boldsymbol{k},\downarrow} \end{pmatrix} = \begin{pmatrix} u^*_{\boldsymbol{k}} & v_{\boldsymbol{k}} \\ -v^*_{\boldsymbol{k}} & u_{\boldsymbol{k}} \end{pmatrix} \begin{pmatrix} c_{\boldsymbol{k},\uparrow} \\ c^+_{-\boldsymbol{k},\downarrow} \end{pmatrix}$$

where

$$\begin{pmatrix} u^*_{\boldsymbol{k}} & v_{\boldsymbol{k}} \\ -v^*_{\boldsymbol{k}} & u_{\boldsymbol{k}} \end{pmatrix} = \boldsymbol{U}^{-1}_k.$$

The constants $u_{\boldsymbol{k}}$ and $v_{\boldsymbol{k}}$ are normalised such that $|u_{\boldsymbol{k}}|^2+|v_{\boldsymbol{k}}|^2 = 1$, and therefore $\boldsymbol{U_k}$ is a unitary matrix. In order to diagonalize the matrix $\boldsymbol{H_k}$ we need to introduce a unitary transformation which defines a similarity relation

$$\boldsymbol{U_k^\dagger H_k U_k = D_k} \tag{2.6}$$

with a diagonal matrix $\boldsymbol{D_k}$.
Solving the equation above with little algebra (see appendix A for details on the computation), and taking into account that the eigenvectors are normalised to one, we arrive at the expressions for the eigenvector components $u_{\boldsymbol{k}}$ and $v_{\boldsymbol{k}}$ and the eigenvalues $\lambda_{\boldsymbol{k}}$ of the new diagonal Hamiltonian expressed in terms of the Bogoliubov operators $\alpha_{\boldsymbol{k}}$ and $\alpha^\dagger_{\boldsymbol{k}}$

$$|u_{\boldsymbol{k}}|^2 = \frac{1}{2}\left(1+\frac{\epsilon_{\boldsymbol{k}}}{\lambda_{\boldsymbol{k}}}\right); |v_{\boldsymbol{k}}|^2 = \frac{1}{2}\left(1-\frac{\epsilon_{\boldsymbol{k}}}{\lambda_{\boldsymbol{k}}}\right) \tag{2.7}$$

$$\lambda_{\boldsymbol{k}} = \pm\sqrt{\epsilon_{\boldsymbol{k}}^2+|\Delta|^2} \tag{2.8}$$

$$H_{BdG} = \sum_{\boldsymbol{k}} \lambda_{\boldsymbol{k}}\left(\alpha^\dagger_{\boldsymbol{k},\uparrow}\alpha_{\boldsymbol{k},\uparrow} + \alpha^\dagger_{\boldsymbol{k},\downarrow}\alpha_{\boldsymbol{k},\downarrow}\right) \tag{2.9}$$

With the Hamiltonian in the diagonal form in the new basis, we were able to find the eigenvalues given by 2.8, from which it appears clear that the energy spectrum of the system is now gapped, as no excitations can exist at energies lower than $|\Delta|$.
The Bogoliubov operators $\alpha^\dagger_{\boldsymbol{k}}$ and $\alpha_{\boldsymbol{k}}$ which form a diagonal basis for the Hamiltonian, are respectively creation and annihilation operators of Bogoliubov quasi-particles (sometimes also called Bogoliubons) which produce the excitation spectrum of the BCS ground state, and which are superposition of particles and holes.
The BCS ground state is defined as $\alpha_{\boldsymbol{k}}|\Psi_{\boldsymbol{GS}}\rangle = 0$, since no quasiparticle excitations are assumed to exist in the ground state. The ket $|\Psi_{\boldsymbol{GS}}\rangle = 0$ is given by

$$|\boldsymbol{\Psi_{GS}}\rangle = \prod\nolimits_k \alpha_{\boldsymbol{k},\uparrow}\alpha_{\boldsymbol{-k},\downarrow}|\boldsymbol{\Omega}\rangle \tag{2.10}$$

and $|\boldsymbol{\Omega}\rangle$ is the state annihilated by all the operators $c_{\boldsymbol{k}}$. The excited states are obtained by acting with $\alpha^\dagger_{\boldsymbol{k}}$ on the BCS ground state and they are the result of breaking a Cooper pair, as already mentioned by Cooper in [33].

In order to understand the implications of the energy gap, we have to find an expression for the mean field parameter Δ. This can be done self consistently i.e computing the expectation value on the right hand side of 2.2 in the new diagonal basis [1].
Thus, starting from 2.2 we get

$$\begin{aligned}
\Delta &= -\sum_{\boldsymbol{k}} V_{\boldsymbol{k},\boldsymbol{k}'}\langle c_{\boldsymbol{-k},\downarrow}c_{\boldsymbol{k},\uparrow}\rangle \\
&= -\sum_{\boldsymbol{k}} V_{\boldsymbol{k},\boldsymbol{k}'}\langle(u_{\boldsymbol{k}}\alpha_{\boldsymbol{-k},\downarrow} - v_{\boldsymbol{k}}\alpha^\dagger_{\boldsymbol{k},\uparrow})(u_{\boldsymbol{k}}\alpha_{\boldsymbol{k},\uparrow} + v_{\boldsymbol{k}}\alpha^\dagger_{\boldsymbol{-k},\downarrow})\rangle \\
&= -\sum_{\boldsymbol{k}} V_{\boldsymbol{k},\boldsymbol{k}'}u_{\boldsymbol{k}}v_{\boldsymbol{k}}\left(\langle\alpha_{\boldsymbol{-k},\downarrow}\alpha^\dagger_{\boldsymbol{-k},\downarrow}\rangle - \langle\alpha^\dagger_{\boldsymbol{k},\uparrow}\alpha_{\boldsymbol{k},\uparrow}\rangle\right).
\end{aligned} \tag{2.11}$$

The Bogoliubov quasiparticles obey the Fermi-Dirac distribution, thus we have

$$\begin{aligned}
\Delta &= -\sum_{\boldsymbol{k}} V_{\boldsymbol{k},\boldsymbol{k}'}u_{\boldsymbol{k}}v_{\boldsymbol{k}}\left(1 - \langle\alpha^\dagger_{\boldsymbol{-k},\downarrow}\alpha_{\boldsymbol{-k},\downarrow}\rangle - \langle\alpha^\dagger_{\boldsymbol{k},\uparrow}\alpha_{\boldsymbol{k},\uparrow}\rangle\right) \\
&= -\sum_{\boldsymbol{k}} V_{\boldsymbol{k},\boldsymbol{k}'}u_{\boldsymbol{k}}v_{\boldsymbol{k}}(1-2n_F(\lambda_{\boldsymbol{k}}))
\end{aligned} \tag{2.12}$$

[1] It can be shown indeed that this procedure for finding the mean field parameter is equivalent to minimize the free energy with respect to Δ. [34]

where n_F is the Fermi Dirac distribution corresponding to the energy value $\lambda_{\boldsymbol{k}}$; and

$$2n_F = \frac{2}{\exp\{-\beta\lambda_{\boldsymbol{k}}\}+1} = \frac{\exp\{-\beta\lambda_{\boldsymbol{k}}\}-1}{\exp\{-\beta\lambda_{\boldsymbol{k}}\}+1}.$$

Furthermore, from relations 2.7 we find

$$u_{\boldsymbol{k}}v_{\boldsymbol{k}} = \frac{1}{2}\frac{\Delta}{\sqrt{\epsilon_{\boldsymbol{k}}^2+\Delta^2}}.$$

At this point, we go to the continuum limit, sending the sum over $\boldsymbol{k}_s$ to an integral: $\sum_{\boldsymbol{k}} \to \int D(E)dE$, with $D(E)$ density of states. We recall that the potential $V_{\boldsymbol{k},\boldsymbol{k}'}$ is non zero (and we also assumed it to be constant in this energy range) only in the interval $\epsilon_F \pm \omega_D$. If we also assume the density of states being constant in this interval, the self-consistent equation for Δ reads

$$\Delta = -\frac{\Delta}{2}V_0 D(E_F)\int_{-\omega_D}^{\omega_D}\frac{dE}{\sqrt{\epsilon_{\boldsymbol{k}}^2+\Delta^2}}\left[\frac{\exp\left\{-\beta\sqrt{\epsilon_{\boldsymbol{k}}^2+\Delta^2}\right\}-1}{\exp\left\{-\beta\sqrt{\epsilon_{\boldsymbol{k}}^2+\Delta^2}\right\}+1}\right] \tag{2.13}$$

where $D(E_F)$ is the density of states at the Fermi level. This leads to the gap equation

$$\frac{2}{V_0 D(E_F)} = -\int_{-\omega_D}^{\omega_D}\frac{dE}{\sqrt{\epsilon_{\boldsymbol{k}}^2+\Delta^2}}\tanh\left(-\beta\sqrt{\epsilon_{\boldsymbol{k}}^2+\Delta^2}\right). \tag{2.14}$$

At zero Temperature, the gap equation above becomes

$$\frac{2}{V_0 D(E_F)} = \int_{-\omega_D}^{\omega_D}\frac{dE}{\sqrt{\epsilon_{\boldsymbol{k}}^2+\Delta^2}} = \operatorname{arcsinh}\left(\frac{2\omega_D}{\Delta_0}\right) \tag{2.15}$$

Thus,

$$\Delta_0 = \frac{\omega_D}{\sinh(2/V_0 D(E))}. \tag{2.16}$$

At given temperature and chemical potential, the gap equation can be solved numerically. Setting $\Delta = 0$ and solving for $T = T_C$, one finds the critical temperature for which the transition between the normal and the superconducting phases occurs.

2.2 Topology and the Kitaev Model

In this section, we introduce the Kitaev model, a toy-model for a 1-D chain of spinless electron, which can host Majorana modes at its boundary when the system is in the topological phase.

Before analysing the model in detail, we give a very brief and intuitive explanation of what we mean by *topological phase* of a material, in order to recap some basic notions useful for the understanding of the rest of the thesis.

2.2.1 Discrete Symmetries and Topological Invariants

As mentioned in the introduction, the study of topological states of matter is a central topic in nowadays physics. It is a very broad subject, since it can be studied from many perspectives, and a deep understanding of this field involves both knowledge on mathematical topology and homotopy groups, and physical knowledge on condensed matter systems. The purpose of this section is to give an intuitive idea behind the classification of system Hamiltonians in different topological classes, and how one in practice can derive a criterion (te topological invariant) in order to understand from the bulk band structure if the system undergoes a topological phase transition at a particular point in the parameter space of the Hamiltonian.

Intuitively, in topology, one is interested in understanding if two 'objects' can be continuously deformed (or smoothly connected) one into the other. If that is the case, they are said to be *topologically equivalent*. We need first to define these 'objects' we are interested in, and the equivalence relation between them (i.e we need to define what we mean by 'continuously deformed one into the other'). In quantum many body theory, the 'objects' we considered are Hamiltonians of the many body systems and the equivalence relation between them is the ***adiabatic principle*** [35]. In the adiabatic approximation, a time-dependent Hamiltonian $H(t)$ is assumed to vary on time much slower than the typical quantum oscillations of the system. In this limit of slowly-varying Hamiltonian, the adiabatic theorem states that if the system is in an eigenstate of the Hamiltonian at an initial time t_i , then it will remain in the instantaneous eigenstate of $H(t)$ during all the evolution till t_f.
In Hamiltonians with a gapped spectrum, the ground state is separated by the bulk excitation by means of an energy gap ΔE_0, thus, starting in the ground state of the Hamiltonian, and evolving the system adiabatically, we must remain in the instantaneous ground state.
Considering two gapped Hamiltonians, and taking the adiabatic evolution, we say that these two Hamiltonians are 'smoothly' connected if they can be deformed into the other without closing the energy gap during the adiabatic evolution in parameter space. If these two Hamiltonians are smoothly connected, then they are topologically equivalent.
If that is not the case, the two Hamiltonians are in two different topological phases, and a topological phase transition occurs at the closing of the band gap.
Since the topology is a generic feature of the Hamiltonian and it cannot depend on a particular time evolution in parameter space of the Hamiltonian, in order to identify the occurrence of a topological phase transition, we need a a quantity that changes only when the gap in the energy spectrum closes. This quantity is precisely the topological invariant. The type and the presence of the topological invariant is completely determined by the symmetries of the Hamiltonian, which also allow us to locate the Hamiltonian in different topological classes. For one particle quadratic Hamiltonians, the relevant discrete symmetries for the determination of the topological classes of general random Hamiltonians (and the corresponding topological invariants) are: Time Reversal, Particle-Hole and Chiral (or sublattice) symmetries. The formal derivation of topological invariant and the subsequent classification of the topological classes of the Hamiltonians based on the symmetries they posses will not be examined in details here. We will rather extrapolate the results useful for our future discussion.
Let us start by considering the action of the three symmetries listed above on a Bloch Hamiltonian $H(\boldsymbol{k})$, where $\boldsymbol{k}$ is the Bloch wavevector in the first Brillouin zone.
Time reversal symmetry 'reverses' the arrow of time and, in momentum space, it sends $k \to -k$. It is an anti-unitary transformation, and, as such, its operator is defined as $\boldsymbol{T} = \boldsymbol{U}K$, where K indicates complex conjugation, and $\boldsymbol{U}$ is a general unitary matrix. By computing $\boldsymbol{T}^2 = \boldsymbol{U}K\boldsymbol{U}K = \boldsymbol{U}\boldsymbol{U}^*$ we observe that Time Reversal squares to ± 1. In particular, for particles with spin 1/2, the Time Reversal symmetry operator is defined by $\boldsymbol{T} = i\sigma_y K$ where σ_y is the second Pauli Matrix, and it squares to -1.
Particle-Hole symmetry exchanges particles with holes and it is again an anti-unitary operator. Once again, $\boldsymbol{P}^2 = \pm 1$ and applying Particle-Hole on the momentum space Hamiltonian we obtain $\boldsymbol{P}H(\boldsymbol{k})\boldsymbol{P}^\dagger = -H(-\boldsymbol{k})$.
Pausing here for a moment, we see that, if we have to classify the Hamiltonians basing on $\boldsymbol{T}^2$ and $\boldsymbol{P}^2$ we have 9 possible combinations as $\boldsymbol{T}(\boldsymbol{P}) = 0$ if the Time-Reversal (Particle-Hole) symmetry is absent, or $\boldsymbol{T}(\boldsymbol{P}) = \pm 1$ when the symmetry is present and it squares to either 1 or -1.
We now add the third symmetry, the Chiral, or sublattice, symmetry. Applying the latter on the Bloch Hamiltonian we obtain $\boldsymbol{C}H(\boldsymbol{k})\boldsymbol{C}^\dagger = -H(\boldsymbol{k})$. The Chiral symmetry can be written as a product of the two previous symmetries $\boldsymbol{C} = \boldsymbol{T}\boldsymbol{P}$. It is a unitary symmetry, so we can always re-adjust the phase such that $\boldsymbol{C}^2 = 1$.
Note however that Chiral symmetry can still be present when both Time Reversal and Particle-Hole are broken, adding one more possibility to the previous 9 arising from the combination of Particle-Hole and Time Reversal. This makes it a total of ten different symmetry classes in

	T	P	C	1d	2d	3d	4d	5d	6d	7d	8d
A	0	0	0	0	Z	0	Z	0	Z	0	Z
AIII	0	0	1	Z	0	Z	0	Z	0	Z	0
AI	1	0	0	0	0	0	Z	0	Z_2	Z_2	Z
BDI	1	1	1	Z	0	0	0	Z	0	Z_2	Z_2
D	0	1	0	Z_2	Z	0	0	0	Z	0	Z_2
DIII	-1	1	1	Z_2	Z_2	Z	0	0	0	Z	0
AII	-1	0	0	0	Z_2	Z_2	Z	0	0	0	Z
CII	-1	-1	1	Z	0	Z_2	Z_2	Z	0	0	0
C	0	-1	0	0	Z	0	Z_2	Z_2	Z	0	0
CI	1	-1	1	0	0	Z	0	Z_2	Z_2	Z	0

Table 2.1: Altland-Zirnbauer periodic table. The first column contains the 10 symmetry classes, for each class is indicated the presence or the absence of one of the three symmetry listed in the text, and for T and P it is indicated if they square to 1 or -1. The last eight columns indicate the type of topological invariant (when it exists) for the particular symmetry class in $1, 2, 3...8$ dimension.

which the quadratic random Hamiltonians with a gapped spectrum can be classified.
Those classes and the relative topological invariant, are summarized in the periodic table 2.1. The first classification of the Hamiltonian in those 10 classes was made by Altland and Zirnbauer [36], and Kitaev in 2009 was able to generalize the Altland-Zirnbauer periodic table to arbitrary dimensions [37]. This table is useful for us as, once we know the symmetry of our Hamiltonian, we know if we expect the system to undergo a topological phase transition and which type of topological invariant is associated to that.

2.2.2 Kitaev Model

The tight binding Hamiltonian proposed by Kitaev [38] is

$$H = -\mu \sum_i c_i^\dagger c_i - \frac{1}{2} \sum_i (t c_i^\dagger c_{i+1} + \Delta e^{i\phi} c_i c_{i+1} + h.c) \tag{2.17}$$

where μ is the on site chemical potential, $t \geq 0$ is the strength of the hopping between nearest neighbouring sites, $\Delta \geq 0$ is the superconducting pairing between electrons in neighbouring site, and ϕ is the superconducting phase.
Let us first analyse the bulk band structure. By imposing periodic boundary conditions on the chain, we can Fourier transform the operators $c_i^\dagger$ and c_i, and write them in terms of the momentum space creation and annihilation operators $c_k^\dagger$, c_k. We can then arrange them in a two-component vector

$$C_k = \begin{pmatrix} c_k \\ c_{-k}^\dagger \end{pmatrix}$$

which allows us to re-write 2.17 in matrix form as

$$H = \frac{1}{2} \sum_k C_k^\dagger H_k C_k \tag{2.18}$$

with

$$H_k = \begin{pmatrix} \epsilon_k & \bar{\Delta}^* \\ \bar{\Delta} & -\epsilon_k \end{pmatrix} \tag{2.19}$$

where $\epsilon_k = -t - \cos k - \mu$ is the kinetic energy and $\bar{\Delta} = -i\Delta e^{i\phi} \sin k$ is the superconducting pairing after Fourier transforming to k space. Note that the superconducting pairing, rather than being constant as in the s-wave superconductor that we saw previously, is an odd function of the momentum.

To diagonalise the BdG Hamiltonian 2.18, we introduce the Bogoliubov quasiparticles operators

$$\begin{aligned} a_k &= u_k c_k + v_k c_{-k}^\dagger \\ a_k^\dagger &= u_k^* c_k^\dagger + v_{-k}^* c_k \end{aligned} \tag{2.20}$$

in terms of which the 2.18 takes the diagonal form

$$H = \sum_k E_k a_k^\dagger a_k. \tag{2.21}$$

E_k is the dispersion relation in the quasiparticles basis and it reads

$$E_k = \sqrt{\epsilon_k^2 + |\bar{\Delta}_k|^2} \tag{2.22}$$

while the coefficients of the Bogoliubov transformation are

$$\begin{aligned} u_k &= \frac{\bar{\Delta}}{|\bar{\Delta}|} \frac{\sqrt{E_k + \epsilon}}{\sqrt{2E_k}} \\ v_k &= \left(\frac{E_k - \epsilon}{\bar{\Delta}} \right) u_k. \end{aligned} \tag{2.23}$$

The pairing Δ, being an odd function of k, vanishes in $k = 0$ and $k = \pm\pi$, implying that the spectrum of Bogoliubov excitations given by the 2.22 is gapless when $\mu = \pm t$, which coincides with the chemical potential being at the top and at the bottom of the conduction band.
There are therefore three regions separated by the gap closing:$\mu < -t$, $t < \mu < t$ and $\mu > t$, however, the first and the third are related by particle-hole symmetry so we can restrict ourselves to the two regions $\mu < -t$ and $|\mu| < t$ separated by the bulk gap closing at $\mu = -t$.
In order to study the implications of the gap closing, let us first recall that any two-by-two matrix can be expanded in a basis of Pauli matrices (plus, if necessary, a term proportional to the two-by-two identity matrix). In our case we have that H_k in 2.19 can be written as

$$H_k = \boldsymbol{h}(k) \cdot \boldsymbol{\sigma} \tag{2.24}$$

with $\boldsymbol{h}(k)$ vector components of the expansion which in our case read

$$\boldsymbol{h}(k) = \begin{pmatrix} \Delta \sin k \sin \phi \\ \Delta \sin k \cos \phi \\ -t \cos k - \mu \end{pmatrix}$$

The vector changes modulus and direction as k moves in the first Brillouin zone from $-\pi$ to π. If we assume that the bulk is always gapped, then $\boldsymbol{h}(k)$ is never zero, and we are allowed to define the unit vector $\hat{\boldsymbol{h}}(k) = \frac{\boldsymbol{h}(k)}{|\boldsymbol{h}(k)|}$ which maps the first Brillouin zone to the unit sphere.
One furthermore notices from symmetries consideration that it is sufficient to specify $\boldsymbol{h}(k)$ in the interval $0 < k < \pi$ since in fact one finds: $h_y(k) = -h_y(-k)$ and $h_z(k) = h_z(-k)$.
Moreover, from these considerations, one concludes that for k=0 and for $k = \pi$, the vector must be aligned along the z direction since $h_y(0) = h_y(\pi) = 0$. This allows us to write

$$\begin{aligned} \hat{\boldsymbol{h}}(0) &= \nu_0 \hat{\boldsymbol{z}} \\ \hat{\boldsymbol{h}}(\pi) &= \nu_\pi \hat{\boldsymbol{z}} \end{aligned} \tag{2.25}$$

where ν_0 and ν_π indicate the signs of the kinetic energy in 0 and π with respect to the Fermi level.
Therefore, one can see that starting with $\hat{\boldsymbol{h}}(k)$ at one pole of the unite sphere (whether top ot bottom along z axis, depending on the sign of the kinetic energy in k=0) when k=0, and varying k till π, one can either end up with $\hat{\boldsymbol{h}}(k)$ in the same pole or in the opposite pole. In order for the latter situation to occur, the kinetic energy must change sign for some values of k in

between 0 and π, meaning that the band gap has to close at some point and then open again. For the bulk spectrum to be gapless, $\boldsymbol{h}(k)$ has to be zero, i.e the trajectory of the unit vector $\hat{\boldsymbol{h}}(k)$ on the unit sphere passes through the origin, where the unit vector is ill-defined. In the former case, where $\hat{\boldsymbol{h}}(0) = \hat{\boldsymbol{h}}(\pi)$, the origin is not included in the trajectory, the unit vector is never ill defined and the bulk gap can never close. These two different trajectories of the unit vector on the Block sphere are therefore topologically distinct. The definitions in (2.25) allow us to individuate a quantity

$$\nu = \nu_0 \nu_\pi \tag{2.26}$$

that distinguishes between the two different trajectories. In fact, for how it is defined, ν can only assume the values ± 1 and it changes sign only when the kinetic energy changes sign, i.e. when after sweeping k from 0 to π we end up with $\hat{\boldsymbol{h}}(k)$ in the other pole of the unit sphere. That is, ν only changes sign when the bulk gap closes.
The topological invariant for the bulk chain of the Kitaev model can be derived also computing the Pfaffian of the Bloch Hamiltonian $H(k)$ in 2.18 [39]. Following this derivation of the topological invariant (which we will not discuss in details here for brevity reasons), one finds that $\nu = +1$ when the fermion parity of the ground state is even, and $\nu = -1$ when it is odd. The parity of the ground state of a conventional (trivial) superconductor is taken to be even such that all the electrons are bound in Cooper pairs.

Having the topological invariant at hand, we can discuss the two different regimes for $\mu < -t$ and $|\mu| < t$. First, we notice that the $\mu < -t$ phase can be connected *smoothly* with the trivial vacuum (i.e the state containing no fermions) by sending $\mu \to -\infty$. The trivial vacuum has even fermion parity and, given that the BdG Hamiltonian conserves the parity of fermionic pairs, in the all range $\mu < -t$ for each value of the chemical potential, one encounters an even number of pair of Fermi points. The value of ν for this phase is $+1$ and it constitutes the trivial phase.
After the gap closes, ν changes sign, thus the phase $|\mu| < t$ has $\nu = -1$ and it corresponds to the topological phase.

2.2.3 Open Chain

The non trivial phase is connected with the appearance of Majorana zero modes at the end of the open chain. In order to appreciate so, we consider now the chain with open boundaries described by (2.17). We can write the fermion operators c_i and $c_i^\dagger$ in terms of two Majorana operators as

$$c_i^\dagger = \frac{1}{2}(\gamma_{1i} + i\gamma_{2i})$$
$$c_i = \frac{1}{2}(\gamma_{1i} - i\gamma_{2i})$$

where $\gamma_1 = \gamma_1^\dagger, \gamma_2 = \gamma_2^\dagger$ and $\gamma_1^2 = \gamma_2^2 = 1$ obey fermionic anticommutation relations.
The Hamiltonian for the open chain in terms of γ is

$$H = -\frac{\mu}{2}\sum_{i=1}^{N}(1 + i\gamma_{2i-1}\gamma_{2i}) - \frac{i}{4}\sum_{i=1}^{N-1}[(\Delta + t)\gamma_{2i}\gamma_{2i+1} + (\Delta - t) + (\Delta - t)\gamma_{2i-1}\gamma_{2i+1}]. \tag{2.27}$$

In order to simplify the couplings between the modes, we consider two limiting cases for the parameters μ, Δ and t, in which the physics becomes evident: the first one corresponds to $t = \Delta = 0$ and $\mu < 0$, whereas for the the second one we set $t = \Delta \neq 0$ and $\mu = 0$.

We start by considering the first case, setting t=Δ=0 and $\mu < 0$. Here (2.27) reduces to

$$H = -\frac{\mu}{2}\sum_{i=1}^{N}(1 + i\gamma_{2i-1}\gamma_{2i}) \tag{2.28}$$

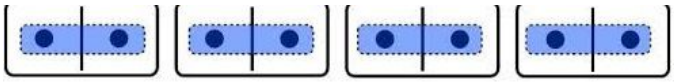

Figure 2.1: In figure, The lattice unit cells are represented by the rectangles and each dot indicates a Majorana. Starting from the first in the left we have γ_1, γ_2 (in the first cell), γ_3, γ_4(in the second cell) and so on. In our notation, if is the cell index, γ_{2i} is paired up with γ_{2i-1}. This figure has been taken from the series of online lectures on topological states of matter, Delft University.

where the only coupling surviving is the one between Majorana modes on the same site: all the modes are paired up to form a fermion on site, as showed in figure 2.1. From (2.28) we see that adding one pair of Majorana modes to the system has a cost in terms of energy: if one considers the ground state as the state where all the fermionic levels up to the Fermi energy are occupied, adding one fermion drives the system out of the ground state. This implies a unique, non degenerate, ground state and a gapped excitation spectrum. In the limiting case we are considering, the spectrum of the finite chain is gapped like the spectrum we obtained for the infinite (bulk) chain, meaning that including the ends of the chain in our treatment does not matter much.
This excitation spectrum matches with the gapped spectrum of a conventional superconductor, with a unique ground with even fermion parity in order for all the electrons to pair up in Cooper pairs.

In the second limiting case, where μ is set to zero and t=$\Delta \neq 0$, (2.27) reads

$$H = -i\frac{t}{2}\sum_{i=1}^{N-1}[\gamma_{2i}\gamma_{2i+1}] \tag{2.29}$$

and we see that Majorana are not paired on site but rather on neighbouring sites. The result is that the modes at the ends of the chain remain unpaired. Furthermore from (2.29) we observe that there is still finite energy cost for adding a fermion to the system in the bulk of the chain, however, the first and the last Majorana modes at the ends of the chain do not appear in the Hamiltonian. The end modes can be combined to form an ordinary but highly non-local fermionic state:

$$f = \frac{1}{2}(\gamma_1 + i\gamma_N). \tag{2.30}$$

Adding such a state to the chain costs zero energy, and the ground state of the system is two fold degenerate. Thus, in this limiting case, as opposed to what we observed in the previous one, considering the ends of the chain does make a difference: in fact, the excitation spectrum of the finite chain is still gapped in the bulk, but has zero energy excitation at its ends.
This configuration is quite different from the one of a conventional superconductor, as there are two degenerate ground states with different fermion parity.
Apart from the zero energy cost, f has another peculiarity compared to the fermionic excitations in the bulk: being non local, means that is immune to local quantum perturbation arising in the system, and the only way to decouple the two Majorana end modes is to have other states at zero energy with which they can merge. In other words, to split the two modes localised at the end of the chain, the bulk gap has to close.
This fact has two important consequences: first, it means that the two limiting case considered above describe two topologically distinct phases, and second, it implies that the end modes are *topologically protected* by local perturbations (they stay localized at the end as long as the bulk gap is open).
The topological protection of the end modes allows us to claim that the conclusions obtained in the limiting case above, holds also for a more general case, as, changing the values of μ, t and Δ from the fine tuned $\mu = 0$ and $t = \Delta$, does not decouple the Majorana end modes unless a topological phase transition occurs. As one might already have guessed, the chain with

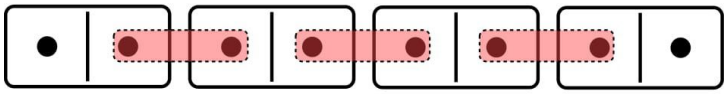

Figure 2.2: In figure, the rectangles delimit the lattice unit cell, and the dots represent Majorana modes. Here, the the second mode of cell i couples with the first mode of cell i+1, leaving the first and the last mode of the chain unpaired.

$t, \Delta = 0, \mu < 0$ maps to the trivial superconducting phase described in the bulk by $\mu < -2t$, whereas the chain where $\mu = 0$ corresponds to the region where $|\mu| < t$ in the bulk, where the topological invariant ν is equals -1.

2.3 Realization of Majorana end Modes in 1D Nanowire

In the last section of this chapter, we introduce the theoretical model for a practical realization of Majorana end modes in a one-dimensional semiconducting nanowire in presence of an external magnetic field and with s-wave superconductivity induced by proximity with a parent bulk superconductor.
This model, proposed in [23, 40], has been extensively studied as it is considered one of the most promising system for detecting the Majorana modes.
In further chapter of the thesis, we modify the set-up of the model by introducing a local perturbation on the spin orbit coupling of the semiconductor and we ask if this local perturbation affects the topological properties of the system.
We consider therefore important to discuss this model in details and, in particular, to derive the criterion for the topological phase transition (analogous to the $|\mu| = t$ in the Kitaev chain).
The derivation discussed in the following closely follows [16]

The real space Hamiltonian for a semiconducting (1D) wire with Rashba spin orbit coupling and the Zeeman field along perpendicular directions is

$$H_{1D} = \sum_{\sigma,\sigma'} \int dx \Psi^{\dagger}_{\sigma}(x) \left[\left(-\frac{\partial_x^2}{2m} - \mu \right) \delta_{\sigma,\sigma'} + B\tau^z_{\sigma,\sigma'} - i\alpha\tau^y_{\sigma,\sigma'}\partial_x \right] \Psi_{\sigma'}(x) \tag{2.31}$$

where we have set once more $\hbar = 1$, τ^y and τ^z are the Pauli matrix y and z acting on electron spins, and $\Psi(x)$ and $\Psi^{\dagger}(x)$ are fermionic fields describing the of electrons in the semiconductor
The real space effective Hamiltonian for a conventional s-wave superconductor is given by the BCS mean field Hamiltonian already discussed in a previous section

$$H_{SC} = \Delta \int dx (\Psi(x)_{\uparrow}\Psi(x)_{\downarrow} + h.c) \tag{2.32}$$

Therefore, the total Hamiltonian describing our system reads

$$H = H_{1D} + H_{SC} \tag{2.33}$$

Let us consider H_{1D} first. The time independent Schrödinger equationat B=0 $\hat{H}_{1D}|\Psi\rangle = E|\Psi\rangle$ is solved by $\Psi(x) = e^{ikx}\chi_{\sigma}$. The resulting band energies are

$$\epsilon_{\pm}(k) = \frac{k^2}{2m} - \mu \pm (\alpha k) \tag{2.34}$$

The bands are illustrated by figure 2.3. Here, we observe that with the Zeeman field at zero, there is no spinless regime, since for each value of the Fermi Energy, we always have an even number of pair of Fermi points.
The spinless regime can be obtained turning on the magnetic field, thus lifting the degeneracy in zero. The two bands 2.34 read

$$\epsilon_{\pm}(k) = \frac{k^2}{2m} - \mu \pm \sqrt{(\alpha k)^2 + B^2} \tag{2.35}$$

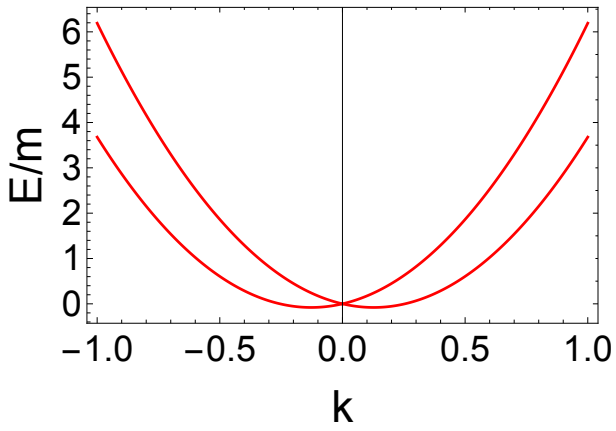

Figure 2.3: Spin splitted energy bands in presence of Rashba SOC. The energy is in units of m.

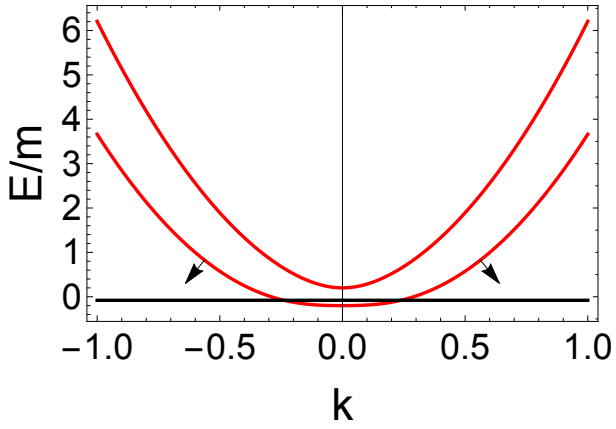

Figure 2.4: Electron bands of the semiconducting wire with magnetic field along z direction, orthogonal to Rashba SOC. When $-B < \mu < B$, the system appears spinless, and, as showed by the black line in figure, for a value the chemical potential within this range, one encounters one pair of Fermi points. The energy is in units of m.

As we appreciate from 2.4, when the Fermi energy resides in between the gap at $k = 0$ induced by the magnetic field, there is only one pair of Fermi points, yielding the desired 'spinless' regime. The competition between Rashba SOC and Zeeman field in orthogonal direction prevents the spins in one energy band to be fully polarised, and this is crucial for the inherited s-wave pairing to be able to open a gap at the Fermi level.

To better understand this, let us consider the Bogoliubov de Gennes form of Hamiltonian 2.33, where α is now set to zero, so the spin degeneracy is removed by the applied magnetic field, which fully polarizes the spins along the z-direction. We Fourier transform to momentum space and write the Hamiltonian in matrix form as

$$H = \begin{pmatrix} \mathbf{\Psi}^\dagger(k), & \mathbf{\Psi}(-k) \end{pmatrix} \begin{pmatrix} \xi_k \cdot \boldsymbol{I} + B \cdot \boldsymbol{\tau}^z & i\Delta \cdot \boldsymbol{\tau}^y \\ -i\Delta \cdot \boldsymbol{\tau}^y & -\xi_k \cdot \boldsymbol{I} - B \cdot \boldsymbol{\tau}^z \end{pmatrix} \begin{pmatrix} \mathbf{\Psi}(k) \\ \mathbf{\Psi}^\dagger(-k) \end{pmatrix} \tag{2.36}$$

where $\mathbf{\Psi}(k) = \{\Psi(k)_\uparrow, \Psi(k)_\downarrow$, $\boldsymbol{I}$ is the 2x2 identity matrix, $\boldsymbol{\tau}^{y,z}$ are the 2×2 Pauli matrices and $\xi_k = \frac{k^2}{2m^*} - \mu$. Note that $\left(\mathbf{\Psi}(k), \mathbf{\Psi}^\dagger(-k)\right)^T$ is the four-component Nambu spinor introduced before. The band structure, shown in figure 2.5, is found by diagonalizing the

$$H_k = \begin{pmatrix} \xi_k \cdot \boldsymbol{I} + B \cdot \boldsymbol{\tau}^z & i\Delta \cdot \boldsymbol{\tau}^y \\ -i\Delta \cdot \boldsymbol{\tau}^y & -\xi_k \cdot \boldsymbol{I} - B \cdot \boldsymbol{\tau}^z \end{pmatrix}. \tag{2.37}$$

As showed in 2.5, in absence of spin orbit coupling, the spin bands carry a well-defined momentum aligned along z, and we can see from the dispersion relation plot that the electron and hole bands crossing at zero energy carry the same spin. Therefore, carriers in those bands

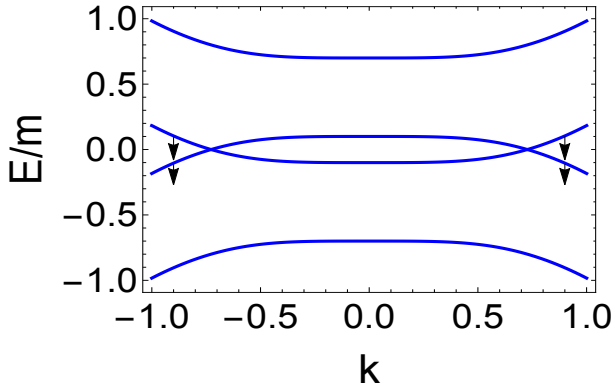

Figure 2.5: The figure shows the energy bands obtained from the BdG Hamitlonian where the strength of the Rashba coupling α is set to zero. We see no gap opening in the Bogoliubov spectrum since the electron and hole bands crossing at zero energy carry the same spin, thus cannot be coupled by singlet pairing. The chemical potential is set to zero and the electronic bands are mirrored along the x-axis by Particle-Hole symmetry. The energy is in units of m.

cannot be coupled by singlet Cooper pairing. As a result, unless the Δ pairing is strong enough to overcome the Zeeman splitting and couple electrons and holes at higher energy, no singlet pairing can occur in the semiconducting system.
Fortunately, this issue is solved when $\alpha \neq 0$ as the SOC in the semiconductor cants the spins away from the z-direction, promoting opposite spins for the states at momenta k and $-k$.

With the previous analysis, we have established the fundamental role of each term in the Hamiltonian in order to actually reproduce the ideal environment for the appearance of Majorana modes: a spinless superconductor.
We are now ready to look at the bulk spectrum of the Hamiltonian 2.33.
By imposing periodic boundary conditions, we can write the Hamiltonian in Fourier space as

$$\begin{aligned} H = \sum_{\sigma,\sigma'} \int dk \Psi^\dagger_{k,\sigma} [(\frac{k^2}{2m} - \mu)\delta_{\sigma,\sigma'} + B\tau^z_{\sigma,\sigma'} - \alpha k \tau^y_{\sigma,\sigma'}] \Psi_{k,\sigma'} \\ + \Delta \int dk [\Psi^\dagger_{\uparrow,k} \Psi^\dagger_{\downarrow,-k} + \Psi_{\downarrow,-k} \Psi_{\uparrow,k}] \end{aligned} \tag{2.38}$$

with $\tau^{x,y,z}$ Pauli matrices acting on spin space, and $\Psi^\dagger_{k,\sigma}$ and $\Psi_{k,\sigma}$ the fermionic field in momentum space.
As usual, it is convenient for us to write the Hamiltonian 2.38 in BdG matrix form as

$$H = \int dk \begin{pmatrix} \mathbf{\Psi}^\dagger_k & \mathbf{\Psi}_{-k} \end{pmatrix} H_k \begin{pmatrix} \mathbf{\Psi}_k \\ \mathbf{\Psi}^\dagger_{-k} \end{pmatrix} \tag{2.39}$$

where, as before, $\mathbf{\Psi}_k = (\Psi_{k,\uparrow}, \Psi_{k,\downarrow})$ and the $(\mathbf{\Psi}_k, \mathbf{\Psi}^\dagger_{-k})^T$ is the 4-component Nambu spinor. In this basis, the 4×4 matrix H_k reads

$$H_k = \begin{pmatrix} \frac{k^2}{2m} - \mu + B & ik\alpha & 0 & \Delta \\ -ik\alpha & \frac{k^2}{2m} - \mu - B & -\Delta & 0 \\ 0 & -\Delta & -\frac{k^2}{2m} + \mu - B & -ik\alpha \\ \Delta & 0 & ik\alpha & -\frac{k^2}{2m} + \mu + B \end{pmatrix} \tag{2.40}$$

and the diagonalization of H_k leads to the four eigenvalues

$$E(k) = \pm \frac{1}{2} \sqrt{4B^2 + k^4 m^2 \pm 4\sqrt{B^2[a\Delta^2 + (k^2 m - 2\mu)^2] + k^2\alpha^2(k^2 m - 2\mu)^2 + 4k^2(\alpha^2 - m\mu) + 4\Delta^2 + 4\mu^2}}. \tag{2.41}$$

In order to understand where a topological phase transition occurs, we need to find the condition for which the gap of the bulk excitation spectrum vanishes. The BdG Hamiltonian

conserves Particle-Hole symmetry, i.e $H_k = -H_{-k}$, thus, from 2.41 we conclude that the energy gap closes at $k = 0$. Setting $E(0) = 0$ one obtains

$$E(0) = \sqrt{B^2 + \Delta^2 + \mu^2 \pm \sqrt{B^2\Delta^2 + B^2\mu^2}} \tag{2.42}$$

which is solved for

$$B = \sqrt{\Delta^2 + \mu^2} \tag{2.43}$$

The 2.43 gives the critical value of the magnetic field for which the topological phase transition occurs.
For $B < \sqrt{\Delta^2 + \mu^2}$, the wire does not appear spinless, and the superconducting gap occurs between antiparallel spins in two different energy bands, resulting in conventional superconductivity, with singlet paring between electrons. In this conditions, the system is in characterized by a strong pairing regime, and it can be shown that the Hamiltonian describing this phase of the system maps continuously to the Kitaev Hamiltonian in the regime $\mu < -t$ [16].
On the other hand, when $B > \sqrt{\Delta^2 + \mu^2}$, the wire appears spinless and the only possible pairing must occur between spins in the same energy band. This pairing is made possible, as underlined before, by the presence of the SOC, which rotates the spins as one sweeps from $-k$ to k. The intraband pairing is a momentum dependent pairing and couples spins in a triplet state: it is the p-wave pairing. Thus for B higher than the critical value, the system resides in the weakly coupled regime,corresponding to the topological phase of the Kitaev chain for $-t < \mu < t$.
In order to show the emergence of the momentum-dependent superconducting pairing, we perform a change of basis on the Hamiltonian 2.38 and re-write it terms of the operators $\Psi^\dagger_\pm(k)$ and $\Psi_\pm(k)$ which create (annihilate) an electron with energy $\epsilon_\pm(k)$ given by the 2.35 at the proximity between the wire and the superconductor (i.e we change to the basis which diagonalises H_{1D}). We thus perform the unitary transformation

$$\begin{pmatrix} \Psi_\uparrow(k) \\ \Psi_\downarrow(k) \end{pmatrix} = \boldsymbol{U} \begin{pmatrix} \Psi_+(k) \\ \Psi_-(k) \end{pmatrix} \tag{2.44}$$

with $\boldsymbol{U}$ given by the normalized eigenvectors which diagonalise H_{1D}

$$\boldsymbol{U} = \begin{pmatrix} \frac{\alpha k}{D_+} & \frac{\alpha k}{D_-} \\ -\frac{i(B+A)}{D_+} & -\frac{i(B-A)}{D_-} \end{pmatrix} \tag{2.45}$$

where $A = \sqrt{B^2 + (\alpha k)^2}$ (the square root term in eigenvalues $\epsilon_\pm(k)$ from the 2.35), $D_\pm = \sqrt{(\alpha k)^2 + (B \pm A)}$.
Therefore

$$\begin{aligned} \Psi_\uparrow(k) &= \frac{\alpha k}{D_+}\Psi_-(k) + \frac{\alpha k}{D_-}\Psi_+(k) \\ \Psi_\downarrow(k) &= -\frac{i(B+A)}{D_+}\Psi_-(k) - \frac{i(B-A)}{D_-}\Psi_+(k) \end{aligned} \tag{2.46}$$

Since we know that H_{1D} is diagonal in the basis of $\Psi(k)_\pm$ and that it explicitly reads

$$H_{1D} = \int dk \Psi^\dagger_+(k)\epsilon_+(k)\Psi_+(k) + \Psi^\dagger_-(k)\epsilon_-(k)\Psi_-(k), \tag{2.47}$$

all we have to do is to express H_{SC} in this basis, which yields

$$\begin{aligned} H_{SC} &= -\Delta \int dk \Psi_\uparrow(k)\Psi_\downarrow(-k) + h.c \\ &= -\Delta \int dk \left(\frac{\alpha k}{D_+}\Psi_-(k) + \frac{\alpha k}{D_-}\Psi_+(k)\right)\left(-\frac{i(B+A)}{D_+}\Psi_-(-k) - \frac{i(B-A)}{D_-}\Psi_+(-k)\right) + h.c \end{aligned} \tag{2.48}$$

expanding the above we obtain

$$\begin{aligned} H_{SC} = &\int dk \frac{B\Delta}{A}[\Psi_-(-k)\Psi_+(k) + h.c] \\ &+ \int dk \frac{\alpha k \Delta}{A}[\Psi_+(-k)\Psi_+(k) + \Psi_-(-k)\Psi_-(k) + h.c]. \end{aligned} \tag{2.49}$$

The first term indicates the interband conventional s-wave, where the pairing $\Delta_s = \frac{B\Delta}{\sqrt{B^2+(\alpha k)^2}}$ is symmetric in momentum space, whereas the second term contains the intraband pairing $\Delta_p = \frac{\alpha k \Delta}{\sqrt{B^2+(\alpha k)^2}}$ which encodes p-wave pairing. The latter, is an odd function of the momentum k as required from Pauli exclusion principle when the pairing occurs in the triplet state.

Tight Binding

We now derive the topological criterion for the system discretized on a lattice of points, described by a tight binding model. The tight binding Hamiltonian for 2.33 above is obtained defining second quantised operators c_i and $c_i^\dagger$ which respectively annihilate and create a fermion on the lattice site i, and using the finite difference to re-write the derivatives as $\partial_x \Psi_i = \Psi_{i+a} - \Psi_{i-a}/2a$. Assuming the Rashba SOC along y direction as above and Zeeman splitting along z the tight binding Hamiltonian in which we consider only nearest neighbours hopping reads

$$\begin{aligned} H = &- t \sum_{<i,j>,\sigma} c^\dagger_{i,\sigma} c_{j,\sigma} + h.c - \mu \sum_{i,\sigma} c^\dagger_{i,\sigma} c_{i,\sigma} \\ &+\alpha \sum_{<i,j>,\sigma,\sigma'} c^\dagger_{i,\sigma} \tau^y_{\sigma,\sigma'} c_{j,\sigma'} + h.c + B \sum_{i,\sigma,\sigma'} c^\dagger_{i,\sigma} \tau^z_{\sigma,\sigma'} c_{i,\sigma'} + \Delta \sum_i c^\dagger_{i,\uparrow} c^\dagger_{i,\downarrow} + h.c \end{aligned} \tag{2.50}$$

where we have set the lattice constant $a = 1$ for simplicity.
Our aim is to derive the topological critical point in the tight binding description of the system. Therefore we Fourier transform the operators in momentum space and study the bulk band structure. The 2.50 then becomes

$$\begin{aligned} H = &\sum_{k,\sigma,\sigma'} c^\dagger_{k,\sigma}[(-2t\cos k - \mu)\delta_{\sigma,\sigma'} + \alpha \sin k \tau^y_{\sigma,\sigma'} + B\tau^z_{\sigma,\sigma'}]c_{k,\sigma'} \\ &+ \Delta \sum_k [c^\dagger_{k,\uparrow} c^\dagger_{-k,\downarrow} + c_{-k,\downarrow} c_{k,\uparrow}]. \end{aligned} \tag{2.51}$$

The diagonalization procedure is the typical one, and after defining a Nambu spinor in momentum space as usual, one finds the tight binding BdG Hamiltonian, where the matrix H_K reads

$$H_k = \begin{pmatrix} -\mu - 2t\cos k & B - 2i\alpha \sin k & 0 & \Delta \\ B + 2i\alpha \sin k & -\mu - 2t\cos k & -\Delta & 0 \\ 0 & -\delta & \mu + 2t\cos k & -B + 2i\alpha \sin k \\ \Delta & 0 & -B - 2i\alpha \sin k & \mu + 2t\cos k \end{pmatrix} \tag{2.52}$$

where t is the hopping term $t = k^2/2m$. One then diagonalises H_k in (2.52) to find the energy eigenvalues.

The gap closes at the point $k = 0$ in the first mBZ. Therefore, in order to derive the criterion for the gap closing in parameter space, one sets $E(0) = 0$ and finds: $E(0) = \pm B \pm \sqrt{(\mu + 2t)^2 + \Delta^2}$ which implies that, in the tight binding approximation, the gap closes when

$$B = \sqrt{(\mu + 2t)^2 + \Delta^2}. \tag{2.53}$$

At low-energy and close to $k = 0$, where the effects of the bandwidth can be neglected, the two models at continuum and the tight binding lead to the same dispersion and to the same criterion

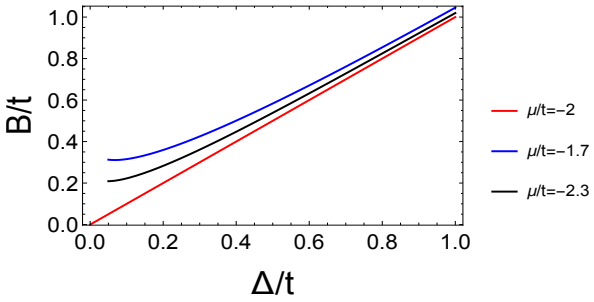

Figure 2.6: Phase transition diagram in the B/Δ plane in presence of only the constant Rashba SOC. α_r/t =0.3

for the gap closing. Therefore, the tight binding is a good approximation in the limit we want to consider, and we will use it for modelling our system in the rest of the thesis.

As a last remark, we plot the phase diagram which shows the transition from trivial and topological phase. The diagram plotted in figure 2.6 shows that the line $\mu = -2t$, where, according to the 2.53, the transition occurs when $B = \Delta$, represents an optimal condition for driving the system in the topological phase. In fact, shifting the value of μ (provided that one remains in the spinless regime created by the Zeeman splitting), the trivial phase (right side of the coloured lines in the plot) gets extended, reducing the portion of the diagram in which the system is in the topological phase.

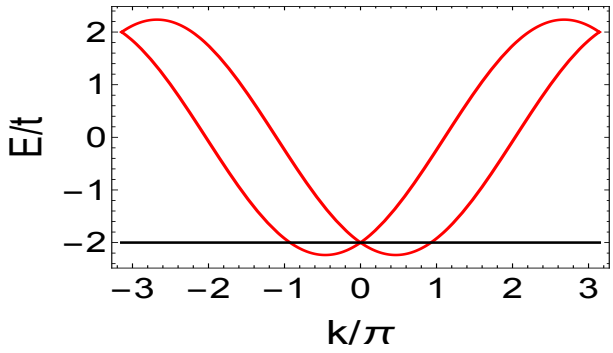

Figure 2.7: The figure shows the band structure at tight binding for the 1D wire where the magnetic field is set to zero. The system preserves Time Reversal symmetry so for each value of the Fermi level, there are four Fermi points, as stated by Kramer theorem.

Notice furthermore that the value $\mu = -2t$ coincides with the energy value of the band crossing in $k = 0$ due to Kramer degeneracy when the magnetic field is zero.

Chapter 3

Spin orbit coupling in Curved Geometries

In the previous chapter, we have introduced the model for a 1D semiconducting nanowire with spin orbit coupling living in a flat geometry.
As already mentioned in the introduction, experimental progresses have allowed to engineer curved nanostructures such as spiral-like nanotubes and nanohelics [41, 42]. Studies on those semiconducting materials, have shown that the non trivial geometry of a curved semiconducting nanowire can lead to topological insulating phases[43].
Motivated by these recent observations, in this thesis we will be concerned in studying the influence of the non trivial geometry of the semiconducting wire on the topological phase of the system hosting Majorana fermions introduced in the previous chapter.
For this purpose, in this chapter, after spending some time in recalling the origin of the SOC in semiconductors, we derive an effective one dimensional Hamiltonian for electrons moving on a curved geometry, and we show that this non trivial geometrical shape results in fact in a periodic canting of the electron spins.

3.1 Spin Orbit Coupling

The spin orbit interaction arises as a relativistic effect concerning the motion of an electron in an external electric field E.
In the case of the atomic spin orbit coupling, the latter is provided by the interaction between the electron intrinsic angular momentum (spin) and the electric field originating by Coulomb interaction between the electron and the nucleus. The coupling of the electron spin with the Coulomb field can be explained semi-classically, as it was first done by Thomas in 1926 [44], by using the Bohr model of Hydrogen atom and the kinematics for a relativistic particle.
Following this reasoning, one starts by describing the interaction between electron and nucleus in the electron rest frame. Due to Lorentz transformation, one finds that, when the electron is on its own rest frame, it experiences a magnetic field coming from the cyclic orbit of the nucleus given by $\boldsymbol{B} = -\boldsymbol{v} \times \frac{\boldsymbol{E}}{c}$. The electron magnetic moment $\boldsymbol{\mu}_s = -\frac{g_s \mu_B}{\hbar}\boldsymbol{S}$ (where g_s is the giroscopic constant, almost 2 for the electron, and μ_B the Bohr magneton) interacts with this magnetic field, leading to a potential term of the form $H_{SO} = -\boldsymbol{\mu}_s \cdot B = \boldsymbol{\mu}_s \cdot \boldsymbol{v} \times \nabla \boldsymbol{V}$. Since the Coulomb potential is a central potential depending only on the distance radius r, the spin orbit potential can be written as

$$H_{SO} = \frac{1}{ecr}\frac{dV}{dr}\boldsymbol{\mu}_s \cdot \boldsymbol{v} \times \boldsymbol{r} = \frac{g_s}{ecr}\frac{\mu_B}{m\hbar}\boldsymbol{S} \cdot \boldsymbol{L} = -\frac{\hbar}{2m^2c^2}\frac{1}{r}\frac{dV}{dr}\boldsymbol{\sigma} \cdot \boldsymbol{L} \tag{3.1}$$

in which the coupling $\boldsymbol{S} \cdot \boldsymbol{L}$ is manifest. For the last equality we have used that $\boldsymbol{s} = \frac{\hbar}{2}\boldsymbol{\sigma}$.
However, one needs to take into account that the electron rest frame is not an inertial frame, and the constant acceleration of the electron amounts to subsequent Lorentz boosts. Applying

two generic (non collinear) Lorentz boosts subsequently, yields to a composition of a boost and a rotation [45]. Therefore, when taking into account the rotation in the accelerating frame of the electron, the spin orbit potential reads

$$H_{SO} = -\frac{\hbar}{2m^2c^2}\frac{1}{r}\frac{dV}{dr}\boldsymbol{\sigma}\cdot\boldsymbol{L} + \frac{\hbar}{4m^2c^2}\frac{1}{r}\frac{dV}{dr}\boldsymbol{\sigma}\cdot\boldsymbol{L} = -\frac{\hbar}{4m^2c^2}\frac{1}{r}\frac{dV}{dr}\boldsymbol{\sigma}\cdot\boldsymbol{L} \tag{3.2}$$

where the second term in the second equality is the so-called Thomas precession term.
The term in the last equality is the full spin orbit coupling term, which can be shown to coincide with the spin orbit coupling term in the Scrödinger-Pauli Hamiltonian derived as a non relativistic limit of the Dirac equation. Therefore, we follow now this approach to derive the spin orbit coupling term in a more formal way.

The time independent Dirac equation for spin 1/2 particles reads

$$(c\boldsymbol{\alpha}\cdot\boldsymbol{p} + \beta m_0c^2 + V)\Psi = E\Psi \tag{3.3}$$

where

$$\boldsymbol{\alpha} = \begin{pmatrix} 0 & \boldsymbol{\sigma} \\ \boldsymbol{\sigma} & 0 \end{pmatrix} \tag{3.4}$$

with $\boldsymbol{\sigma}$ being the vector of Pauli matrices $\boldsymbol{\sigma} = \{\sigma_x, \sigma_y, \sigma_z\}$, and

$$\boldsymbol{\beta} = \begin{pmatrix} \mathbf{1}_{2x2} & 0 \\ 0 & -\mathbf{1}_{2x2} \end{pmatrix}. \tag{3.5}$$

The Diras spinor ψ is a four-component spinor, but the Scrödinger-Pauli equation is an equation of a two-component spinor (the spin up and spin down projection of a spin 1/2 particle). As a first step, we can thus re-write the Dirac spinor as $\Psi = \begin{pmatrix} \Psi_A \\ \Psi_B \end{pmatrix}$, with Ψ_A indicating the first two component and Ψ_B the last two.
The Dirac equation above couples the components Ψ_A and Ψ_B, yielding the equations

$$\begin{aligned} (\boldsymbol{\sigma}\cdot\boldsymbol{p})\Psi_B &= \frac{1}{c}(\bar{E} - V)\Psi_A \\ (\boldsymbol{\sigma}\cdot\boldsymbol{p})\Psi_A &= \frac{1}{c}(\bar{E} - V + 2m_0c^2)\Psi_B \end{aligned} \tag{3.6}$$

where we have defined $\bar{E} = E - m_0c^2$.
From the second equation we can find $\Psi_B = \frac{c(\boldsymbol{\sigma}\cdot\boldsymbol{p})}{\bar{E}-V+2m_0c^2}\Psi_A$ and re-write the equation for Ψ_A as

$$(\boldsymbol{\sigma}\cdot\boldsymbol{p})\left(\frac{c^2}{\bar{E} - V + 2m_0c^2}\right)(\boldsymbol{\sigma}\cdot\boldsymbol{p})\Psi_A = (\bar{E} - V)\Psi_A. \tag{3.7}$$

In the non relativistic limit, the quantity $\frac{(\bar{E}-V)}{2m_0c^2} \approx (\frac{v}{c})^2$ is small so we can Taylor expand the $\left(\frac{c^2}{\bar{E}-V+2m_0c^2}\right)$ in the previous expression as

$$\frac{1}{2m_0c^2}\left(\frac{c^2}{\frac{\bar{E}-V}{2m_0c^2}+1}\right) = \frac{1}{2m_0}\left(1 - \frac{(\bar{E}-V)}{2m_0c^2} + ...\right). \tag{3.8}$$

Requiring the Dirac spinor to be normalized to one implies

$$\int d^3x\Psi^\dagger\Psi = 1 \rightarrow \int d^3x(\Psi_A^\dagger\Psi_A + \Psi_B^\dagger\Psi_B) = 1 \tag{3.9}$$

which shows that the equation 3.3 for Ψ is not equivalent to the 3.7 for Ψ_A as the latter itself is not normalized to one. Substituting in the normalisation relation $\Psi_B = \frac{c(\boldsymbol{\sigma}\cdot\boldsymbol{p})}{\bar{E}-V+2m_0c^2}\Psi_A$ derived above, and recalling that for an electron moving in an electromagnetic field the momentum $\boldsymbol{p}$

is the canonical momentum $\boldsymbol{p} = (\boldsymbol{p}_0 - e\boldsymbol{A})$, where $\boldsymbol{A}$ is the vector potential, we have for the normalization relation

$$1 = \int d^3r \Psi_A^+ \left[1 + \frac{1}{4m_0^2c^2} \left(\boldsymbol{\sigma} \cdot (\boldsymbol{p}_0 - e\boldsymbol{A})\right) \left(\boldsymbol{\sigma} \cdot (\boldsymbol{p}_0 - e\boldsymbol{A})\right)\right] \Psi_A \tag{3.10}$$

where we have neglected orders higher than $(v/c)^2$. Using the identity $(\boldsymbol{\sigma} \cdot \boldsymbol{a})(\boldsymbol{\sigma} \cdot \boldsymbol{b}) = (\boldsymbol{a} \cdot \boldsymbol{b}) + i\boldsymbol{\sigma}(\boldsymbol{a} \times \boldsymbol{b})$ and that $(\boldsymbol{p} - e\boldsymbol{A}) \times (\boldsymbol{p} - e\boldsymbol{A}) = -ie\boldsymbol{B}$, we obtain

$$1 = \int d^3r \Psi_A^\dagger \left[1 + \frac{p^2 + e\boldsymbol{\sigma} \cdot \boldsymbol{B}}{4m_0^2c^2}\right] \Psi_A, \tag{3.11}$$

from which we can define the spinor $\bar{\Psi}$ as

$$\bar{\Psi} = \left(1 + \frac{p^2 + e\boldsymbol{\sigma} \cdot \boldsymbol{B}}{8m_0^2c^2}\right) \Psi_A \tag{3.12}$$

which is normalised to unity. Plugging $\bar{\Psi}$ in the 3.7, up to order $(v/c)^2$ we obtain the Scrödinger-Pauli equation

$$\left[\frac{p^2}{2m_0} + V - \frac{p^4}{8m_0^3c^2} - \frac{\hbar}{4m_0^2c^2}\boldsymbol{\sigma} \cdot \boldsymbol{p} \times \nabla V_0 - \frac{e\hbar^2}{8m_0^2c^2}\nabla \cdot \boldsymbol{\mathcal{E}} + \frac{e\hbar}{2m_0}\boldsymbol{\sigma} \cdot \boldsymbol{B} - \frac{e\hbar p^2}{4m_0^3c^2}\boldsymbol{\sigma} \cdot \boldsymbol{B}\right] \bar{\Psi} = \bar{E}\bar{\Psi} \tag{3.13}$$

where $\boldsymbol{\mathcal{E}} = (1/e)\nabla V_0$ indicates the electric field. In the previous equation, the third term is a relativistic correction on the kinetic energy, the fourth therm is the spin orbit coupling term, the fifth term is the so- called Darwin term, the sixth term is the Zeeman term and the last term in the equation, a relativistic correction on the latter.

3.1.1 Spin Orbit Coupling in Semiconductors

The Scrödinger-Pauli equation above describes the motion of an electron in an external potential in the vacuum.
When considering the motion of the electron in a semiconductor, the $\boldsymbol{k} \cdot \boldsymbol{p}$ method constitutes a powerful tool to find the band structure of the system in the vicinity of the band edge. In the following, we underline the main features of this method.

We start from the Scrödinger equation for the electrons in a periodic lattice

$$\left(\frac{p^2}{2m_0} + V_0(r)\right) \Psi(r) = E\Psi(r) \tag{3.14}$$

where $V_0(r)$ is the crystal potential. We then write the wavefunctions $\Psi(r)$ in terms of Bloch functions as $\Psi(r) = e^{i\boldsymbol{k}\cdot\boldsymbol{r}} u_{\nu,\boldsymbol{k}}(r)$, where ν is the band index. Acting with the momentum operator $\boldsymbol{p} = -i\hbar\partial_r$ on the plane waves part of the previous equation we obtain the equation for the periodic part of the Bloch functions as

$$\left(\frac{p^2}{2m_0} + \frac{\hbar^2k^2}{2m_0} + \frac{\hbar}{m_0}\boldsymbol{k} \cdot \boldsymbol{p} + V_0(r) + \right) u_{\nu,\boldsymbol{k}}(r) = E_{\nu,\boldsymbol{k}}(\boldsymbol{k}) u_{\nu,\boldsymbol{k}}(r). \tag{3.15}$$

Including the Pauli spin orbit coupling term in 3.14 and acting on the plane wave part with the operator $\boldsymbol{p}$ we get

$$\left(\frac{p^2}{2m_0} + \frac{\hbar^2k^2}{2m_0} + \frac{\hbar}{m_0}\boldsymbol{k} \cdot \boldsymbol{p} + \frac{\hbar}{4m_0^2c^2}(\boldsymbol{\sigma} \times \nabla V_0)(\hbar\boldsymbol{k} + \boldsymbol{p}) + V_0\right) u_{n,\boldsymbol{k}}(r) = E_{n,\boldsymbol{k}}(\boldsymbol{k}) u_{\nu,\boldsymbol{k}}(r). \tag{3.16}$$

Note that, since now the orbital and the spin degree of freedom are coupled the conserved quantity is the total angular momentum $J = L + S$ and the band index n identifies the bands

according to their total angular momentum quantum number. Defining the operator $\mathbf{\Pi}$ via minimal substitution as

$$\mathbf{\Pi} = \boldsymbol{p} + \frac{\hbar}{4m_0c^2}(\boldsymbol{\sigma} \times \nabla V_0) \tag{3.17}$$

we can re-write the above equation as

$$\left(\frac{p^2}{2m_0} + \frac{\hbar^2k^2}{2m_0} + \frac{\hbar}{m_0}\boldsymbol{k}\cdot\mathbf{\Pi} + \frac{\hbar}{4m_0^2c^2}\boldsymbol{p}\cdot(\boldsymbol{\sigma}\times\nabla V_0) + V_0\right)u_{n,\boldsymbol{k}}(r) = E_{\nu,\boldsymbol{k}}(\boldsymbol{k})u_{n,\boldsymbol{k}}(r). \tag{3.18}$$

Recalling that $u_{n,\boldsymbol{k}}(r) = \langle \boldsymbol{r}|n,\boldsymbol{k}\rangle$, we can write the Scrödinger-Pauli equation for the two component spinors $|n,\boldsymbol{k}\rangle$. For every $\boldsymbol{k}$ the set of the Bloch periodic functions $\{|n,\boldsymbol{k}\rangle\}$ form an orthonormal basis. Assuming that we are interested in describing the band structure in the vicinity of the band edge $\boldsymbol{k_0}$, and assuming (as it is indeed the case for many semiconductors) that the band edge is at the Γ point ($\boldsymbol{k} = 0$), we can expand the $\{|n,\boldsymbol{k}\rangle\}$ in terms of the band edge periodic functions as

$$|n,\boldsymbol{k}\rangle = \sum_{\nu,\sigma} c_{n,\nu,\sigma}(\boldsymbol{k})|\nu,\sigma\rangle \tag{3.19}$$

where we are considering the band edge eigenfunctions solution of the Scrödinger equation without spin orbit coupling, since it is convenient to include the SOC further in the calculation as a small perturbation. Therefore the band edge eigenfunctions $|n,\boldsymbol{k}\rangle$ are defined as $|\nu,\sigma\rangle = |\nu,\mathbf{0}\rangle \otimes |\sigma\rangle$.
Multiplying the equation 3.18 by $\langle\nu',\sigma'|$ and using orthonormality for $\langle\nu',\sigma'|\nu,\sigma\rangle$ we obtain for the dispersion relation the equation

$$\sum_{\nu,\sigma}\left(\left[E(\mathbf{0}) + \frac{\hbar^2k^2}{2m_0}\right]\delta_{\sigma,\sigma'}\delta_{\nu,\nu'} + \frac{\hbar}{m_0}\boldsymbol{k}\cdot\boldsymbol{P}^{\nu,\nu'}_{\sigma,\sigma'} + \Delta^{\nu,\nu'}_{\sigma,\sigma'}\right)c_{n,\nu,\sigma}(\boldsymbol{k}) = \sum_{\nu,\sigma}E_n(\boldsymbol{k})c_{n,\nu,\sigma}(\boldsymbol{k}) \tag{3.20}$$

where the off diagonal terms read

$$\begin{aligned}\boldsymbol{P}^{\nu,\nu'}_{\sigma,\sigma'} &= \langle\nu'\sigma'|\mathbf{\Pi}|\nu,\sigma\rangle \\ \Delta^{\nu,\nu'}_{\sigma,\sigma'} &= \frac{\hbar}{4m_0^2c^2}\langle\nu'\sigma'|(\boldsymbol{p}\cdot\boldsymbol{\sigma}\times\nabla V_0)|\nu,\sigma\rangle.\end{aligned} \tag{3.21}$$

In general, the Hamiltonian in 3.20 is an infinite dimensional matrix, however, many times one is interested only in a few bands in the vicinity of the band edge, in such a way that the full $\boldsymbol{k}\cdot\boldsymbol{p}$ interaction and the SOC are taken into account only in those bands near the expansion point, while the contribution of the furthest bands is included via quasi degenerate perturbation theory [46], yielding to extra terms in higher order in $\boldsymbol{k}$ in the off diagonal matrix elements.
Therefore, treated as a perturbation on the $\boldsymbol{k}\cdot\boldsymbol{p}$ Hamiltonian 3.15, the SOC term is included in the matrix elements 3.21 between the band edge Bloch functions, and its contribution becomes stronger the smaller is the energy separation Δ_0 between the two bands.

Depending on the type of semiconductor one wants to describe and in which energy bands one is interested, different $\boldsymbol{k}\cdot\boldsymbol{p}$ models considering $N \times N$ $\boldsymbol{k}\cdot\boldsymbol{p}$ Hamiltonians have been constructed and analysed. One of them is the 8×8 Kane model [47, 48] which takes into account the eight bulk energy bands coming from the six-fold degenerate p-like (angular momentum $l = 1$) valence band and the two fold degenerate s-like (angular momentum $l = 0$) conduction band. We do not discuss the model here, but we use the result that, at first order perturbation theory in the vicinity of Γ, the spin orbit coupling term entering the low energy effective Hamiltonian is linear in $\boldsymbol{k}$.
From this result, and noting that the spin orbit coupling conserves Time Reversal symmetry, we conclude that the spin orbit coupling term linear in $\boldsymbol{k}$ entering the Hamiltonian, breaks spatial inversion symmetry.

Inversion symmetry is naturally broken in the bulk in asymmetric crystalline structures (bulk inversion asymmetry, referred to as BIA), like in zinc blend structures without centre of inversion, yielding a spin orbit term in the Hamiltonian which goes under the name of Dresselhaus spin orbit coupling.
However, in semiconducting structure, the inversion symmetry can also be broken via structure asymmetry (structure inversion asymmetry or SIA), for example by engineering heterostructures of different materials yielding a potential difference at the junction, producing an electric field. The spin orbit coupling term entering the effective Hamiltonian for these systems is the so-called Rashba SOC. This is the kind of spin orbit coupling acting in the model for the conventional one dimensional nanowire designed to host Majorana fermions discussed in the previous chapter.
In order to derive the Rashba SOC from the Kane model, one has to use the ***envelope function approximation***, which allows for a treatment of the dynamics of electrons and holes in a crystal structure in presence of external electric (and magnetic) fields.
Applying this procedure in a two dimensional thin film semiconductor, assuming a uniform electric field along the z-direction $\boldsymbol{E} = E\hat{z}$ one obtains a Rashba term in the Hamiltonian which takes the form

$$H_R = \alpha(k_x\sigma_y - k_y\sigma_x). \tag{3.22}$$

Here α is a parameter that depends both on the strength of the external electric field and on the intrinsic properties of the material.

3.2 1D semiconducting quantum wire in a curved geometry and Rashba Superlattice

In this section, we derive the effective one dimensional Hamiltonian for a planary curved semiconducting nanowire living in the two-dimensional x-y plane with Rashba SOC . In doing that, we closely follow [49].

The derivation relies on the thin-wall quantization method developed firstly by Jensen and Koppe in 1971 [50] and later (1981) by da Costa [51]. In this procedure, the particle is constrained to move on n dimensional surface S embedded in a m dimensional space (with $m \geq n+1$) by introducing infinite potential barriers at a distance $\boldsymbol{\delta}$ from the surface and taking the limit $\delta \to 0$. Note that there are $m-n$ normal directions to the surface in which one introduces the confining potential barriers. Because of the strong confinement on the normal direction, the separation between energy levels along this direction is much higher than the one along the tangent directions on the surface. Thus, one can project the total Hamiltonian on the lowest transverse energy level and derive the effective Hamiltonian for the motion along the tangential directions. Jensen and Koppe furthermore demonstrated that the effect of the curvature on the motion of the particle manifests in the dimensional-reduced effective Hamiltonian through the appearance of a potential term which is a function of the extrinsic curvature of the surface. This potential is known as quantum geometric potential (QGP).
It has been showed that the procedure is legitimate also in presence of external electric and magnetic field [52],[53], and in presence of spin orbit coupling [49].

Our starting point for deriving the effecive one dimensional Hamiltonian for a 1D channel nanaowire is the continuum Pauli-Scrödinger equation in the effective-mass approximation to describe the motion of the carriers in a semiconductor in presence of Rashba SOC

$$\left(\frac{\boldsymbol{p}^2}{2m^*} + \boldsymbol{\alpha}\cdot\boldsymbol{\sigma}\times\boldsymbol{p}\right)\Psi = E\Psi \tag{3.23}$$

where Ψ is a two dimensional spinor, $\boldsymbol{\sigma}$ is the vector of the Pauli matrices generating Clifford algebra in the 3D Euclidean space and obeying the anticommutation relation $\{\sigma_i, \sigma_j\} = 2\eta_{ij}$, and $\boldsymbol{\alpha}$ is the vector directed along the direction of the external electric field generating SOC and of magnitude α corresponding to the Rashba SOC constant.

Note that as in 3.22 $\boldsymbol{\alpha} := \alpha\hat{\boldsymbol{z}}$ but for convenience we keep it general in the following derivation. In what follows, we will use Greek indices to indicate the three dimensional tensor component in curved space, while Latin indices will be used to indicate the tensor component in flat, Euclidean three dimensional space.

We can generalize the effective Schrödinger-Pauli equation in a curved space as

$$\begin{aligned} E\psi &= \left[-\frac{\hbar^2}{2m^\star}\left(G^{\mu\nu}\partial_\mu\partial_\nu - G^{\mu\nu}\,\Gamma^\lambda_{\mu\nu}\partial_\lambda\right)\right. \\ &\quad \left. -i\,\hbar\,\mathcal{E}^{\mu\nu\lambda}\,\alpha_\mu\varsigma_\nu\partial_\lambda\right]\psi, \end{aligned} \tag{3.24}$$

where is the inverse metric tensor $G^{\mu\nu}$ in the 3D curved space, and we have used the box operator

$$\Box\phi = G^{\mu\nu}\nabla_\mu\nabla_\nu$$

for the kinetic energy operator in curved space and

$$\Gamma^\lambda_{\mu\nu} = \frac{1}{2}G^{\lambda\beta}(\partial_\nu G_{\beta\mu} + \partial_\mu G_{\beta\nu} - \partial_\beta G_{\mu\nu})$$

is the affine connection. Furthermore, in the SOC term we have introduced $\mathcal{E}^{\nu\nu\lambda} = (||G||)^{-1/2}\epsilon^{\mu\nu\lambda}$ the contravariant Levi-Civita tensor and the ζ_μ, ζ_ν generalize the Pauli matrices in curved space and obey the anticommutation relation $\{\zeta_\mu, \zeta_\nu\} = 2G_{\mu,\nu}$.

We need now to define a set of coordinates to parametrize the 3D space. Given its convenience for describing the motion of a carrier along a curve, we will use the Frenet-Serret reference frame to define our set of local coordinates. In the following we therefore recall the basics characteristic of this frame.

We start by parametrizing the position of the particle moving on a continuous and smooth curve to be parametrized by the vector $\boldsymbol{r}(t)$, with the origin of the vector $\boldsymbol{r}(t)$ coinciding with the origin of a fixed Cartesian reference frame. We can define the infinitesimal arclength ds as

$$\frac{ds}{dt} = \left|\left|\frac{d\boldsymbol{r}}{dt}\right|\right| = \sqrt{\left(\frac{dx}{dt}\right)^2 + \left(\frac{dy}{dt}\right)^2 + \left(\frac{dz}{dt}\right)^2} \tag{3.25}$$

thus, the arclength is given by

$$s(t) = \int_{t_0}^{t} d\tau \sqrt{\left(\frac{dx}{d\tau}\right)^2 + \left(\frac{dy}{d\tau}\right)^2 + \left(\frac{dz}{d\tau}\right)^2}. \tag{3.26}$$

If the sets of points on the curve were initially parametrised by t, one can invert the previous relation for the arclength (as we have assumed the curve to be continuous and smooth) and obtain $\boldsymbol{r}(t(s)) = \boldsymbol{r}(s)$. We have therefore parametrised the curve using the arclength s. The tangent vector to the curve in terms of the arclength reads

$$\boldsymbol{T}(s) = \frac{d\boldsymbol{r}}{ds} = \frac{d\boldsymbol{r}}{dt}\frac{dt}{ds} \tag{3.27}$$

and , due to 3.25 and the fact that $\frac{dt}{ds} = (\frac{ds}{dt})^{-1}$, we automatically have that the tangent vector as a function of s is a unit vector

$$\widehat{\boldsymbol{T}}(s) = \frac{d\boldsymbol{r}}{ds} = \frac{\frac{d\boldsymbol{r}}{dt}}{||\frac{d\boldsymbol{r}}{dt}||}. \tag{3.28}$$

If we now consider $\widehat{\boldsymbol{T}}'(s)$, where the prime means we take the derivative with respect to s, by using the fact that $\widehat{\boldsymbol{T}}(s)$ is a unit norm vector and by differentiating the $\widehat{\boldsymbol{T}}(s)\cdot\widehat{\boldsymbol{T}}(s) = 1$ we get

$\widehat{\boldsymbol{T}}(s) \cdot \widehat{\boldsymbol{T}}^{'}(s) = 0$, meaning that $\widehat{\boldsymbol{T}}^{'}$ is orthogonal to $\widehat{\boldsymbol{T}}$ and directed along the normal direction to the curve. We can define a vector

$$\boldsymbol{\kappa}(s) := \frac{d\boldsymbol{T}}{ds} = \kappa(s)\widehat{\boldsymbol{N}} \tag{3.29}$$

where $\widehat{\boldsymbol{N}}$ indicates the normal direction. The vector $\boldsymbol{\kappa}$ expresses the rate of change of the tangent vector $\widehat{\boldsymbol{T}}$ as one proceeds along the curve, and it is called the curvature vector, and the proportionality factor $\kappa(s)$ is defined as the curvature [54]. Note that the sense of $\widehat{\boldsymbol{T}}^{'}(s)$ is always determined by the curve, whereas the one of $\widehat{\boldsymbol{N}}$ can be chosen arbitrarily. However, by requiring $\widehat{\boldsymbol{N}}$ to be continuous along the curve, the sign of $\kappa(s)$ distinguishes between the concave and convex sides of the curve. In here we follow his convention.
Having introduced the proportionality factor between the tangent and the normal vectors, we are now able to write down the Frenet-Serret equations of motion

$$\begin{aligned} \frac{d\widehat{\boldsymbol{T}}(s)}{ds} &= \kappa(s)\widehat{\boldsymbol{N}}(s) \\ \frac{d\widehat{\boldsymbol{N}}(s)}{ds} &= -\kappa(s)\widehat{\boldsymbol{T}}(s). \end{aligned} \tag{3.30}$$

We are now ready to define our set of coordinates. In fact, considering the planar curve parametrised by the archlength s, we can define the Frenet-Serret coordinates in the three dimensional space in the vicinity of the curve as

$$\boldsymbol{R}(s, q_2, q_3) = \boldsymbol{r}(s) + \widehat{\boldsymbol{N}}(s)q_2 + \widehat{B}q_3 \tag{3.31}$$

where $\widehat{B}$ is the binormal vector, perpendicular to the plane of the curve.

We derive the components of the metric tensor $G_{\mu,\nu}$ by constructing the line element

$$d\boldsymbol{R}^2 = \left(\frac{\partial \boldsymbol{r}(s)}{\partial s} + q_2\frac{\partial \widehat{\boldsymbol{N}}(s)}{\partial s}\right)ds^2 + (\widehat{\boldsymbol{N}}(s))^2 dq_2^2 + \widehat{B}^2 dq_3^2 = (1-\kappa(s)q_2)^2 ds^2 + dq_2^2 + dq_3^2 \tag{3.32}$$

where for the first equality we have used that the orthogonality of the tangent normal and binormal directions (and therefore their dot product is zero), for the second equality we have used the Frenet equation $\partial_s \widehat{\boldsymbol{N}}(s) = -\kappa(s)\widehat{\boldsymbol{T}}(s)$ and that $\widehat{\boldsymbol{N}}(s) \cdot \widehat{\boldsymbol{N}}(s) = \widehat{B} \cdot \widehat{B} = 1$.
The metric tensor is therefore diagonal and reads

$$G = \begin{pmatrix} [1-\kappa(s)q_2]^2 & 0 & 0 \\ 0 & 1 & 0 \\ 0 & 0 & 1 \end{pmatrix},$$

and the determinant $||G|| = (1-\kappa(s)q_2)^2$.
Defining at each point a set of one forms e^i_μ and vector fields e^μ_i such that $e^i_\mu e^\nu_j = \delta^j_i$, following Cartan's dreibein formalism [55], we can write the metric tensor as $G_{\mu\nu} = e^i_\mu \delta_{ij} e^j_\nu$. This enables us to define the generators of the Clifford algebra in curved space as $\zeta_\mu = e^i_\mu \sigma_i$. From the metric above, e^i_μ can be chosen as $e^i_s = (1-\kappa(s)q_2)\widehat{\boldsymbol{T}}^i(s)$, $e^i_{q_2} = \widehat{\boldsymbol{N}}^{i(s)}$,$e^i_{q_3} = \widehat{B}^i$, yielding $\zeta_s = \sigma_t(1-\kappa(s)q_2)$, $\zeta_{q_2} = \sigma_N$ and $\zeta_{q_3} = \sigma_B$, where σ_T is a local Pauli matrix defined as $\sigma_T = \boldsymbol{\sigma}\cdot\widehat{\boldsymbol{T}}$ and the same holds for σ_N and σ_B.

In order to constrain the motion of the carriers along the one dimensional planar curve, we follow the thin-wall quantization procedure introduced above [51]. We thus introduce two strong potential barriers along the normal and binormal direction, indicated as $V_{\lambda_N}(q_2)$ and $V_{\lambda_B}(q_3)$ where λ_N and λ_N are the squeezing parameters.

We moreover define a spinor field χ with norm in Euclidean space given by $N = \int \chi^+ \chi ds dq_2 dq_3$. Therefore by norm conservation we have

$$N = \int \sqrt{||G||}\Psi^+\Psi ds dq_2 dq_3 = \int \chi^+ \chi ds dq_2 dq_3$$

implying $\chi := \Psi \times ||G||^{1/4}$.
In the limit $\lambda_{N,B} \to \infty$, the normal and binormal direction are squeezed around zero, thus, in the limit for $q_{2,3} \to 0$ the equation Scrödinger equation for the spinors χ becomes

$$\begin{aligned} E\,\chi \;\; = \;\; & \left[-\frac{\hbar^2}{2m^\star}\left(\eta^{\mu\nu}\partial_\mu\partial_\nu + \frac{\kappa(s)^2}{4}\right) - i\hbar\,\epsilon^{\mu\nu\lambda}\,\alpha_\mu\sigma_\nu\partial_\lambda \right. \\ & \left. -i\hbar\,\epsilon^{\mu\nu q_2}\,\alpha_\mu\sigma_\nu\frac{\kappa(s)}{2} + V_{\lambda_N}(q_2) + V_{\lambda_B}(q_3)\right]\chi \end{aligned} \tag{3.33}$$

where we have used that in the above limit, the derivatives of Ψ in terms of χ are given by

$$\begin{cases} \partial_{q_2}\psi = \partial_{q_2}\chi + \dfrac{\kappa(s)}{2}\chi \\ \\ \partial^2_{q_2}\psi = \partial^2_{q_2}\chi + \kappa(s)\partial_{q_2}\chi + \dfrac{3}{4}\kappa(s)^2\chi. \end{cases}$$

and that the only non trivial component of the affine connection is $\Gamma^{q_2}_{s,s} = \kappa(s)$.
In equation 3.33 the motion along the tangential direction is coupled with the motion along the normal direction by the spin orbit interaction. However, due to the strong confinement of the normal direction and the high frequency of oscillation of the degrees of freedom along the latter, we can apply adiabatic approximation and separate the two variables, writing the spinor as

$$\chi(s, q_2, q_3) = \chi_T(s)\chi_N(q_2)\chi_B(q_3),$$

where the $\chi_{N,B}$ solve the Schrödinger equation

$$-\frac{\hbar^2}{2m^\star}\partial^2_{q_2,q_3}\;\chi_{N,B} + V_{\lambda_{N,B}}(q_{2,3})\,\chi_{N,B} = E_{N,B}\,\chi_{N,B}.$$

Treating the normal and binormal degrees of freedom as perturbation, the first order derivatives along the latter directions in equation 3.33 vanish. We can therefore write an effective one dimensional Scrödinger-Pauli equation for the degrees of freedom along the tangential direction $\chi(s)$ as

$$\begin{aligned} E\,\chi_T \;\; = \;\; & \left[-\frac{\hbar^2}{2m^\star}\left(\partial_s^2 + \frac{\kappa(s)^2}{4}\right) - i\hbar\alpha_N\sigma_B\partial_s \right. \\ & \left. +i\hbar\alpha_T\sigma_B\frac{\kappa(s)}{2} + i\hbar\alpha_B\left(\sigma_N\partial_s - \sigma_T\frac{\kappa(s)}{2}\right)\right]\chi_T. \end{aligned} \tag{3.34}$$

If we now consider the electric field inducing Rashba spin orbit coupling pointing in the binormal direction as in 3.22 and noticing that $\left(\sigma_N\partial_s - \sigma_T\dfrac{\kappa(s)}{2}\right) = \frac{1}{2}\{\partial_s, \sigma_N\}$ we can write the preceding equation as

$$E\chi_T = \left[\frac{\hat{p}_s^2}{2m^\star} - \frac{\hbar^2\kappa(s)^2}{8m^\star} + i\hbar\frac{\alpha_B}{2}\{\partial_s, \sigma_N\}\right]\chi_T. \tag{3.35}$$

The Hamiltonian derived above is manifestly Hermitian, and it is the correct one dimensional operator describing the motion of the electron in the curve-shaped semiconductor.
The effect of the curvature is incorporated in the local canting of the electron spins, in fact, as shown in figure 3.1 for a serpentine-like wire, the magnitude of the spin orbit remains constant, but the direction rotates in the x-y plane. Assuming for the curved wire the periodic shape in figure 3.1, the 1D SOC Hamiltonian 3.35 is invariant under translations of a full period λ. We thus introduce a tight binding model for the 3.35 and we show that the local spin orbit coupling leads to a superlattice structure.

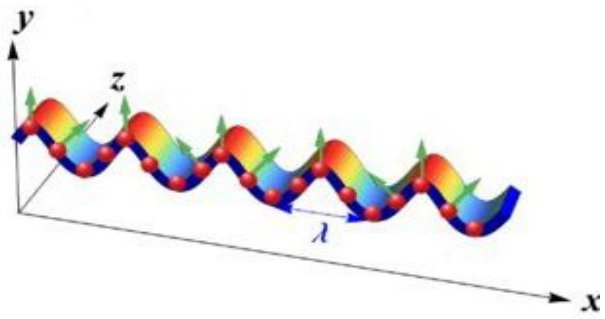

Figure 3.1: The figure represents a serpentine nanowire lying in the x-y plane, which displays a periodic spin canting induced by the curved geometry of the wire.

Tight Binding Model

Le us start by writing the Hamiltonian in equation 3.35 in second quantised form in terms of the spinor field operators $\Psi(s)^\dagger$ and $\Psi(s)$ as

$$H = \sum_{\sigma,\sigma'} \int ds \Psi^\dagger(s)_{\sigma,\sigma'} \left[-\frac{\hbar^2}{2m^*}\partial_s^2 - \frac{i\alpha_r}{2}(\tau_N(s)\partial_s + \partial_s \tau_N(s)) \right] \Psi(s)_{\sigma,\sigma'}. \tag{3.36}$$

As previously, m^* is the effective electron mass, α_r is the strength of the Rashba SOC, and finally, $\tau_N(s) = \boldsymbol{\tau} \cdot \widehat{\boldsymbol{N}}(s)$ is the local Pauli matrix defined in the preceding section.

In the x,y plane of the curved nanowire, the vectors $\widehat{\boldsymbol{T}}$ and $\widehat{\boldsymbol{N}}$ of the Frenet-Serret frame can be written in polar coordinates in terms of an angle θ (depending itself on the arclength s) as

$$\begin{aligned} \widehat{\boldsymbol{T}} &= \{\cos\theta(s), -\sin\theta(s), 0\} \\ \widehat{\boldsymbol{N}} &= \{\sin\theta(s), \cos\theta(s), 0\}. \end{aligned} \tag{3.37}$$

From the previous form of the tangent and normal vectors and using the 3.30 we get that $\theta(s)$ is completely determined by the curvature of the nano wire through

$$\theta(s) = -\int^s \kappa(s^{'})ds^{'}. \tag{3.38}$$

At this point, we take the periodic shape of the wire to assume a simple sinusoidal form, having parametric equation in the Euclidean space $\boldsymbol{r}(x) = \{x, A\sin\left(\frac{2\pi x}{\lambda}\right), 0\}$ where λ indicates the periodicity and A the height.
In the limit $\left(\frac{2\pi A}{\lambda}\right) << 1$, the archlength s can be approximated by the coordinate x, and we can determine the curvature $\kappa(s) \simeq \kappa(x)$ as $\kappa(s) = d\boldsymbol{T}/ds = d^2\boldsymbol{r}(s)/ds$ which, differentiating the equation for the curved wire above, leads to

$$\kappa(x) = -A\left(\frac{2\pi}{\lambda}\right)^2 \sin\left(\frac{2\pi x}{\lambda}\right). \tag{3.39}$$

In order to obtain the tight binding model describing the planary curved nanowire in a discrete lattice space, we need derive the discrete form of the 3.36 in 1D lattice space. The detailed derivation, which makes use of the *finite difference formula* is given in appendix B.
In discrete one dimensional lattice, the atomic sites are separated by the lattice constant a, which we are setting to one throughout the following for simplicity.
In terms of the fermionic field operators on the lattice the Hamiltonian derived in appendix B

reads

$$H = -t\sum_{\sigma,\sigma'}\sum_{i}\Psi^{\dagger}_{i,\sigma}\Psi_{i+1,\sigma'}\delta_{\sigma,\sigma'} - \frac{i\alpha_r}{2}\sum_{\sigma,\sigma'}\sum_{i}\Psi^{\dagger}_{i,\sigma}\tau^{y}_{\sigma,\sigma'}\left[\frac{(\cos\theta_i+\cos\theta_{i+1})}{2}\right]\Psi_{i+1,\sigma'} + \Psi^{\dagger}_{i,\sigma}\tau^{x}_{\sigma,\sigma'}\left[\frac{(\sin\theta_i+\sin\theta_{i+1})}{2}\right]\Psi_{i+1,\sigma'} + h.c. \tag{3.40}$$

where θ_i is the periodic function of the curvature in the discrete space defined as $\theta_i = -\frac{A}{\lambda}2\pi\cos\left(\frac{2\pi i}{\lambda}\right)$. Note that, the terms $(\cos\theta_i+\cos\theta_{i+1})/2$ and $(\sin\theta_i+\sin\theta_{i+1})/2$ imply that the strength of the curvature induced Rashba SOC is encoded on the bonds between nearest neighbouring sites.

The locally varying spin orbit interaction due to the curvature of the wire, breaks translation symmetry on the lattice (as it does in continuum space), as the SOC term on the bond between the first and the second atomic site is different between the SOC on the bond between the second and the third site and so on. However, given its periodic nature, leaves the system invariant if translated of a full period. On the lattice, we can define a unit cell with the same periodicity of the function θ so we recover translation invariance between the cells. The lattice spacing between atomic sites a is taken to be one, thus the lattice constant of the new unit cell is simply given by the number q of atomic sites included in it. Since the period of the function θ depends on the parameter λ, in order for the periodicity of the new unit cells and the periodicity of θ to coincide, we just need to take the new lattice constant $q=\lambda$. Furthermore, in order to account for a possible phase arising between the function θ and the arrangement of the atomic sites in the new unit cells (e.g when the origin of the periodic function θ does not coincide with the first atomic position of the lattice unit cell), we introduce a displacement phase ϕ and define the atomic positions within the new unit cell as $x_n = \frac{n}{\lambda} = \left(\frac{n}{q}+\frac{\phi}{2\pi}\right)$. In terms of the positions x_n, the function θ reads $\theta(x_n) = -2\pi\frac{A}{\lambda}\cos(2\pi x_n)$.
The lattice formed by these unit cells with enhanced lattice constant is called superlattice and the corresponding unit cells, superlattice unit cells.
With the superlattice structure constructed as above, we want to re-write the fermionic field operators Ψ_i and $\Psi^{\dagger}_i$ in terms of creation and annihilation operators $c^{\dagger}_{n,i}$, $c_{n,i}$ on superlattice sites. In the latter operators, the index $n=1,2,...,q$ runs over the different atomic sites within the unit cell, while the index $i=1,2,...,N/q$ runs over the superlattice cells. With this notation, we can write the Hamiltonian 3.40 as

$$H = \sum_{\sigma,\sigma'}\sum_{n=1}^{q-1}\sum_{i=1}^{N/q} c^{\dagger}_{n,i,\sigma}\left[-t\delta_{\sigma,\sigma'} + \frac{i\alpha_r}{2}\tau^{y}_{\sigma,\sigma'}\left(\frac{\cos(\theta(x_n))+\cos(\theta(x_{n+1}))}{2}\right)\right]c_{n+1,i,\sigma'} \tag{3.41}$$

$$+c^{\dagger}_{n,i,\sigma}\left[+\frac{i\alpha_r}{2}\tau^{x}_{\sigma,\sigma'}\left(\frac{\sin(\theta(x_n))+\sin(\theta(x_{n+1}))}{2}\right)\right]c_{n+1,i,\sigma'} \tag{3.42}$$

$$+c^{\dagger}_{q,i,\sigma}\left[-t\delta_{\sigma,\sigma'} + \frac{i\alpha_r}{2}\tau^{y}_{\sigma,\sigma'}\left(\frac{\cos(\theta(x_q))+\cos(\theta(x_1))}{2}\right)\right]c_{1,i+1,\sigma'} \tag{3.43}$$

$$+c^{\dagger}_{q,i,\sigma}\left[\frac{i\alpha_r}{2}\tau^{x}_{\sigma,\sigma'}\left(\frac{\sin(\theta(x_q))+\sin(\theta(x_1))}{2}\right)\right]c_{1,i+1,\sigma'} \tag{3.44}$$

where $\theta(x_n)$ is defined as above, yielding therefore $\theta(x_q) = -\frac{A}{\lambda}\cos\left[2\pi\left(1+\frac{\phi}{2\pi}\right)\right]$ and $\theta(x_1) = -\frac{A}{\lambda}\cos\left[2\pi\left(\frac{1}{q}+\frac{\phi}{2\pi}\right)\right]$.

3.2.1 Momentum Space

In order to write the tight binding Hamiltonian in momentum space, we transform the operators $c^{\dagger}_{n,i}$ and $c_{n,i}$ as

$$c^{\dagger}_{n,i} = \frac{1}{\sqrt{2\pi}} \sum_{k}^{k=N/q} e^{-i(k\cdot i)} c^{\dagger}_{n,k}$$

and

$$c_{n,i} = \frac{1}{\sqrt{2\pi}} \sum_{k=1}^{k=N/q} e^{i(k\cdot i)} c_{n,k}$$

. Notice that, since in real lattice space we have defined a superlattice with unit cell with enlarged lattice constant q, in reciprocal space (momentum space), the first Brillouin Zone is reduced to the momenta $\left[-\frac{\pi}{q}, \frac{\pi}{q}\right]$.The reduced Brillouin zone is referred to as Mini Brillouin zone, or mBZ. As a consequence, electronic level corresponding to momenta k of the initial Brillouin zone outside mBZ, are mapped inside the reduced Brillouin zone and yield to the band folding of the energy spectrum.
The Hamiltonian in k-space reads

$$\begin{aligned} H = \sum_{\sigma,\sigma'} \sum_{n=1}^{q-1} \sum_{k=1}^{N/q} & c^{\dagger}_{n,k,\sigma} \left[-t\delta_{\sigma,\sigma'} + \frac{i\alpha_r}{2} \tau^{y}_{\sigma,\sigma'} \left(\frac{\cos\left(\theta(x_n)\right) + \cos\left(\theta(x_{n+1})\right)}{2} \right) \right] c_{n+1,k,\sigma'} \\ & + c^{\dagger}_{n,k,\sigma} \left[+ \frac{i\alpha_r}{2} \tau^{x}_{\sigma,\sigma'} \left(\frac{\sin\left(\theta(x_n)\right) + \sin\left(\theta(x_{n+1})\right)}{2} \right) \right] c_{n+1,k,\sigma'} \\ & + c^{\dagger}_{q,k,\sigma} \left[-t\delta_{\sigma,\sigma'} + \frac{i\alpha_r}{2} \tau^{y}_{\sigma,\sigma'} \left(\frac{\cos\left(\theta(x_q)\right) + \cos\left(\theta(x_1)\right)}{2} \right) \right]] e^{ik} c_{1,k+1,\sigma'} \\ & + c^{\dagger}_{q,k,\sigma} \left[\frac{i\alpha_r}{2} \tau^{x}_{\sigma,\sigma'} \left(\frac{\sin\left(\theta(x_q)\right) + \sin\left(\theta(x_1)\right)}{2} \right) \right] e^{ik} c_{1,k+1,\sigma'} . \end{aligned} \tag{3.45}$$

In order to derive the band structure of the Hamiltonian above, one defines the spinor

$$\boldsymbol{C}_k = \left(c_{n_1,k,\uparrow}, c_{n_1,k,\downarrow}, c_{n_2,k,\uparrow}, ..., c_{n_q,k,\downarrow} \right)^T \tag{3.46}$$

which allows to write the Hamiltonian in k space in matrix form $H = \sum_k \boldsymbol{C}_k H_k \boldsymbol{C}_k$, and find the dispersion relation ϵ_k diagonalizing H_k.
Explicit form of H_k for $q = 3$ and $q = 4$ is given in appendix C.

Chapter 4

A Toy Model for Topological Superconductivity in Rashba Superlattice

In order to study the influence of the curved geometry of the semiconducting wire on the topological superconducting phase, we begin by introducing a simplified toy model in which we consider the conventional wire hosting Majorana modes presented in chapter 1 with an additional modulated Rashba SOC orthogonal to the constant SOC.
We start by analysing the bulk band structure of the semiconducting wire alone, in order to enlighten the influence of the locally-varying Rashba SOC, and we proceed by first introducing a Zeeman splitting in the bulk band structure and then adding the proximity induced s-wave superconductivity, in order to study the full system designed to host Majorana modes.

4.1 Toy Model Hamiltonian

We introduce here the effective $\boldsymbol{k}\cdot\boldsymbol{p}$ Hamiltonian for the semiconducting wire with a locally varying term depending on a periodic function of the coordinates set along the z-direction and constant Rashba SOI set along the y direction. The Hamiltonian reads

$$H_{SOC} = \sum_{\sigma,\sigma'} \int dx \Psi^{\dagger}_{\sigma}(x) \left[-\frac{\partial_x^2}{2m} + \frac{i\alpha_m}{2}\{\kappa(x), \partial_x\}\tau^z_{\sigma,\sigma'} + \alpha_r \tau^y_{\sigma,\sigma'}\partial_x \right] \Psi_{\sigma'}(x) \tag{4.1}$$

Where we have set $\hbar = 1$. The term $i\alpha_m\{\kappa(x), \partial_x\}\tau^z_{\sigma,\sigma'}/2$ is the one-dimensional Rashba SOC that results from an effective electric field along the $\hat{y}$ direction, whereas the term $\alpha_r\tau^y_{\sigma,\sigma'}\partial_x$ is the Rashba SOC resulting from an effective electric field along the $\hat{z}$ direction. The $\tau^y_{\sigma,\sigma'}$ and $\tau^z_{\sigma,\sigma'}$ are, respectively, the second and the third Pauli matrices acting on spin space, and α_m and α_r are the strength of the SOC fields in the corresponding directions.
The anticommutator $\{\kappa(x), \partial_x\}$ between $\kappa(x)$ and the operator ∂_x is the local term that accounts for the modulation of the Rashba field along the $\hat{z}$ direction: $\kappa(x)$ is in fact a periodic function and, for simplicity, we assume $\kappa(x) = \cos\left(\frac{2\pi}{\lambda}x\right)$.

Tight Binding Model

In order to write the tight binding model for the system constituted by the preceding Hamiltonian for the semiconducting wire, we first discretize (4.1) on a one-dimensional lattice using the procedure that makes use of the finite differences method already showed for the previous section (details can be found in appendix B). As a consequence, for the terms in 4.1 containing derivatives, we will get nearest neighbours hopping terms of the form $\Psi^{\dagger}_{i,\sigma}\Psi_{j,\sigma} + h.c$ where

$j = i + a$, where a is the lattice spacing, which we set to one for simplicity. The term containing the anticommutator in the Hamiltonian (4.1), can be discretized using the product rule for finite differences as showed in appendix B. With this procedure we find

$$\Psi^{\dagger}_{i,\sigma} \frac{[\kappa_i + \kappa_j]}{2} \tau^z_{\sigma,\sigma'} \Psi_{j,\sigma'} + h.c$$

where k_i and k_j denote the periodic function on site i and j. This implies that the Rashba spin orbit strength is acting on the bond between nearest neighbours, yielding a modulated nearest neighbours hopping.
The latter, as analogous to the model introduced in chapter 3, breaks translation invariance between neighbouring sites on the lattice. Nevertheless, we can recover translation invariance between adjacent cells redefining a unit lattice cell with the same periodicity of the modulation of the SOC, in the exact same fashion of the previous chapter. The superlattice period is therefore $q = \lambda$ and, including the displacement phase ϕ the atomic positions in the superlatice cell are given by $\frac{n}{\lambda} = \left(\frac{n}{q} + \frac{\phi}{2\pi}\right)$. In the latter superlattice structure, we introduce the fermionic creation and annihilation operators $c^{\dagger}_{n,i,\sigma}$ and $c_{n,i,\sigma}$ where, sticking with the notation introduced previously, the index $n = 1, 2, ...q$ runs over the atomic sites within the unit cell, while the index $i = 1, 2, ...N/q$ runs over the number of superlattice cells and the index σ is the spin index. In term of these operators, the tight binding Hamiltonian is given by

$$\begin{aligned} H^{tb}_{SOC} = &\sum_{\sigma,\sigma'} \sum_{n=1}^{q} \sum_{i=1}^{N/q} c^{\dagger}_{n,i,\sigma} \left[-t\delta_{\sigma,\sigma'} + \alpha_r \tau^y_{\sigma,\sigma'} + \alpha_m \tau^z_{\sigma,\sigma'} \left(\frac{\kappa_n + \kappa_{n+1}}{2} \right) \right] c_{n+1,i,\sigma'} \\ &+ c^{\dagger}_{q,i,\sigma} \left[-t\delta_{\sigma,\sigma'} + \alpha_r \tau^y_{\sigma,\sigma'} + \alpha_m \tau^z_{\sigma,\sigma'} \left(\frac{\kappa_q + \kappa_1}{2} \right) \right] c_{1,i+1,\sigma'} + h.c \end{aligned} \tag{4.2}$$

where κ_n, κ_q, κ_1 are respectively given by $\kappa_n = \cos\left[2\pi\left(\frac{n}{q} + \frac{\phi}{2\pi}\right)\right]$,$\kappa_q = \cos\left[2\pi\left(1 + \frac{\phi}{2\pi}\right)\right]$ and $\kappa_1 = \cos\left[2\pi\left(\frac{1}{q} + \frac{\phi}{2\pi}\right)\right]$. Here, ϕ is the phase that accounts for different configurations of the superlattice unit cells as previously explained.

Momentum Space

In order to write the Hamiltonian in momentum space we first define the Fourier Transform

$$c^{\dagger}_{n,i} = \frac{1}{\sqrt{2\pi}} \sum_{k=1}^{k=N/q} e^{-i(k\cdot i)} c^{\dagger}_{n,k}$$

and

$$c_{n,i} = \frac{1}{\sqrt{2\pi}} \sum_{k=1}^{k=N/q} e^{i(k\cdot i)} c_{n,k}.$$

In terms of the latter, the Hamiltonian in momentum space reads

$$\begin{aligned} H_{SOC} = &\sum_{\sigma,\sigma'} \sum_{n=1}^{q} \sum_{k=1}^{N/q} c^{\dagger}_{n,k,\sigma} \left[-t\delta_{\sigma,\sigma'} + \alpha_r \tau^y_{\sigma,\sigma'} + \alpha_m \tau^z_{\sigma,\sigma'} \left(\frac{\kappa_n + \kappa_{n+1}}{2} \right) \right] c_{n+1,k,\sigma'} \\ &+ c^{\dagger}_{q,k,\sigma} \left[-t\delta_{\sigma,\sigma'} + \alpha_r \tau^y_{\sigma,\sigma'} + \alpha_m \tau^z_{\sigma,\sigma'} \left(\frac{\kappa_q + \kappa_1}{2} \right) \right] e^{k\cdot i} c_{1,k,\sigma'} + h.c \end{aligned} \tag{4.3}$$

We define the spinor $\boldsymbol{C}_k = \left(c_{n_1,k,\uparrow}, c_{n_1,k,\downarrow}, c_{n_2,k,\uparrow}, ..., c_{n_q,k,\downarrow}\right)^T$ that allows us to write the Hamiltonian in matrix form $\boldsymbol{C}^{\dagger}_k \boldsymbol{H}_k \boldsymbol{C}_k$ and diagonalize $\boldsymbol{H}_k$ in order to find the dispersion relation and therefore, the bulk band structure. Explicit form of $\boldsymbol{H}_k$ are given in appendix C.

4.2 Normal Phase Bulk Bands

In the following, we consider the energy spectrum for different periodicities of the superlattice unit cell and how the band structure of the semiconducting wire is modified.

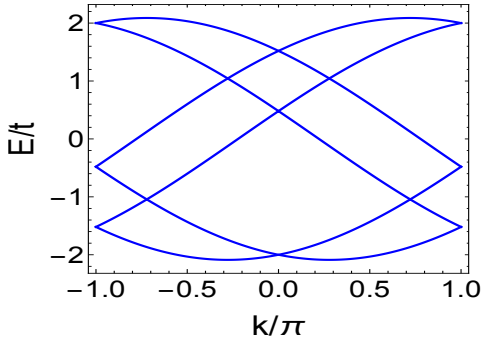

(a) Band Structure $q = 3$. In here, only the constant Rashba SOC along y is turned on, leading to the typical momentum-dependent spin splitting of the energy bands. The strength of the Rasha SOI is set at $\alpha_r/t = 0.2$

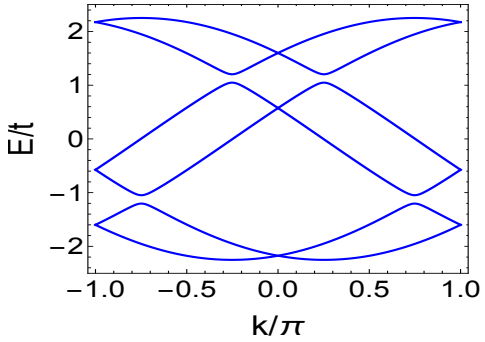

(b) Band structure for $q = 3$. Both component of the Rashba SOC are present, and we observe insulating gap opening at unpinned point the first mBZ for all integer filling fractions $\nu = 1/3$, $\nu = 2/3$. The strength of the constant Rasha SOC is set at $\alpha_r/t = 0.2$ while the strength of the moduleated Rashba SOC along z is set to $\alpha_m/t = 0.8$.

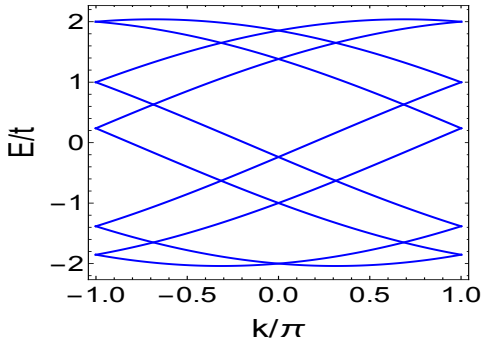

(c) Band Structure $q = 5$. In here, only the constant Rashba SOC along y is turned on, leading to the typical momentum-dependent spin splitting of the energy bands. The strength of the Rasha SOI is set at $\alpha_r/t = 0.2$

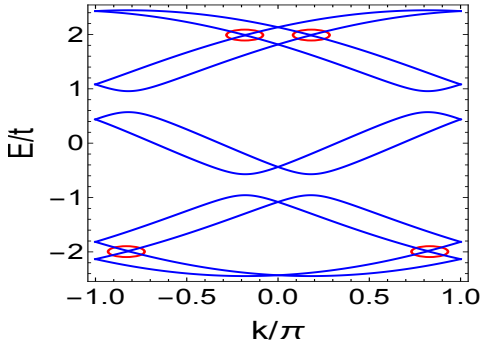

(d) Band structure for $q = 5$. Both component of the Rashba SOC are present, and we observe insulating gap opening at unpinned point the first mBZ for all integer filling fractions $\nu = 1/5$, $\nu = 2/5$,$\nu = 3/5$ and $\nu = 4/5$. The gap at $\nu = 1/5$ and $\nu = 3/5$ cannot be appreciated in this figure, and the red circles indicate that a zoom on those bands crossings is required. The latter will be provided in the next figure. The strength of the constant Rasha SOC is set at $\alpha_r/t = 0.2$ while the strength of the moduleated Rashba SOC along z is set to $\alpha_m/t = 0.8$.

Figure 4.1: Energy bands for $q = 3$ and $q = 5$ atomic sites in a superlattice unit cell. Both the superlattice periodicity show the same behaviour when introducing the modulated component of the SOC orthogonal to the constant one.

Figure 4.1 shows the band structure when we consider a superlattice unit cell containing an odd number q of atomic sites. More precisely, in the 4.1, we have plotted the energy bands for $q = 3$ and $q = 5$. The band structure in 4.1 demonstrates that the system, in presence of the locally varying SOC, undergoes a metal-insulator phase transition at unpinned points in the first mBZ. In fact, the energy spectra in 4.1(b) and 4.1(d) display the band insulating gap opening at integer filling fractions $\nu = n/q$, with $n = 1, ..., q$, at unpinned points. Note that the lowest energy bands at $\nu = 1/5$ and the highest at $\nu = 4/5$ in 4.1(d) indeed do not cross as it is showed

in 4.2 where we zoom on the filling fractions $\nu = 1/5$ and $\nu = 4/5$.

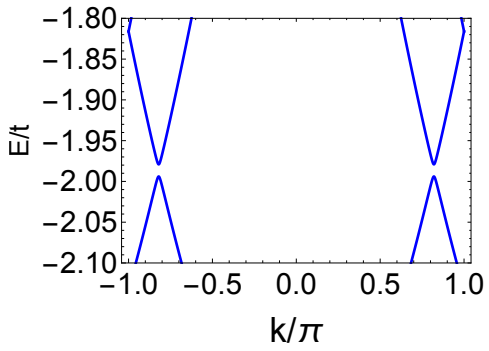

(a) Zoom on the lowest energy bands for $q = 5$, where we can appreciate the gap opening at $\nu = 1/5$. The strength of the constant Rasha SOC is set at $\alpha_r/t = 0.2$ while the strength of the moduleated Rashba SOC along z is set to $\alpha_m/t = 0.8$.

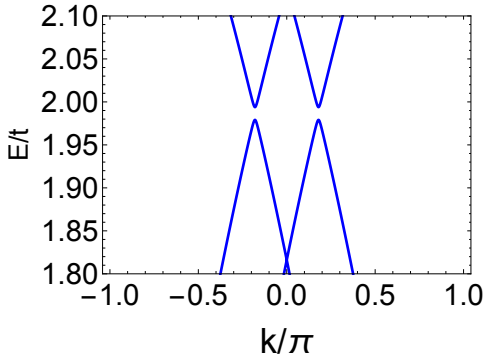

(b) Zoom on the highest energy bands for $q = 5$, where we can appreciate the gap opnening at filling $\nu = 4/5$. The strength of the constant Rasha SOC is set at $\alpha_r/t = 0.2$.

Figure 4.2

Figure 4.3 shows instead the bulk band structure when an even periodicity of the superlattice cell is chosen.
Looking at 4.3(a) and 4.3(b), we observe that, as we introduced the modulated component of the Rashba SOC along z-direction, when $q = 4$, there is no insulating gap opening at any filing fraction. On the other hand, if we consider the 4.3(d) showing the band structure for $q = 6$, we see insulating gap opening at unpinned points in the first mBZ for the filling fractions $\nu = 2/6$ and $\nu = 4/6$, while, no gap opening occurs at $\nu = 1/6$ and $\nu = 5/6$: the zoom provided in figure 4.4 is meant to convince the reader that indeed in the case of $q = 6$ the lowest and the highest energy bands cross even in presence of the modulated SOC. The filling fractions $\nu = 2/6$ and $\nu = 4/6$ indeed correspond to the filling fractions $\nu = 1/3$ and $\nu = 2/3$ in the case analysed previously for $q = 3$ where the insulating gap are open, meaning that he band structure in 4.3(d) for $q = 6$ shows consistency both with the case of superlattice periodicities $q = 3$ and $q = 4$. We have therefore observed that the introduction of a modulated SOC induces metal-insulator transitions at integer filling fractions $\nu = n/q$ with n and q co-primes and q odd.

We want now to understand if the absence of insulating gap opening at any filling fraction for q even is due to the specific periodic shape of the superlattice coinciding with the periodic modulation of the SOC. Thus, we analyse the band structure for the preceding cases $q = 4$ and $q = 6$ when the displacement phase ϕ has a non trivial value.
We start by considering the case $q = 4$, where the band structure plotted in 4.5 displays a gap at half filling which was closed in the previous plot obtained for $\phi = 0$, implying that, as one allows for different displacements of the atomic sites in the superlattice structure, the locally varying SOC induces metal-insulator phase transitions in the system at half filling.

Having found that the bulk spectrum of the system acquires a gap at zero energy as one varies the parameter ϕ, we further analyse the potential occurrence of a topological phase transition corresponding to a closing and a subsequent reopening of the insulating gap as sweeping the displacement phase ϕ. Figure 4.6 displays the band structure for an open, finite, chain with $q = 4$ atomic sites per unit superlattice cell as ϕ is swept from 0 to 1. Here, we observe that the energy spectrum, gapless at $\phi = 0$, acquires an insulating gap for small values of ϕ, which closes and opens again as one continues sweeping ϕ along a full period. After the first gap closing, we notice the appearance of zero energy states localised at the end of the chain, leading the chain in the topological insulating phase.

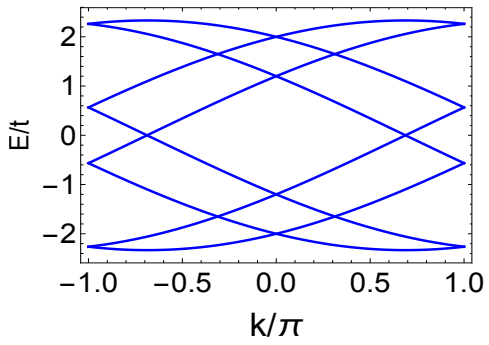

(a) Band Structure $q = 4$. In here, only the constant Rashba SOC along y is turned on, leading to the typical momentum-dependent spin splitting of the energy bands. The strength of the Rasha SOI is set at $\alpha_r/t = 0.4$

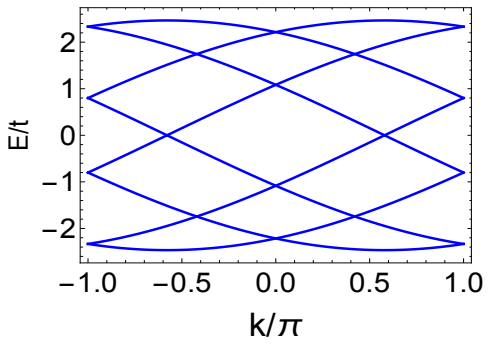

(b) Band structure for $q = 4$. Both component of the Rashba SOC are present, and we observe no insulating gap opening in the first mBZ for any filling fraction. The strength of the constant Rasha SOC is set at $\alpha_r/t = 0.4$ while the strength of the moduleated Rashba SOC along z is set to $\alpha_m/t = 0.8$.

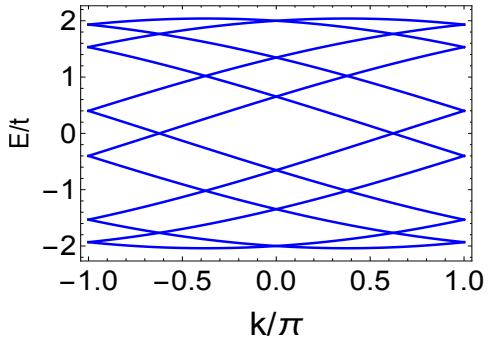

(c) Band Structure $q = 6$. In here, only the constant Rashba SOC along y is turned on, leading to the typical momentum-dependent spin splitting of the energy bands. The strength of the Rasha SOC is set at $\alpha_r/t = 0.4$

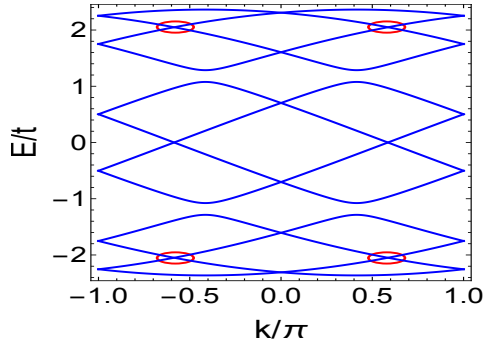

(d) Band structure for $q = 6$. Both component of the Rashba SOC are present, and we observe insulating gap opening at unpinned points the first mBZ for the filling fractions $\nu = 1/3$ and $\nu = 2/3$. We have evidentiated the band crossings at filling $\nu = 1/6$ and $\nu = 5/6$ zince we zoom on them in the next figure and we show that, as opposite of what happens in the case $q = 5$ there is no gap opening for these filling fractions. The strength of the constant Rasha SOC is set at $\alpha_r/t = 0.4$ while the strength of the moduleated Rashba SOC along z is set to $\alpha_m/t = 0.8$.

Figure 4.3: Energy bands for $q = 4$ and $q = 6$ atomic sites in a superlattice unit cell. Here we see no insulating gap opening when $q = 4$ whereas, for $q = 6$, the insulating gaps open only at filling fractions $\nu = 1/3$ and $\nu = 2/3$.

We have therefore showed that the locally varying SOC promotes the generation of a topological insulating phase which hosts conducting states at the edge.
In order to classify the topological phase, we need to look at the symmetries possessed by the system. The effective Hamiltonian we are studying, includes the electron kinetic energy and two spin orbit coupling terms. Those terms alone, do not break Time reversal symmetry, meaning that the system is symmetric under $\boldsymbol{T} H_k \boldsymbol{T}^{-1} = H_{-k}$ with $\boldsymbol{T}$ which squares to -1 for spin 1/2 particles. Furthermore, as the sites in the unit superlattice cell are assumed to be occupied by atoms of the same kind, the system possess also the unitary sublattice symmetry (chiral symmetry), meaning that if one takes the mid point of the unit cell and reverses the sites, the system remains unchanged. Finally, it is evident that the system possesses also the anti-unitary Particle-Hole symmetry, which squares to -1 for spinful electrons.

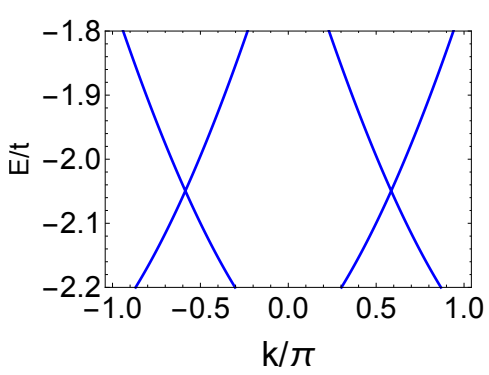

(a) Zoom on the lowest energy bands for $q = 6$, where we can appreciate the gap opening at $\nu = 1/5$.The strength of the constant Rasha SOC is set at $\alpha_r/t = 0.4$ while the strength of the moduleated Rashba SOC along z is set to $\alpha_m/t = 0.8$.

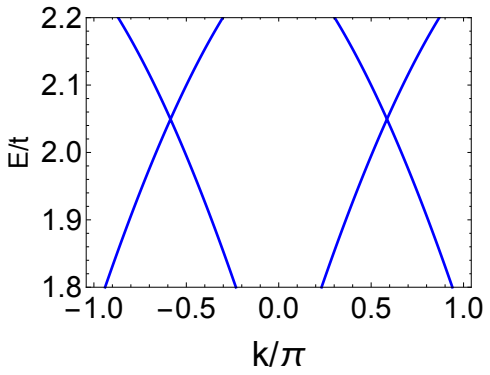

(b) Zoom on the highest energy bands for $q = 6$, where we can appreciate the gap opnening at filling $\nu = 4/5$. The strength of the constant Rasha SOC is set at $\alpha_r/t = 0.4$.

Figure 4.4

Under these considerations, we can conclude that the system is in the chiral symplectic class CII of the Altland-Zirnbauer periodic table. In one dimension, the topological invariant associated to this symmetry class is an integer (Z) number.

The analysis for the case $q = 6$ underlines a different behaviour of the system. In fact, as showed in 4.7, no metal-insulator transition is induced at half filling, since the system remains gapless as one sweeps ϕ in the whole interval from 0 to 1, implying that the energy level crossing at zero energy with this superlattice periodicity, is protected by an additional symmetry.
The study of the band structure for $q = 4$ and $q = 6$ with non zero displacement phase has revealed also that the band crossing at filling fractions $\nu = 1/q$ and $\nu = (q-1)/q$ remain unaffected by the presence of the SOC, implying that this crossings are robust against the local perturbation and they are protected by and additional hidden symmetry of the system.

The preceding analysis has therefore pointed out that, for superlattices with periodicity corresponding to $4n$, with n positive integer, the modulation of the SOC induces a metal- insulator transition at half filling for non trivial values of ϕ, and the resulting insulating phase is driven into a topological phase hosting zero energy edge states by sweeping the parameter ϕ.

The previous results are limited to specific superlattice configuration, therefore someone can regard them as rather irrelevant for withdrawing general physical conclusions on the system. However, we wish to point out that the preceding analysis has been done in the spirit of partially reproduce already known results from [31] in the case of a conventional semiconducting wire where the superlattice structure is induced by the externally modulated SOC rather than the curved geometry of the wire. The results we have found are indeed in agreement with the results in [49], thus enforcing our initial motivation for considering this system as a simplified model for studying the effects of the Rashba superlattice on the topology of the semiconductor-superconductor heterostructure discussed in chapter three.

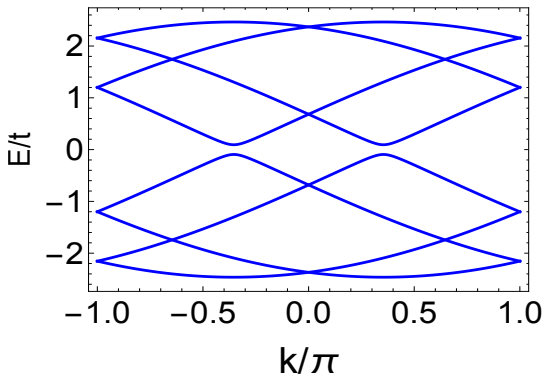

Figure 4.5: Plot of the band structure for $q = 4$ atomic sites in the unit superlattice cell. The displacement phase ϕ equals $2\pi/5$, and we observe the appearance of an insulating gap at half filling. The strength of the constant Rashba SOC is $\alpha_r/t = 0.4$ while the strength of the modulated SOC is $\alpha_m/t = 0.8$.

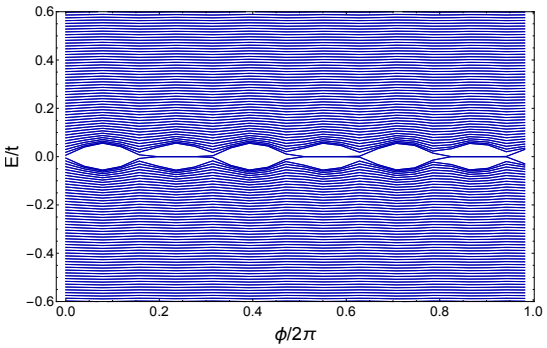

Figure 4.6: Band structure for the system with $q = 4$ atomic sites in a unit cell, obtained by diagonalizing an open chain containing $N = 600$ atoms. The strength of the constant SOC is $\alpha_r/t = 0.4$, whereas the strength of the modulated SOC is $\alpha_m/t = 1$.

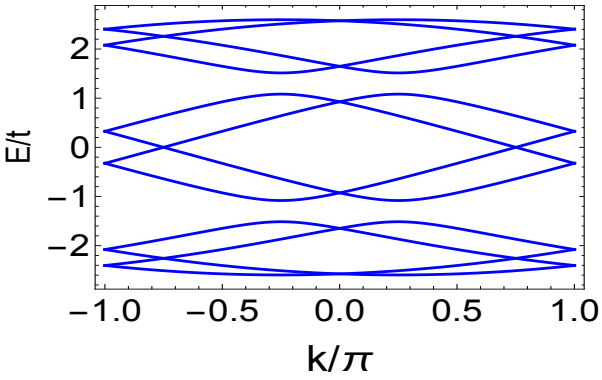

Figure 4.7: Plot of the band structure for $q = 6$ atomic sites in the unit superlattice cell. The displacement phase ϕ equals $2\pi/5$, the strength of the constant Rashba SOC is $\alpha_r/t = 0.4$ while the strength of the modulated SOC is $\alpha_m/t = 0.8$. In here for the filling fractions $\nu = 1/6$, $\nu = 1/2$ and $\nu = 5/6$ there is no insulating gap opening.

4.2.1 Bulk Band analysis with the additional Magnetic Field

Here, we add the magnetic field along the x-direction, orthogonal to the SOC. At tight binding, the Zeeman term reads

$$H_Z^{tb} = \sum_{\sigma,\sigma'} \sum_{n=1}^{q} \sum_{i=1}^{N/q} c^{\dagger}_{n,i,\sigma} B \tau^{x}_{\sigma,\sigma'} c_{n,i,\sigma'} \tag{4.4}$$

where the operators $c^{\dagger}_{n,i,\sigma}$ and $c_{n,i,\sigma}$ are the fermionic creation and annihilation operator in the notation already introduced previously, and B is the strength of the effective magnetic field. Fourier transforming in momentum space, using the same convention for the Fourier operators introduced in chapter two: $c^{\dagger}_{n,i} = \frac{1}{\sqrt{2\pi}} \sum_k e^{-i(k\cdot i)} c^{\dagger}_{n,k}$ and $c_{n,i} = \frac{1}{\sqrt{2\pi}} \sum_k e^{i(k\cdot i)} c_{n,k}$ we get

$$H_Z = \sum_{\sigma,\sigma'} \sum_{n=1}^{q} \sum_{k=1}^{N/q} c^{\dagger}_{n,k,\sigma} B \tau^{x}_{\sigma,\sigma'} c_{n,k,\sigma'} \tag{4.5}$$

The tight binding, momentum space Hamiltonian we are considering here is therefore given by $H = H_{SOC} + H_Z$. The energy eigenvalues are obtained diagonalising the matrix H_k obtained when putting H in matrix form $\boldsymbol{C}^{\dagger}_k H_k \boldsymbol{C}_k$, using the same definition of $\boldsymbol{C}$ as before. In what follows, we analyse the band structure for different superlattice periodicities.

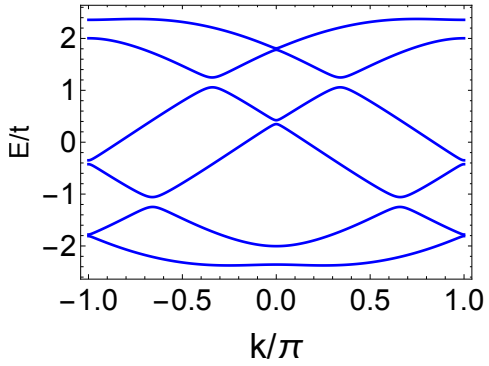

(a) Band structure $q = 3$, $B = 0.3$. The magnetic field lifts the Kramer degeneracy in $k = 0$ and $k = \pm\pi$. In figure, we observe the field induced gap at $k = 0$ between the two lowest energy bands (filling fractions $\nu < 1/3$), and at $k = \pi$ at the edge of the mBZ between the two highest energy bands. The strength of the constant Rasha SOC is set at $\alpha_r/t = 0.2$ while the strength of the modulated Rashba SOC along z is set to $\alpha_m/t = 0.8$.

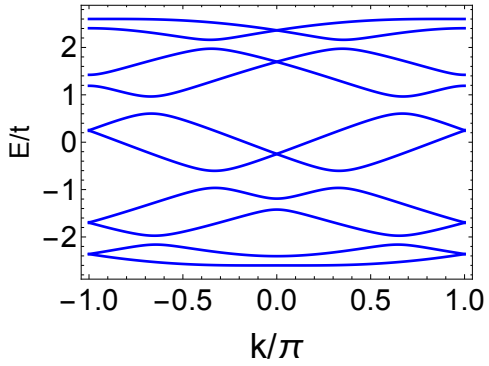

(b) Band structure $q = 5$, $B = 0.3$. The magnetic field lifts the Kramer degeneracy in $k = 0$ and $k = \pm\pi$. In figure, we observe the field induced gap at $k = 0$ between the two lowest energy bands (filling fractions $\nu < 1/5$), and at $k = \pi$ at the edge of the mBZ between the two highest energy bands. The strength of the constant Rasha SOC is set at $\alpha_r/t = 0.2$.

Figure 4.8: The figures show band structure for the semiconducting wire with the introduction of an external magnetic field for odd superlattice period.

Figure 4.8 shows the band structure for odd superlattice periodicity, $q = 3$ and $q = 5$ atoms in the unit cell, in presence of the magnetic field. The latter breaks Time Reversal symmetry in the system, lifting the Kramer degeneracy at the Kramer invariant points $k = 0$ and $k = \pm\pi$. Looking at the lowest energy bands in both 4.8(a) and 4.8(b) we observe that, when the Fermi level resides within the gap at $k = 0$ induced by the Zeeman splitting, one encounters only one pair of Fermi points and the system appears effectively spinless.
In presence of the magnetic field, the band structures for odd superlattice periodicity with externally modulated SOC present metal-insulator phase transitions at unpinned points in the first mBZ at all integer filling fractions $\nu = n/q$ as we saw in the previous analysis.

Figure 4.9 shows the band structure of the system with broken Time Reversal symmetry for even periodicity of the superlattice unit cell, in particular, we consider (as before), $q = 4$ and $q = 6$, atomic sites in the unit cell. As observed for odd superlattice periodicity, the magnetic field lifts the Kramer degeneracy at the Kramer invariant points $k = 0$ and $k = \pm\pi$. Notice that, for an even number of atomic sites in the unit cell, the edges of the first Brillouin Zone are folded at the Γ point in the first mini-Brillouin Zone in the reciprocal superlattice space, thus the splitting of the Kramer invariant points occurs at $k = 0$ in the first mBZ for both the lowest energy bands (originally degenerate in $k = 0$) and the highest energy bands (originally

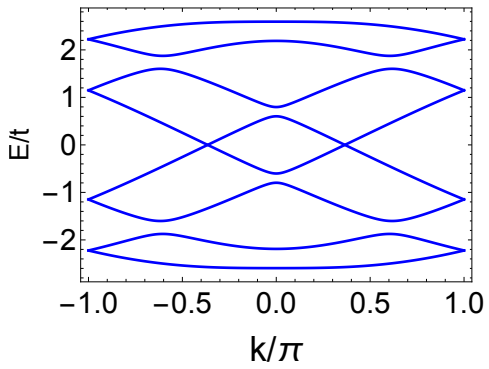

(a) Band structure $q = 4$, $B = 0.3$. In figure, we observe the field induced gap at $k = 0$ between the two lowest energy bands (filling fractions $\nu < 1/4$). When the superlattice unit cell contains an even number of atomic sites, the energy eigenvalues at $\pm\pi$ are folded in zero, thus also for he two highest energy bands, the field induced gap is at $k = 0$. The strength of the constant Rasha SOC is set at $\alpha_r/t = 0.4$ while the strength of the modulated Rashba SOC along z is set to $\alpha_m/t = 0.8$.

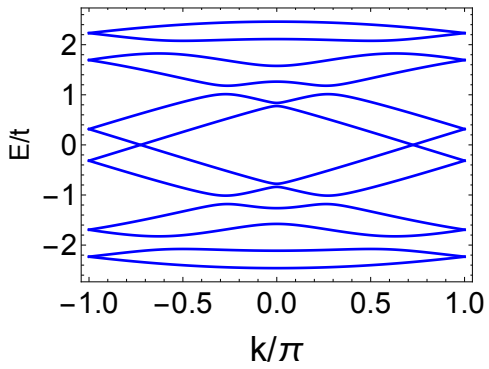

(b) Band structure $q = 6$, $B = 0.3$. In figure, we observe the field induced gap at $k = 0$ between the two lowest energy bands (filling fractions $\nu < 1/6$). When the superlattice unit cell contains an even number of atomic sites, the energy eigenvalues at $\pm\pi$ are folded in zero, thus also for he two highest energy bands, the field induced gap is at $k = 0$. The strength of the constant Rasha SOC is set at $\alpha_r/t = 0.4$ while the strength of the modulated SOC along z is set to $\alpha_m/t = 0.8$.

Figure 4.9: The figures show band structure for the semiconducting wire with the introduction of an external magnetic field for even superlattice period.

degenerated at $\pm\pi$).
The band structures for $q = 4$ and $q = 6$ show that the breaking of the Time Reversal symmetry allows for insulating gap openings at filling fractions $\nu = 1/q$ and $\nu = (q-1)/q$, which are never possible in absence of the magnetic field as we saw in the previous section.
However, even with broken Time Reversal, the band crossings at half filling in both the 4.9(a) and 4.9(b) remain untouched. Since the band spectra plotted so far were obtained by setting the displacement phase $\phi = 0$, in figure 4.10(a) and 4.10(b) we display the band structure for $q = 4$ and $q = 6$ respectively, with $\phi = 2\pi/5$. Analogously to what we have observed in the previous section, figure 4.10(a) shows insulating gap opening at half filling for $q = 4$, meaning that the SOC induces metal-insulator transitions at half filling as a function of the phase ϕ.

The band structure for $q = 6$ in figure 4.10(b) shows instead that the energy spectrum at half filling still remains gapless for $q = 6$. Therefore, in the case where q is even and $q \neq 4N$, the band crossings at half filling remain symmetry protected even in presence of external magnetic field.

4.3 Superconducting phase

Here we analyse the system including the proximity induced s-wave superconducting pairing term, which at tight binding, in terms of the operators $c^\dagger_{i,n,\sigma}$ and $c_{i,n,\sigma}$ reads

$$H_{SC} = \Delta \sum_{n=1}^{q} \sum_{i=1}^{N/q} c^\dagger_{n,i,\uparrow} c^\dagger_{n,i,\downarrow} + h.c + \mu \sum_{\sigma,\sigma'} \sum_{n=1}^{q} \sum_{i=1}^{N/q} c^\dagger_{n,i,\sigma} \delta_{\sigma,\sigma'} c_{n,i,\sigma'} \tag{4.6}$$

where we have included the term accounting for the on site chemical potential.
We begin by considering the bulk energy spectrum for the full Hamiltonian given by $H = H_{SOI} + H_Z + H_{SC}$, where, in terms of the operators $c^\dagger_{n,k,\sigma}$ and $c_{n,k,\sigma}$, we Fourier transform the H_{SC} as

$$H_{SC} = \Delta \sum_{n=1}^{q} \sum_{k=1}^{N/q} c^\dagger_{n,k,\uparrow} c^\dagger_{n,k,\downarrow} + h.c + \mu \sum_{\sigma,\sigma'} \sum_{n=1}^{q} \sum_{k=1}^{N/q} c^\dagger_{n,k,\sigma} \delta_{\sigma,\sigma'} c_{n,k,\sigma'}. \tag{4.7}$$

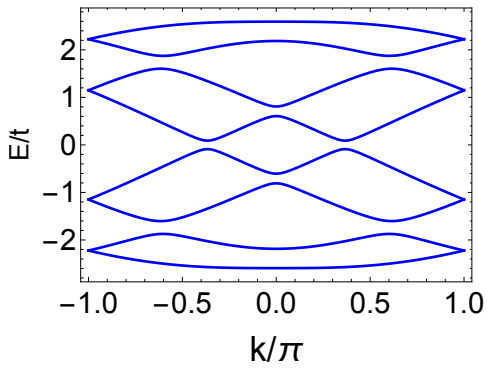

(a) Band structure $q = 4$, $B = 0.3$ and $\phi = 2\pi/5$. Here we observe insulating gap opening at half filling. The strength of the constant Rasha SOC is set at $\alpha_r/t = 0.4$ while the strength of the modulated Rashba SOC along z is set to $\alpha_m/t = 0.8$.

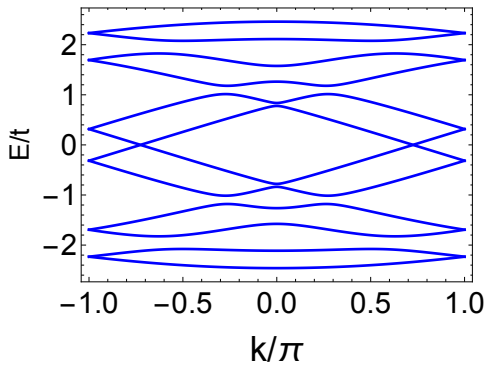

(b) Band structure $q = 6$, $B = 0.3$ and $\phi = 2\pi/5$. In here we see that, even with a non trivial value of ϕ the spectrum remains gapless at half filling. The strength of the constant Rasha SOC is set at $\alpha_r/t = 0.4$ while the strength of the modulated SOC along z is set to $\alpha_m/t = 0.8$.

Figure 4.10: Band structure for $q = 4$ and $q = 6$ atomic sites in one superlattice cell including a non trivial displacement phase.

In order to find the energy dispersion relation of the full Hamiltonian including the superconducting term, we re-write the Hamiltonian in BdG matrix form $\boldsymbol{C}_k^\dagger \boldsymbol{H}_k \boldsymbol{C}_k$, where the spinor $\boldsymbol{C}_k$ is now the $4q$ dimensional Nambu spinor defined as

$$\boldsymbol{C}_k = \left(c_{1,k,\uparrow}, c_{1,k,\downarrow}, c^\dagger_{1,-k,\uparrow}, c^\dagger_{1,-k,\downarrow}, c_{2,k,\uparrow}, ..., c^\dagger_{q,-k,\downarrow}\right)^T. \tag{4.8}$$

Our goal in this section is to verify if the additional (modulated) Rashba SOC that we have introduced in our model, plays a role in modifying the occurrence of the transition between the trivial superconducting phase of the system and the topological phase, thus leading to a different phase diagram respect to the phase diagram for a nanowire with constant Rashba SOC.
In the latter case it has in fact been established that the superconducting band gap closes for $B = \sqrt{(\mu + 2t)^2 + \Delta^2}$ leading to the topological superconducting phase at its re-opening.

From this topological criterion, we see that the phase transition occurs at $B = \Delta$ if $\mu = -2t$, which, for the wire without modulation on SOC, corresponds to setting the value of μ at the energy value of the Kramer invariant point in Γ. As seen in the previous chapter, this represents an optimal condition for the occurrence of the topological phase transition. Moreover, since the presence of the magnetic field lifts the Kramer degeneracy in $k = 0$ inducing a gap between the two bands at the Γ point, setting the chemical potential at this energy value ensures that the system is in the spinless regime created at low energy by arbitrarily small external magnetic fields. Therefore, in the analysis that follows where we include the externally modulated Rashba SOC, we will be concerned with setting the chemical potential at the energy value of the Kramer invariant point in $k = 0$.

In figure 4.11, where we plot the energy bands of the BdG Hamiltonian with magnetic field B ad superconducting pairing Δ set to zero, we show that, with the addition of the modulated Rashba SOC, the Kramer invariant point is no longer situated at $\mu = -2t$ ($\mu = -2$ in figure since the energy bands are plotted in t-units). In fact, the introduction of the externally modulated SOC changes the bandwidth, thus, since t gets renormalised to $\bar{t}$, the Kramer invariant point is now at $\mu = -2\bar{t}$, which as showed by the black line in figure 4.11(b) , is given by $\mu = -2t + \epsilon$.

Clearly, the renormalization of t resulting in a change in the energy value of the Kramer invariant point, depends on the strength of the externally modulated Rashba SOC. Therefore,

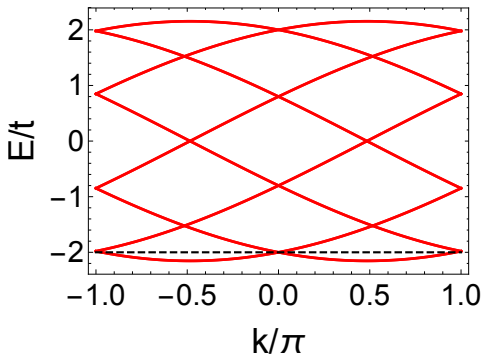

(a) Band structure $q = 4$, $B = 0.3$ and $\Delta = 0$.The Kramer invarian point at $k = 0$ is situated at $\mu/t = -2$ The strength of the constant Rasha SOC is set at $\alpha_r/t = 0.4$ while the strength of the modulated Rashba SOC along z is set to $\alpha_m/t = 0$.

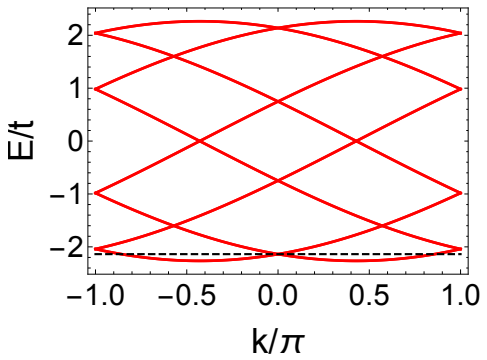

(b) Band structure $q = 4$, $B = 0.0$ and $\Delta = 0$. We observe the effect shift in the Kramer point, individuated in the graph by the dashed black line representing the chemical potential $\mu/t = -2.13371$. The strength of the constant Rasha SOC is set at $\alpha_r/t = 0.4$ while the strength of the modulated SOC along z is set to $\alpha_m/t = 0.7$.

Figure 4.11: The figures show the band structure for $q = 4$. The dashed black line individuate the Kramer invariant point when the modulated Rashba SOC is turned off (left) and on (right).

in the following analysis, we will be careful in re-setting the chemical potential μ at the energy value corresponding to the Kramer invariant point each time we modify the parameter α_m controlling the strength of the modulated SOC.

4.3.1 Effect of the Modulated Rashba SOC

Let us first consider the system where the only component of the SOC is given by the modulated Rashba coupling along the z-direction.

As a first remark, we observe that, in absence of a constant spin orbit coupling canting the spins away from the polarization induced by the magnetic field, the interband p-wave pairing is not possible. In fact, in this set up where the electron spin in the energy bands is fully polarized, the band crossings at zero energy occur between bans with the same spin and the superconducting pairing Δ is not able to form Cooper pairs between parallel spin electrons. However, when the pairing Δ is 'larger' than the Zeeman splitting, the s-wave pairing occurs, and the system is a trivial superconductor, as showed in figure 4.12.

In the conventional wire, in absence of the SOC interaction, the transition between gapped s-wave superconducting and gapless spectrum occurs when $B = \Delta$ (provided that one sets the chemical potential at $\mu = -2t$), as in fact, this criterion is independent of the strength of the constant Rashba field.

Therefore, we start by verifying that the introduction of the modulated SOC already modifies the phase transition between metallic and superconducting phases.

In figure 4.13, we plot the line separating the two phases fixing a value of the magnetic field and tuning the strength of the modulated SOC. Lines of different colours have been obtained for different values of the magnetic field (which we indicate as Δ_c in the legend). The 4.13(a) and the 4.13(b) are plotted for different superlattice periods ($q = 4$ and $q = 5$ respectively). The dashed lines separate the $\Delta < B$ (left side of the dashed lines) and the $\Delta > B$ (right side) sections and they correspond to the closing of the superconducting gap when $\alpha_m = 0$. The coloured lines in both the figures in 4.13 show that the occurrence of the phase transition is modified when a local SOC is introduced, and the modified critical line is a monotonic function

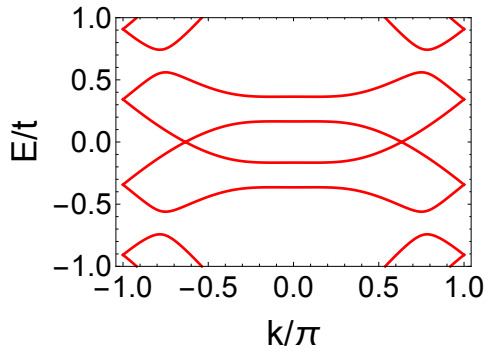

(a) Band structure $q = 4$, $B = 0.3$ and $\Delta = 0.1$, the value of the chemical potential is $\mu/t = -2.11896$. The strength of the constant Rashba SOC α_r/t is set to zero while $\alpha_m/t = 0.7$. We observe here the gapless spectrum for $B > \Delta$.

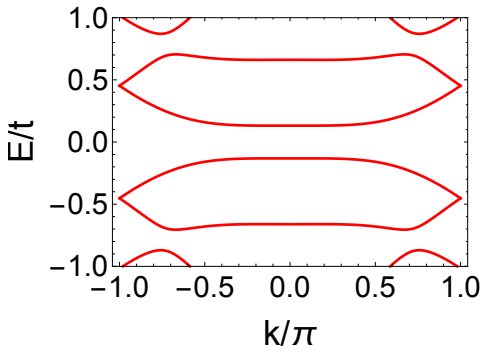

(b) Band structure $q = 4$, $B = 0.3$ and $\Delta = 0.1$, the value of the chemical potential is $\mu/t = -2.11896$. The strength of the constant Rashba SOC α_r/t is set to zero while $\alpha_m/t = 0.7$. In here we have the gapped spctrum of the s-wave superconducting phase occurring for $B < \Delta$.

Figure 4.12: The figures show the band structure for $q = 4$. The dashed black line individuate the Kramer invariant point when the modulated Rashba SOC is turned off (left) and on (right).

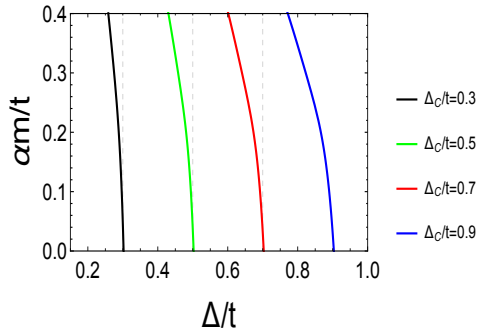

(a)

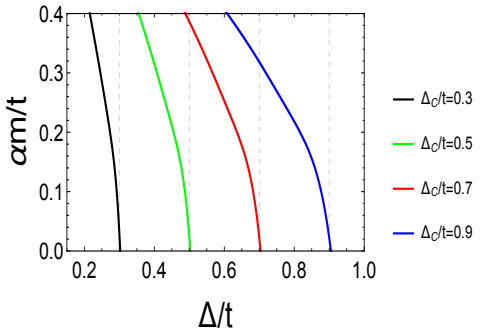

(b)

Figure 4.13: Figure shows how the closing of the superconducting gap separating the s-wave and gapless phase is modified by the modulated Rashba SOC. The dashed lines indicate the value $\Delta = B$, (or Δ_c as in the graph labels) at which the gap closes when the modulated SOC is turned off. Therefore each coloured line is the critical line obtained varying α_m and Δ having fixed a different value for the magnetic field (indicated in the legend as Δ_c). For each value of α_m, the chemical potential μ is set at the Kramer point energy value in Γ.

of α_m.
These diagrams therefore show that the occurrence of the phase transition depends on the parameter α_m, which controls the strength of the modulated SOC. This already denotes an outstanding difference compared to the conventional wire, where no dependency on the strength of the Rashba SOC was found.
Furthermore, observing the diagrams, we can conclude that the introduction of a the local SOC leads to an enhancement of the superconducting phase as the lines separating the two phases are shifted more and more to the left as α_m increases, thus allowing the pairing Δ to open a gap also when $\Delta < B$. The enhancing of the superconducting phase becomes more evident for higher magnetic fields.

The same feature is observed in 4.14 where the phase diagram is plotted in the plane B/Δ. In 4.14, the x-axis represents the line $B = \Delta$, so the whole portion of plane displayed in the diagram represents the gapless phase of the system in the case of the conventional wire. However, as one introduces the modulated SOC, we see that the portion of the diagram delimited by the

coloured lines is now in the superconducting phase. Moreover, in agreement with the previous diagrams, the enhancing of the superconducting phase is proportional to α_m.

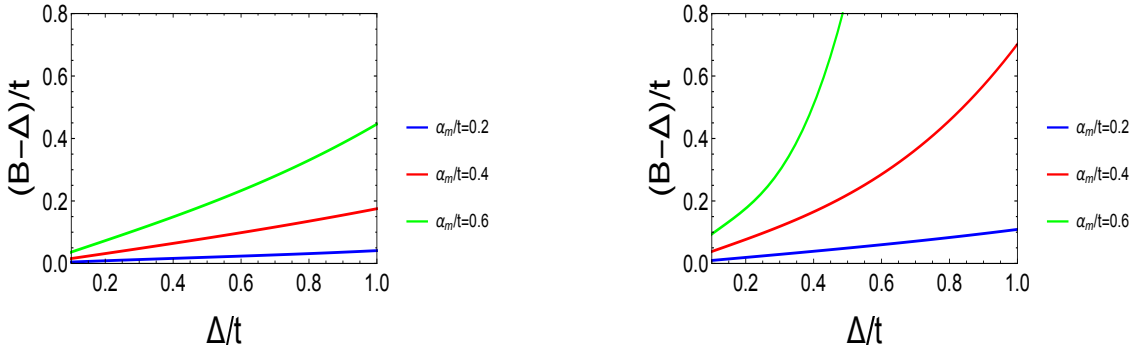

Figure 4.14: In figure the enhancing on the s-wave superconducting phase due to α_m is shown for $q = 4$ (left) and $q = 5$ (right). The x-axis represents the line $B = \Delta$ and the portion of plane displayed in the figure is the plane $B > \Delta$, where the system is in its gapless phase when $\alpha_m = 0$. For $\alpha_m \neq 0$ the system is in the s-wave phase in the part of the plane delimited by the coloured lines, for each value of α_m.

We therefore conclude that the local SOC promotes superconductivity over the gapless phase, allowing for the superconducting gap to remain open even for values of the pairing Δ smaller than the magnetic field.

4.3.2 Topological Phase Transition analysed in Bulk

Now we consider the full system in presence of constant Rashba splitting. Here, the s-wave gap in the bulk band spectrum closes in a specific point in parameter space, then it opens again and the system is found in the topological phase.
We hereby look at the changes in the phase diagram due to the introduction of the modulation on the Rashba field.

We proceed as in the previous section and in figure 4.15 we display the phase diagram in the plane α_m/Δ, obtained by fixing a value for the magnetic field and tuning the strength of the local SOC. The different coloured lines have been obtained for different values of the strength of the constant SOC α_r. Analogously to what we observed in the case $\alpha_r = 0$, all the curves in 4.15 indicate an enhancing of the trivial superconducting phase in the diagram.
Moreover, we can appreciate another interesting feature: when in the system both the Rashba spin orbit coupling components are present (the constant one in the y-direction, controlled by the tuning parameter α_r and the modulated SOC along z direction with corresponding strength α_m), their combined effect is such that the enhancing of the trivial superconducting phase gets even more amplified as the value of is α_r increased.

The same features are confirmed by looking at the phase diagrams in the B/Δ plane of figure 4.16. Here, we have chosen a specific value of the strength of the modulated SOC and the diagrams show an enlarging of the trivial phase proportional to the strength of the magnetic field and of the constant Rashba SOC strength α_r.

We consider appropriate to pause for a moment and make two comments on the study conducted so far.
As a first remark, we wish to remind that previous analysis, was made choosing a specific value of the chemical potential, which coincides with the energy value at the Kramer degeneracy in Γ (in presence of time reversal symmetry).
In fact, at the beginning of this section, we have recalled that the condition $\mu = -2t$ in the conventional wire represents the optimal condition for driving the system in the topological phase.

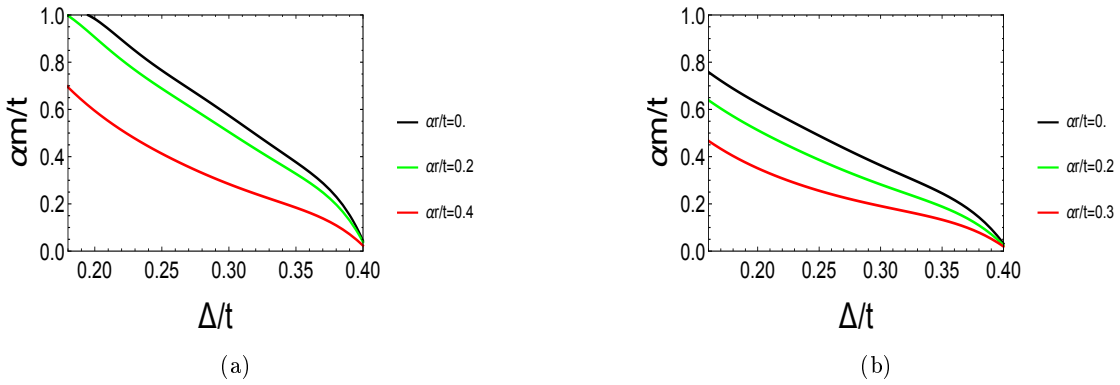

(a) (b)

Figure 4.15: In figure, $B/t = 0.4$. The lines obtained for various α_r mark the phase transition between topological phase for the cases $\alpha_r \neq 0$, or gapless phase (black line, $\alpha_r = 0$) and trivial phase (right side of the lines). On the left $q = 4$, on the right, q=5. In the diagrams, the vertical line at $\Delta = B = 0.4$ separates the two phases in the case of conventional wire. The trivial superconducting phase (right side of the curves) is therefore enhanced by the introduction of the modulated SOC.

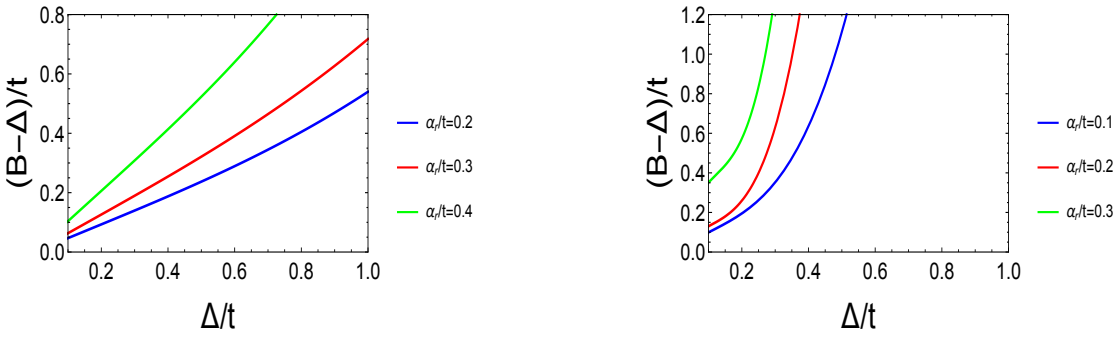

(a) (b)

Figure 4.16: In figure, the x-axis represents the $B = \Delta$ line, at which the phase transition would occur if $\alpha_m = 0$. In here, α_m/t is set to 0.6, and the lines plotted for different α_r show how the occurrence of the phase transition deviates from the x-axis. The coloured lines for different α_r mark the border between trivial superconducting phase (lower part of the diagram) and topological phase (upper part), showing the enhancement of the s-wave phase. On the left, $q = 4$, on the right $q = 5$.

We have furthermore argued that with the addition of the modulated SOC there is a renormalization on t, that leads to a shift of the Kramer invariant point at $\bar{t} = t \pm \epsilon$, where $\bar{t}$ changes in function of the modulated SOC, thus, we set $\mu = -2\bar{t}$ during the whole previous analysis. In figure 4.17 we show indeed that, setting the chemical potential at $\mu = -2\bar{t}$ represents the optimal condition for the occurrence of the phase transition, even in presence of the externally modulated SOC. In fact, as we can appreciate in 4.17 the critical line for the phase transition obtained when μ is set at the energy value of the Kramer invariant point, is the minimum of the set of curves obtained when the chemical potential is set to different values within the effectively spinless range created by the external magnetic field at low energy.

As a second remark, we would like to underline that, in the spirit of running a tight binding analysis in the low energy regime, we decided to restrict ourselves to study the system when the chemical potential is in the 'effectively spinless' regime induced between the two lowest energy bands, which means that this analysis has been restricted to filling fractions $\nu < 1/2q$.

From the phase diagrams obtained in both cases $\alpha_r = 0$ and $\alpha_r \neq 0$ we learned that the presence of the modulated SOC indeed interferes with the occurrence of the topological phase transition as it seems to modify the condition in parameter space under which the bulk energy spectrum becomes gapless. The results showed by the diagrams are quite impressive. First of

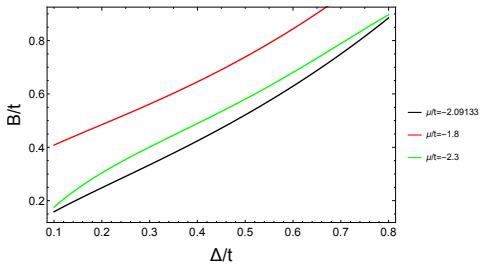

(a) Critical line for the occurrence of the topological phase transition in the plane B/Δ obtained for a superlattice periodicity $q = 4$. The black line represents the phase transition line when μ is set at the Kramer invariant point. The strength of the constant SOC is $\alpha_r/t = 0.2$ and the strength of the modulated SOC $\alpha_m/t = 0.6$".

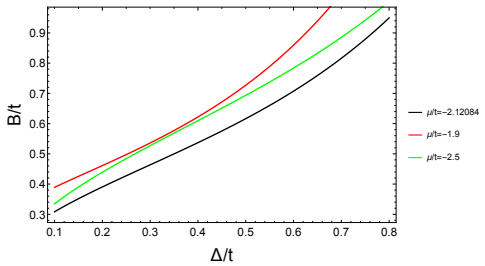

(b) Critical line for the occurrence of the topological phase transition in the plane B/Δ obtained for a superlattice periodicity $q = 5$. The black line represents the phase transition line when μ is set at the Kramer invariant point. The strength of the constant SOC is $\alpha_r/t = 0.2$ and the strength of the modulated SOC $\alpha_m/t = 0.6$". .

Figure 4.17: The sets of curves obtained for two different superlattice periods (one even and one odd), show the critical line which separates the trivial and the topological superconducting phases. We observe that the critical line obtained when $\mu = -2\bar{t}$ is the minimum of the set of curves plotted for both superlattice periods.

all because they are suggesting that the topology of the ground state manifold (which is a global property of the system) is affected by the locally varying SOC, and secondly, because both the 4.15 and 4.16 show that the occurrence of the phase transition is modified as one changes the strengths of the Rashba SOC α_r and α_m, suggesting that the latter should enter somehow the criterion for the bulk gap closing. This is in contrast to the result for the conventional wire, as the criterion for the topological phase transition derived in chapter two is not influenced by the strength of the constant Rashba field α_r.

Therefore, in order to attempt a derivation for the criterion of the phase transition in the system with additional modulated SOC , we start by looking at the Hamiltonian for the normal phase in real space $H = H_{SOC} + H_Z$:

$$\begin{aligned} H_{SOC} &= \sum_{\sigma,\sigma'} \int dx \Psi^\dagger_\sigma(x) \left[-\frac{\partial_x^2}{2m} + \frac{i\alpha_m}{2}\{k(x), \partial_x\}\tau^z_{\sigma,\sigma'} + \alpha_r \tau^y_{\sigma,\sigma'}\partial_x \right] \Psi_{\sigma'}(x) \\ H_z &= \sum_{\sigma,\sigma'} \int dx \Psi^\dagger_\sigma(x)[B\tau^x_{\sigma,\sigma'}]\Psi_{\sigma'}(x). \end{aligned} \tag{4.9}$$

Since we have observed that the phase diagram is modified by the introduction of the modulation on the SOC, in the following, we consider that the main contribution on the modified band structure (and consequently on the new phase diagram) comes from the modulated SOC. We thus write the normal phase Hamiltonian as $H = H_0 + H_1$. The unperturbed Hamiltonian $H_0 = H_{kin} + H_{\alpha_m}$, is given by the kinetic energy term and the modulated Rashba term, whereas the Hamiltonian H_1 which we will consider as a small perturbation is given by $H_1 = H_{\alpha_r} + H_z$.

We therefore write H_0 as

$$\begin{aligned} H_0 &= \sum_{\sigma,\sigma'} \int dx \Psi^\dagger_\sigma(x) \left[-\frac{\partial_x^2}{2m} + \frac{i\alpha_m}{2} \{k(x), \partial_x\} \tau^z_{\sigma,\sigma'} \right] \Psi_{\sigma'}(x) \\ &= \sum_{\sigma,\sigma'} \int dx \Psi^\dagger_\sigma(x) \left[\frac{1}{2m} \left(-i\partial_x - m\alpha_m \cos\left(\frac{2\pi}{\lambda} x\right) \tau^z_{\sigma,\sigma'} \right)^2 - \frac{m\alpha_m^2}{2} \cos^2\left(\frac{2\pi}{\lambda} x\right) \right] \Psi_{\sigma'}(x) \\ &= \sum_{\sigma,\sigma'} \int dx \Psi^\dagger_\sigma(x) \hat{H}_0 \Psi_{\sigma'}(x). \end{aligned} \tag{4.10}$$

Where we have used the fact that every Hamiltonian including a linear SOC term can be put in this quadratic form by simply 'completing the square'. Note that the $\hat{H}_0$ in the preceding can be written as

$$\hat{H}_0 = \frac{\Pi^2}{2m} - V(x)$$

where

$$\Pi = \left(-i\partial_x - m\alpha_m \cos\left(\frac{2\pi}{\lambda} x\right) \tau^z_{\sigma,\sigma'} \right)$$

is obtained via minimal substitution, and the potential $V(x)$ just reads

$$V(x) = -\frac{m\alpha_m^2}{2} \cos^2\left(\frac{2\pi}{\lambda} x\right).$$

Having H_0 in this form, we thus recognize that, we can apply a Gauge transformation in order to bring H_0 in the form of a free particle Hamiltonian.
This is a procedure that can always be done in presence of a linear SOC term [56, 57, 58], and it is justified by the fact that the the SOC vector can be re-interpreted as a Gauge vector in the same fashion as the vector potential A that appears in the minimal substitution of the momentum in QED [59].

In our specific case, the unitary transformation needed to bring H_0 in the desired form is given by

$$\hat{U} = exp\left(im\alpha_m \int^x dx' \cos\left(\frac{2\pi}{\lambda} x'\right) \tau^z \right) \tag{4.11}$$

to the field $\Psi(x)$ such that $\Psi'(x) = \hat{U}\Psi(x)$ and $\hat{H}_0' = \hat{U}^\dagger \hat{H}_0 \hat{U}$.
Computing the derivatives and then commuting $\hat{H}_0$ and $\hat{U}$, we get

$$\hat{H}_0' = -\frac{\partial_x^2}{2m} - \frac{m\alpha_m^2}{2} \cos^2\left(\frac{2\pi}{\lambda} x\right). \tag{4.12}$$

Having obtained a more easily solvable form for H_0, we want now to include the perturbation H_1 in our analysis. We apply the same unitary transformation to $\hat{H}_Z$ and $\hat{H}_{\alpha_r}$. In here, we have to work with matrix multiplication since the unitary transformation contains the Pauli matrix τ^z whereas the Zeeman term is along τ^x and the constant Rashba SOC along τ^y.
For the Zeeman term we thus have

$$\hat{H}_Z' = \hat{U}^\dagger B \tau^x \hat{U} = \begin{pmatrix} -A & 0 \\ 0 & A \end{pmatrix} \begin{pmatrix} 0 & 1 \\ 1 & 0 \end{pmatrix} \begin{pmatrix} A & 0 \\ 0 & -A \end{pmatrix} \tag{4.13}$$

where we have set for brevity $A = exp\left(im\alpha_m \int^x dx' \cos\left(Qx'\right)\right)$, with $Q = \left(\frac{2\pi}{\lambda}\right)$. Computing the matrix multiplication and re-writing A in its extended form one finds

$$\hat{H}_Z^{'} = \begin{pmatrix} 0 & exp\left(-2im\alpha_m \int^x dx^{'} \cos\left(Qx^{'}\right)\tau^z\right) \\ exp\left(2im\alpha_m \int^x dx^{'} \cos\left(Qx^{'}\right)\tau^z\right) & 0 \end{pmatrix} \\ = \cos\left(\frac{2m\alpha_m}{Q}\sin\left(Qx\right)\right)\tau^x + \sin\left(\frac{2m\alpha_m}{Q}\sin\left(Qx\right)\right)\tau^y \tag{4.14}$$

where in the second equality we have used the Euler formulas and we have computed the integral $\int^x \cos Qx^{'}dx^{'}$. Similar procedure can be applied to the constant Rashba term yielding

$$\hat{H}_{SOC}^{'} = \hat{H}_0^{'} + i\alpha_r \cos\left(\frac{2m\alpha_m}{Q}\sin\left(Qx\right)\right)\tau^y + i\alpha_r \sin\left(\frac{2m\alpha_m}{Q}\sin Qx\right)\tau^x \tag{4.15}$$

Now, if we assume that the term $\hat{H}_0^{'}$ is the dominant term in determining the band structure, we can treat the constant Rashba SOC with strength α_r and the Zeeman term as perturbation and compute the first order in perturbation theory.
When one computes $\langle H_Z^{'}\rangle$, the term with the $\sin\left(\frac{2m\alpha_m}{Q}\sin\left(Qx\right)\right)$ vanishes since it is an odd function of x and the integral over the whole space gives zero, whereas the term with $\cos\left(\frac{2m\alpha_m}{Q}\sin\left(Qx\right)\right)$ integrated gives $\frac{2\pi}{Q}J_0\left(|\frac{2m\alpha_m}{Q}|\right)$ with J_0 first Bessel function. Therefore, at first order correction, the Zeeman term is renormalized by a factor proportional to the J_0 as a function of the strength of the modulated Rashba α_m. The same happens for the strength of the constant SOC term α_r which also gets renormalised as $\bar{\alpha}_r(\alpha_m)\ \alpha_m$.
Combining the preceding, we have that the effective Hamiltonian for the normal phase reads

$$\hat{H}^{'} = -\frac{\partial_x^2}{2m} - \frac{m\alpha_m^2}{2}\cos^2 Qx + i\alpha_r\tau^y J_0\left(\frac{2m\alpha_m}{Q}\right) + B\tau^x J_0\left(\frac{2m\alpha_m}{Q}\right) \tag{4.16}$$

where J_0 is the first Bessel function, which is a decreasing function, smaller than one, in the interval $[0, 1]$.
We can therefore conclude that, at low energy and for very small values of α_r and B, both the Zeeman energy and the constant Rashba field experienced from a fermion moving in the nanowire where a locally varying Rashba SOC is added, are decreased by effect of the latter. In particular, they decrease following the J_0, which is plotted in figure 4.18 and shows the same trend as the line marking the phase transition showed in the previous section for α_m small.
To be more rigorous, we must underline that the Zeeman energy that we have indicated with the label B so far, is indeed given by $E_z(=B) = \frac{1}{2}g\mu_B h$ where mu_B is the Bohr magneton, h is the value of the external magnetic field applied to the system, and g is the Landé g factor. The latter, is the one that gets indeed renormalized by the presence of the modulation on the SOC. As a consequence of the renormalization of the g factor, the Zeeman splitting effectively acting on the particles is lower, thus a lower superconducting pairing Δ is necessary in order to create the transition to the trivial superconducting phase. In other words, the s-wave interband pairing in the 2.49 occurs for a smaller Δ.
Thus, the criterion for the gap closing $B > \sqrt{(2t+\mu)^2 + \Delta^2}$ appears modified as $\bar{B}(\alpha_m) > \sqrt{(2t+\mu)^2 + \Delta^2}$ where $\bar{B}(\alpha_m) < B$.

4.3.3 Topological phase transition analysed with the open chain

Finally, we analyse the system at tight binding with open boundary conditions, in order to verify the validity of the criterion found imposing periodic boundary condition. According to bulk-edge correspondence, we in fact expect to find zero energy eigenvalues localised at the end of the nano-wire when the system is predicted to be in the topological phase. Figure 4.19 shows the eigenvalues for the open chain with superlattice period $q = 4$. As indicated in the caption, the plot of the gapped spectrum on the left hand side is obtained for $\Delta < B$,(i.e where we expect

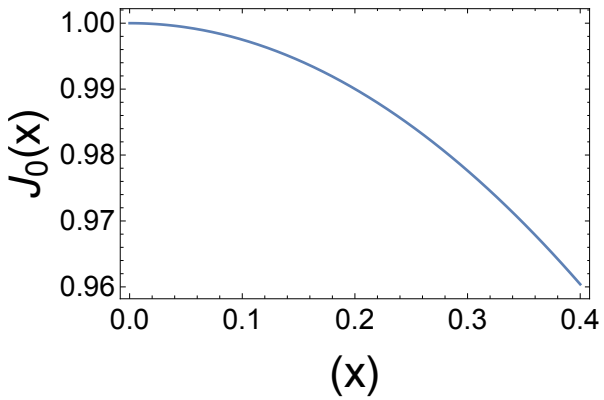

Figure 4.18: Plot of the first Bessel $J_0(x)$ function in the interval $x \in (0, 0.4)$

to find Majorana modes in the case of the conventional wire where $\alpha_m = 0$) showing us once more the effect of the modulated Rashba SOC, which diminishes the value of the average magnetic field perceived by the particle, allowing for s-wave pairing at higher B. As a consequence of that, the gap closing does not happen at $\Delta = B$ but at $\Delta = \bar{B}(\alpha_m)$ with $\bar{B}(\alpha_m) < B$.
The left side of the figure shows indeed that, for values of $\Delta < \bar{B}(\alpha_m)$ the system is still gapped but there are two zero energy modes, ensuring us that indeed the phase transition occurs and, after the gap closing, the system is in the topological phase.

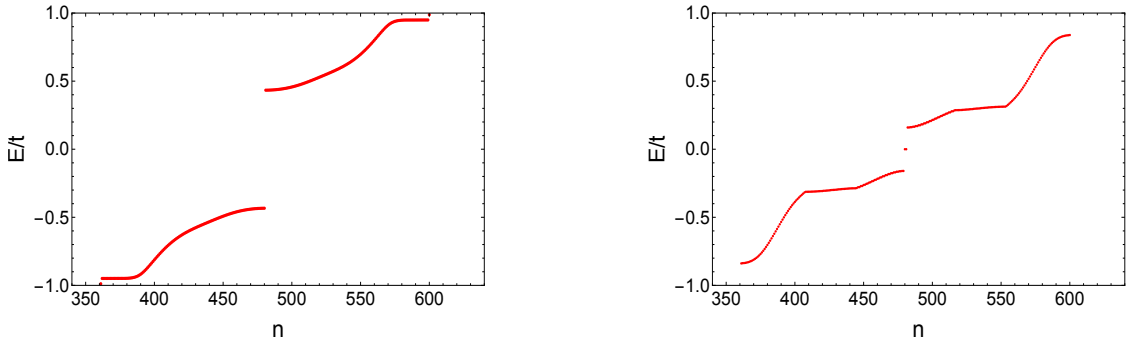

(a) (b)

Figure 4.19: The figure is obtained diagonalizing an Hamiltonian of 200 sites with superlattice unit cell containing $q = 4$ atomic sites. On the left, we see the s-wave gapped spectrum obtained for $\Delta/t = 0.3$ and $B/t = 0.4$: we have trivial superconductivity for $B > \Delta$, due to the modulated SOC. On the right we see instead the zero energy modes appearing in the eigenvalues spectrum once the gap has closed bringing the system in the topological phase. On the left site we have set $\Delta/t = 0.3$ and $B/t = 0.9$. In both the plots, $\alpha_r/t = 0.4$, $\alpha_m/t = 0.6$ and the chemical potential is at the Kramer invariant point ($\mu/t = -2.59389$ for this set of parameters.)

Chapter 5

Geometry Induced Topological Phase Transitions

In the third chapter of this thesis, we introduced the effective $k \cdot p$ Hamiltonian for a planary curved semiconducting wire. We have seen that the effect of the curved geometry can be incorporated in a locally varying spin orbit coupling term in the one dimensional effective Hamiltonian describing the motion of the electron along the curve. In this chapter we consider the semiconductor-superconductor heterostructure hosting Majorana modes, with the semiconducting nanowire being the serpentine-shaped wire discussed previously. We start by analysing the bulk band structure of the semiconducting wire alone, in order to enlighten the influence of the curvature induced locally-varying Rashba SOC, and we proceed by first introducing a Zeeman splitting in the bulk band structure and then adding the proximity induced s-wave superconductivity, in order to study the full system designed to host Majorana modes in its topological phase.

5.1 Normal Phase Bulk Bands

The effective tight binding Hamiltonian in momentum space for the serpentine-shaped nanowire introduced in chapter three reads

$$\begin{aligned} H_{SOC} = \sum_{\sigma,\sigma'}\sum_{n=1}^{q-1}\sum_{k=1}^{N/q} & c^{\dagger}_{n,k,\sigma}\left[-t\delta_{\sigma,\sigma'} + \frac{i\alpha_r}{2}\tau^{y}_{\sigma,\sigma'}\left(\frac{\cos\left(\theta(x_n)\right)+\cos\left(\theta(x_{n+1})\right)}{2}\right)\right]c_{n+1,k,\sigma'} \\ & + c^{\dagger}_{n,k,\sigma}\left[+\frac{i\alpha_r}{2}\tau^{x}_{\sigma,\sigma'}\left(\frac{\sin\left(\theta(x_n)\right)+\sin\left(\theta(x_{n+1})\right)}{2}\right)\right]c_{n+1,k,\sigma'} \\ & + c^{\dagger}_{q,k,\sigma}\left[-t\delta_{\sigma,\sigma'} + \frac{i\alpha_r}{2}\tau^{y}_{\sigma,\sigma'}\left(\frac{\cos\left(\theta(x_q)\right)+\cos\left(\theta(x_1)\right)}{2}\right)\right]e^{ik}c_{1,k+1,\sigma'} \\ & + c^{\dagger}_{q,k,\sigma}\left[\frac{i\alpha_r}{2}\tau^{x}_{\sigma,\sigma'}\left(\frac{\sin\left(\theta(x_q)\right)+\sin\left(\theta(x_1)\right)}{2}\right)\right]e^{ik}c_{1,k+1,\sigma'} \end{aligned} \quad . \tag{5.1}$$

where$\theta(x_n) = -\frac{A}{\lambda}\cos\left[2\pi\left(\frac{n}{q}+\frac{\phi}{2\pi}\right)\right]$, $\theta(x_q) = -\frac{A}{\lambda}\cos\left[2\pi\left(1+\frac{\phi}{2\pi}\right)\right]$ and $\theta(x_1) = -\frac{A}{\lambda}\cos\left[2\pi\left(\frac{1}{q}+\frac{\phi}{2\pi}\right)\right]$ and q indicates the number of atomic sites included in the superlattice unit cell and ϕ is the displacement phase.
In order to be able to find the energy eigenvalues, we write the preceding in matrix form as $\boldsymbol{C}^{\dagger}_{k}H_k\boldsymbol{C}_k$, where we recall

$$\boldsymbol{C}_k = \left(c_{n_1,k,\uparrow}, c_{n_1,k,\downarrow}, c_{n_2,k,\uparrow}, ..., c_{n_q,k,\downarrow}\right)^T$$

defined in chapter three. In the following, we study the bulk band structure for different superlattice periodicities obtained diagonalizing the matrix H_k.

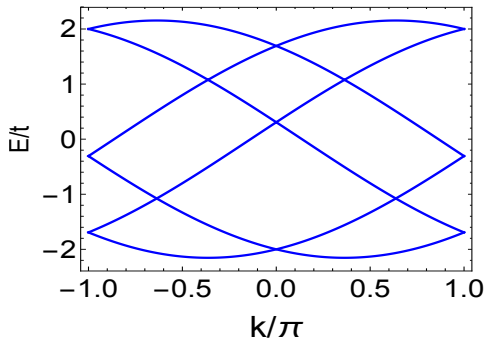

(a) Band Structure $q = 3$. In here, A/λ is set to zero. In this case, the only component of the SOC active in the system is a constant component along the y direction (due to the particular form of the SOC in 5.1),leading to the typical momentum-dependent spin splitting of the energy bands. The strength of the Rasha SOC is set at $\alpha_r/t = 0.2$

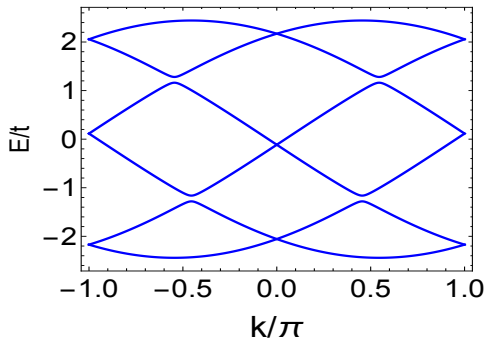

(b) Band structure for $q = 3$. Here $A/\lambda = 0.8$, thus the SOC term is locally varying in the x/y plane. We observe insulating gap opening at unpinned point the first mBZ for all integer filling fractions $\nu = 1/3$, $\nu = 2/3$. The strength of the Rasha SOC is set at $\alpha_r/t = 0.2$.

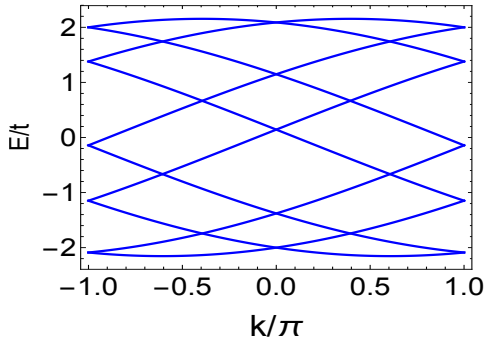

(c) Band Structure $q = 5$. In here, A/λ is set to zero. In this case, the only component of the SOC active in the system is a constant component along the y direction (due to the particular form of the SOC in 5.1), leading to the typical momentum-dependent spin splitting of the energy bands. The strength of the Rasha SOC is set at $\alpha_r/t = 0.2$

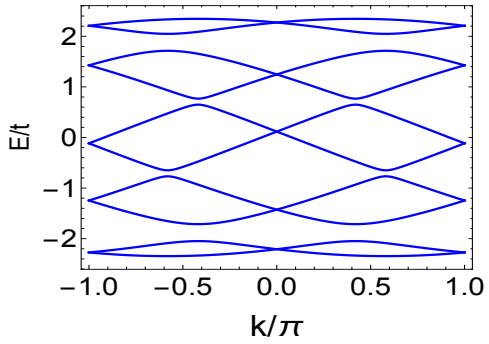

(d) Band structure for $q = 5$. Here $A/\lambda = 0.8$, thus the SOC term is locally varying in the x/y plane. We observe insulating gap opening at unpinned point the first mBZ for all integer filling fractions $\nu = 1/5$, $\nu = 2/5$,$\nu = 3/5$ and $\nu = 4/5$. The strength of the Rashba SOC is set at $\alpha_r/t = 0.2$.

Figure 5.1: Energy bands for $q = 3$ and $q = 5$ atomic sites in a superlattice unit cell. Both the superlattice periodicity show the same behaviour when the curvature induced locally varying spin orbit coupling is acting on the system.

We consider at first a superlattice unit cell with odd periodicity. In Figure 5.1 we plot the band structure for $q = 3$ and $q = 4$ atomic sites in the unit cell. In 5.1(a) and 5.1(c) we have set A/λ to zero, which implies that all the $\theta(x_n)$ in 5.1 are zero. When the curvature is zero the local canting of the spin is no longer present, and the motion of the electron in the semiconductor in presence of SOC is described by the Pauli-Schrödinger Hamiltonian in the one dimensional flat space. In the tight biding Hamiltonian 5.1 one can verify that when all the $\theta(x_n)$ are zero, only the constant components along y of the SOC survive. Therefore, the plots in 5.1(a) and 5.1(c) show the band structure for a conventional straight wire where the momentum-dependent band splitting is given by the uniform Rashba SOC applied, and it displays Kramer degeneracy at the Kramer invariant points: $k = 0$ and $k = \pm\pi$. Note that the band folding in the mBZ is the result of an 'artificial' superlattice structure in real space: in fact, in this case, the invariance for translation is not broken as no local term is introduced. We nevertheless chose to show the band folding in the first mBZ in order to compare it with the band structure where the effects of the curvature are present.

The band structure for non trivial values of A/λ is plotted in figures 5.1(b) and 5.1(d). In here, we appreciate the effect of the locally varying SOC, which induces metal-insulator transitions at all integers filling fractions $\nu = n/q$ (with n integer), at unpinned points in the first mBZ, thus showing the same features we have already encountered analysing the previous model with externally modulated SOC.

In figure 5.2, we plot the band structure for an even periodicity of the superlattice, in particular for $q = 4$ and $q = 6$ atomic sites in the unit cell.
As for the above, figures 5.2(a) and 5.2(c) show the band structure of a system with only constant SOC along the y-direction, since A/λ is set to zero. When we allow for non trivial values of A/λ we obtain the band structure displayed in 5.2(b) and 5.2(d). In the former, the band structure is plotted for $q = 4$ atomic sites in the unit superlattice cell and we see no insulating gap opening occurring in the bulk spectrum. The latter shows the band structure when $q = 6$ atomic sites are placed in the unit cell, and we observe metal- insulator transitions only at filling fractions $\nu = 2/6$ and $\nu = 4/6$. However, the previous band structures are plotted when the displacement phase ϕ is set to zero. Therefore, in order to verify the possible occurrence of metal-insulator phase transitions if a phase is introduced between the periodicity of the superlattice array of unit cells and the periodic canting of spins induced by the SOC, we plot the band structure for $q = 4$ and $q = 6$ for non trivial values of ϕ.
In figure 5.3, we show the band structure for $q = 4$ when the displacement phase $\phi = 2\pi/5$, and we observe insulating gap opening at half filling fractions. Since the bulk band structure appears gapless at half filling when $\phi = 0$ and it acquires a gap when including a non trivial value of the phase ϕ, we analyse the energy spectrum sweeping the parameter ϕ for a whole period, in order to individuate the possible topological phase transitions between insulating phases. Figure 5.4 displays the band structure obtained diagonalizing the Hamiltonian for an open chain, showing the appearance of zero energy end modes after a first gap closing of the bulk band spectrum, signalling the presence of a phase transition in the system between a trivial and a topological insulating phase.

Analysing the symmetries of the system, for any value of ϕ we have Time Reversal symmetry $\boldsymbol{T}H_k\boldsymbol{T}^{-1} = H_{-k}$, where $\boldsymbol{T}^2 = -1$ for a system of spin 1/2 particles; a unitary Chiral symmetry (sub-lattice symmetry), which reads $\boldsymbol{C}H_k\boldsymbol{C}^{-1} = -H_k$ and a Particle-Hole symmetry $\boldsymbol{P}H_k\boldsymbol{P}^{-1} = -H_{-k}$ where $\boldsymbol{P}^2 = -1$. Therefore, the symmetry class of the system is the chiral symplectic class CII in the the Altland-Zirnbauer periodic table, which yields a Z topological invariant.

Figure 5.5 shows the band structure for $q = 6$ atomic sites in the unit cell where $\phi = 2\pi/5$. As opposed to what happens for the case $q = 4$, in here, no metal-insulator transition occurs at half filling including a displacement phase. Meaning that the band crossings at $\nu = 1/2$ are protected by an inner symmetry. The same holds for the energy level crossings at filling fractions $\nu = 1/q$ and $\nu = (q-1)/q$ with q even.

With the analysis above, we have showed that, in the normal phase, the two models we are considering, show the same features, and both show consistency with the more general and exhaustive study presented in [31].

5.1.1 Bulk Band analysis with the additional Magnetic Field

We now add a magnetic field to the system, orthogonal to the plane of the spin orbit interaction. The magnetic field breaks Time Reversal symmetry, changing the symmetry class of the Hamiltonian, thus we are going to analyse the band structure of the system with the additional magnetic field, verifying the influence of the curvature-induced local canting of the spins on the

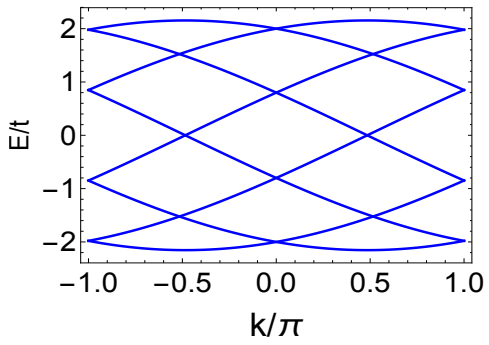

(a) Band Structure $q = 4$. In here, A/λ is set to zero. In this case, the only component of the SOC active in the system is a constant component along the y direction, leading to the typical momentum-dependent spin splitting of the energy bands. The strength of the Rasha SOC is set at $\alpha_r/t = 0.4$

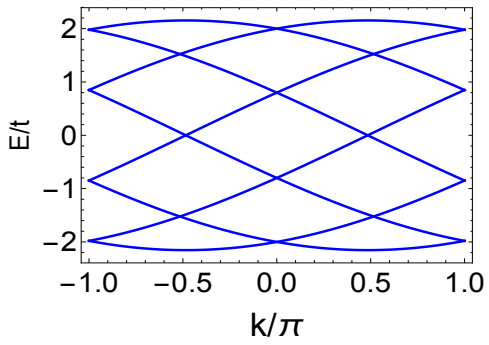

(b) Band structure for $q = 4$. Here $A/\lambda = 0.8$, thus the SOC term is locally varying in the x/y plane. We observe no insulating gap opening in the first mBZ. The strength of the Rasha SOC is set at $\alpha_r/t = 0.4$.

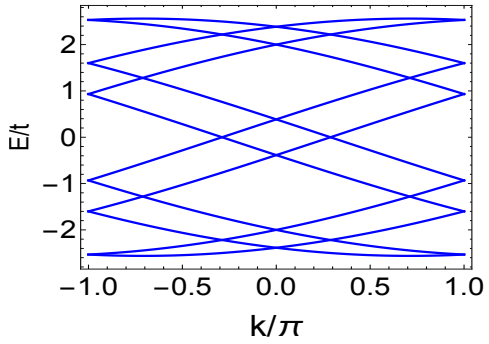

(c) Band Structure $q = 6$. In here, A/λ is set to zero. In this case, the only component of the SOC active in the system is a constant component along the y direction (due to the particular form of the SOC in 5.1), leading to the typical momentum-dependent spin splitting of the energy bands.The strength of the Rasha SOC is set at $\alpha_r/t = 0.3$

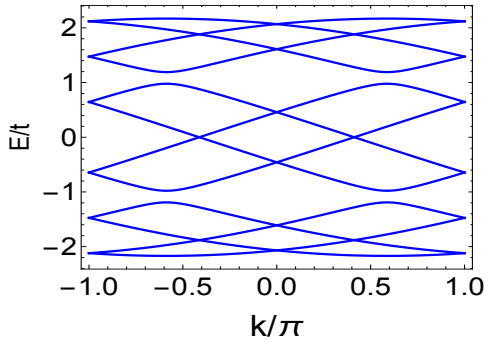

(d) Band structure for $q = 6$. Here $A/\lambda = 0.8$, thus the SOC term is locally varying in the x/y plane. We observe insulating gap opening at unpinned point the first mBZ for the filling fractions $\nu = 1/3$ and $\nu = 2/3$, but no insulating gap opens for the filling fractions $\nu = 1/6$, $\nu = 1/2$ and $\nu = 5/6$. The strength of the Rasha SOC is set at $\alpha_r/t = 0.3$.

Figure 5.2: Energy bands for $q = 4$ and $q = 6$ atomic sites in a superlattice unit cell. When the locally varying SOC is present in the system, we observe no insulating gap opening in the first mBZ at filling fractions $\nu = n/q$ where n and q co-primes and q even.

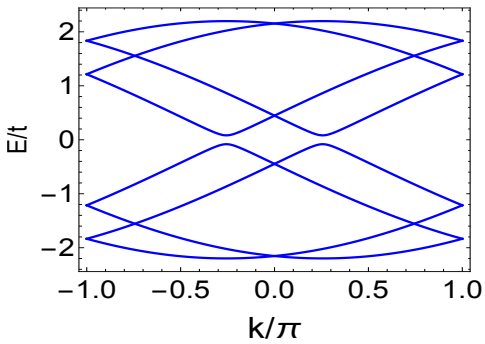

Figure 5.3: Band structure $q = 4$. The displacement phase is $\phi = 2\pi/5$, and the energy spectrum show an insulating gap opening at half filling. The strength of Rashba SOC is $\alpha_r/t = 0.4$ and $A7\lambda = 0.8$.

topology of the new system.

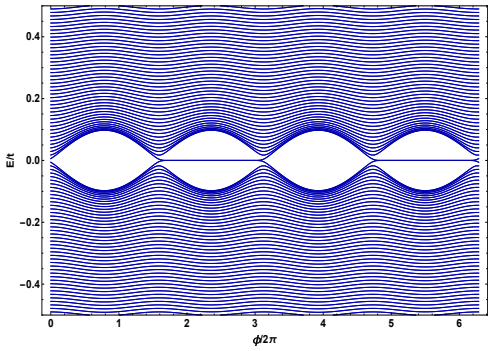

Figure 5.4: Band structure for the system with $q = 4$ atomic sites in a unit cell, obtained by diagonalizing an open chain containing $N = 600$ atoms. The strength of the SOC is $\alpha_r/t = 0.3$ and $A/\lambda = 0.4$.

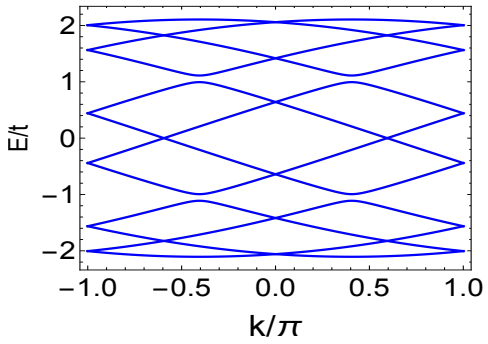

Figure 5.5: Band structure for $q = 6$.The displacement phase is $\phi = 2\pi/5$, the energy spectrum shows, as in the case where $\phi = 0$ insulating gap opening only at filling fractions $\nu = 1/3$ and $\nu = 2/3$. The strength of the SOC is $\alpha_r/t = 0.3$ and $A/\lambda = 0.8$.

The Hamiltonian is given by $H = H_{SOC} + H_Z$, where,

$$H_Z = \sum_{\sigma,\sigma'} \sum_{n=1}^{q} \sum_{i=1}^{N/q} c^{\dagger}_{n,i,\sigma} B\tau^{z}_{\sigma,\sigma'} c_{n,i,\sigma'} \tag{5.2}$$

is the tight binding Hamiltonian for the magnetic field along the z-direction in real lattice space. Recalling that the operators $c^{\dagger}_{n,i}$ and $c_{n,i}$ are transformed as $c^{\dagger}_{n,i} = \frac{1}{\sqrt{2\pi}} \sum_k e^{-i(k\cdot i)} c^{\dagger}_{n,k}$ and $c_{n,i} = \frac{1}{\sqrt{2\pi}} \sum_k e^{i(k\cdot i)} c_{n,k}$,we can write H_Z in momentum space as

$$H_Z = \sum_{\sigma,\sigma'} \sum_{n=1}^{q} \sum_{k=1}^{N/q} c^{\dagger}_{n,k,\sigma} [B\tau^{z}_{\sigma,\sigma'} + \mu\delta_{\sigma,\sigma'}] c_{n,k,\sigma'}. \tag{5.3}$$

In order to find the dispersion relation $\epsilon(k)$, we write the Hamiltonian in matrix form as

$$H = \begin{pmatrix} c^{\dagger}_{1,k,\uparrow} & c^{\dagger}_{1,k,\downarrow} & c^{\dagger}_{2,k,\uparrow} & .... & c^{\dagger}_{q,k,\downarrow} \end{pmatrix} \boldsymbol{H}_k \begin{pmatrix} c_{1,k,\uparrow} \\ c_{1,k,\downarrow} \\ . \\ . \\ . \\ c_{q,k,\downarrow} \end{pmatrix} \tag{5.4}$$

In the following we analyse the band structure resulting from the diagonalization of $\boldsymbol{H}_k$ for different superlattice unit cells.

Figure 5.6 displays the bulk band structure when the superlattice unit cell includes an odd number of atomic sites. The magnetic field removes the Kramer degeneracy at $k = 0$ creating

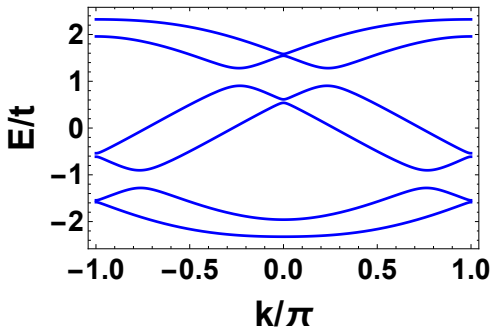

(a) Band structure q=3. B=0.2, $\alpha_r = 0.4$, $A/\lambda = 1$, $\phi = 0$.

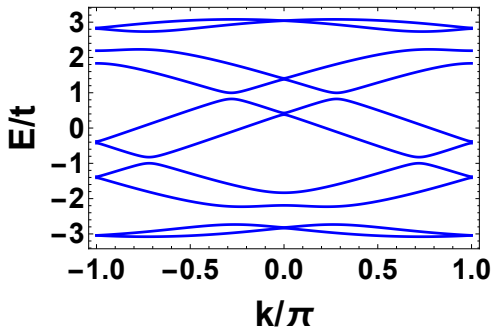

(b) Band structure q=5. $B = 0.2$, $\alpha_r = 0.7$,$A/\lambda = 1$, $\phi = 0$.

Figure 5.6: The figure shows the bulk bands for odd superlattice period. The bands are plotted in the first mBZ and they show insulating gap opening at unpinned points in the spectrum for all integer filling fractions $\nu = m/q$, $m = 1, ..., q$.

an effectively spinless regime at low energy, at filling fractions $\nu < 1/q$.
For odd periodicity of the superlattice cell, the curvature induced modulation of the Rashba SOC in the semiconductor, realizes metal-insulator transitions at unpinned points in the first mBZ at all integer filling fractions $\nu = m/q$, where $m = 1, .., q$ is an integer number.

Figure 5.7 shows the bulk bands for superlattice unit cells with even number of atomic sites. As expected, the introduction of the Time Reversal breaking term, lifting the degeneracy in $k = 0$, realizes a spinless regime in the low energy bands when $-2t - B < \mu < -2t + B$.
However, as opposite to what happens for superlattice unit cells with odd atomic sites, the competition between the magnetic field along z and the curvature induced modulation on the SOC influences the insulating gap openings in the first mBZ. In fact, the results of the previous section showed that, for an even superlattice period, no gap opening was ever possible at the filling fractions $\nu = 1/q$, $1/2$ and $(q-1)/q$, whereas, here, the introduction of the magnetic field leads to insulating gap opening in the spectrum at the filling fractions $\nu = 1/q$ and $(q-1)/q$. However, still no gap opening occurs for $\nu = 1/2$.

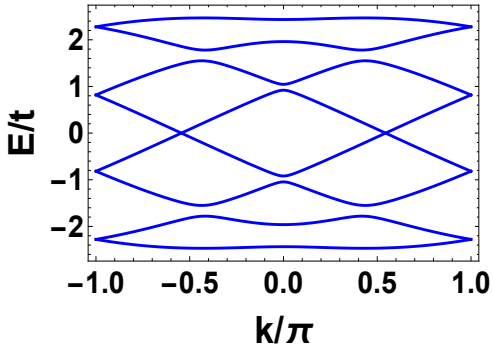

(a) Band structure $q = 4$. $B = 0.3$, $\alpha_r = 0.4$, $A/\lambda = 0.8$, $\phi = 0$.

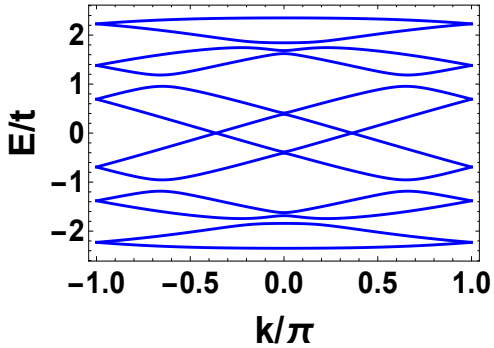

(b) Band structure q=6. $B = 0.3$, $\alpha_r = 0.4$,$A/\lambda = 0.8$, $\phi = 0$.

Figure 5.7: The figure shows the bulk bands for even superlattice period. The bands are plotted in the first mBZ and they show insulating gap opening at unpinned points in the spectrum for all integer filling fractions $\nu = m/q$, $m = 1, ..., q$, except for half-filling.

In figure 5.8 we plot the energy bands in the first mBZ with the same superlattice unit cell as the one used to plot the bands in figure 5.7, with the same values of the parameters as before, but where we change the displacement phase, from zero to $\phi = 2\pi/5$. What we observe is that adding a displacement phase does not change the situation for $q = 6$, as there is still no

insulating gap opening at half filling, meaning that those states are protected by an additional internal symmetry. On the other hand, for $q = 4$, we do observe the insulating gap opening at $\nu = 1/2$, leading us to consider the possibility that the system can be driven in a topological insulating phase by changing the parameter ϕ.
In figure 5.9 we have thus plotted the energy eigenvalues for the real lattice space BdG Hamiltonian of a finite chain with open boundary conditions, as a function of ϕ indicating the displacement phase of the atomic sites in the superlattice unit cell. As the figure shows, we obtain low-energy chiral fermionic end states after a first closing of the half filling gap at $\phi = \pi/2$, connecting the valence and the conduction bands.
With the breaking of Time Reversal, the symmetry class here drops to the to AIII complex class of Altland-Zirnbauer classification, and the topological invariant is still a Z number.

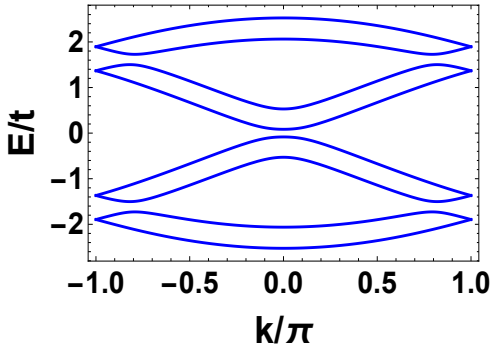

(a) Band structure $q = 4$. $B = 0.3$, $\alpha_r = 0.4$, $A/\lambda = 0.8$, $\phi = 2\pi/5$.

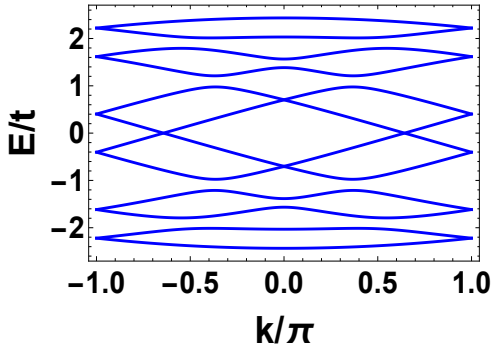

(b) Band structure q=6. $B = 0.3$, $\alpha_r = 0.4, A/\lambda = 0.8$, $\phi = 2\pi/5$.

Figure 5.8: The figure shows the bulk bands for even superlattice period. The bands are plotted in the first mBZ and they show insulating gap opening at unpinned points in the spectrum for all integer filling fractions $\nu = m/q$, $m = 1, ..., q$, except for half-filling.

5.2 Superconducting Phase

In this section, we finally analyse the full system, introducing the superconducting term in the Hamiltonian

$$H_{SC} = \Delta \sum_{n=1}^{q} \sum_{i=1}^{N/q} c^{\dagger}_{n,i,\uparrow} c^{\dagger}_{n,i,\downarrow} + h.c + \mu \sum_{\sigma,\sigma'} \sum_{n=1}^{q} \sum_{i=1}^{N/q} c^{\dagger}_{n,i,\sigma} \delta_{\sigma,\sigma'} c_{n,i,\sigma'} \tag{5.5}$$

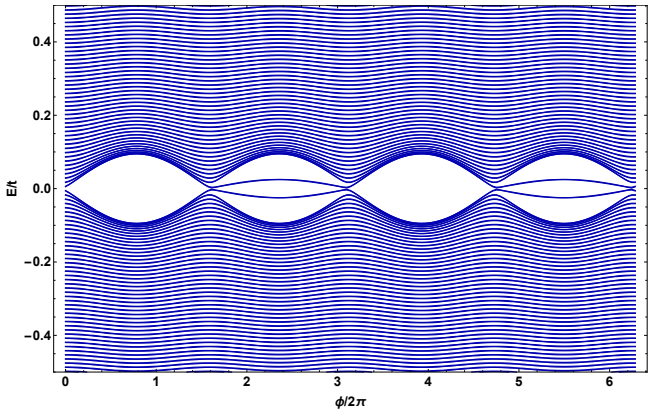

Figure 5.9: Energy eigenvalues obtained diagonalising the BdG Hamiltonian of an open, finite chain of N=600 atoms, with superlattice period λ=4a. B=0.2, α_r=0.3, A/λ=0.2.

where we have also included the chemical potential μ. The total Hamiltonian for the system is now given by $H = H_{SOC} + H_Z + H_{SC}$.
As usual, we start by analysing the bulk band structure in momentum space. From the previous section we already know H_{SOC} and H_Z after Fourier transforming. H_{SC} in momentum space reads

$$H_{SC} = \Delta \sum_{n=1}^{q} \sum_{k=1}^{N/q} c^{\dagger}_{n,k,\uparrow} c^{\dagger}_{n,k,\downarrow} + h.c. + \mu \sum_{\sigma,\sigma'} \sum_{n=1}^{q} \sum_{k=1}^{N/q} c^{\dagger}_{n,k,\sigma} \delta_{\sigma,\sigma'} c_{n,k,\sigma'} \tag{5.6}$$

At this point, we want to write the Hamiltonian in BdG matrix form $H = \boldsymbol{C}_k^{\dagger} \boldsymbol{H}_k \boldsymbol{C}_k$ where $\boldsymbol{C}_k$ is the 4q-dimensional Nambu spinor defined as

$$\boldsymbol{C}_k = \left(c_{1,k,\uparrow}, c_{1,k,\downarrow} c^{\dagger}_{1,-k,\uparrow}, c^{\dagger}_{1,-k,\downarrow}, c_{2,k,\uparrow}, ..., c^{\dagger}_{q,-k,\downarrow} \right)^T .$$

In order to find the bulk bands, we then diagonalize $\boldsymbol{H}_k$.
Having found the dispersion relation, we are interested in understanding in which point in the parameter space the bulk gap closes, signalling the presence of a topological phase transition. In the following, we analyse the phase diagram, plotting the critical line separating the trivial and the topological superconducting phases.
From the theoretical model introduced in chapter two of this thesis, we know that the gap closing happens at $k = 0$ (Γ), both at continuum and in the tight binding limit, due to Particle-Hole symmetry of the Hamiltonian. Since the modulation on SOC introduced via curvature does not affect Particle-Hole symmetry, we expect the gap closing to still occur at the Γ point in our system. We have furthermore observed that, in the low energy limit close to Γ, the two theories at continuum and at tight binding lead to the same results. This is in fact not the case for higher energies where the effects of the bandwidth in the tight binding approximation become more evident. We are therefore restricting ourselves to the lowest energy bands, more precisely, we choose the Fermi energy to always lie within the two lowest energy bands, i.e $-2t - B < \mu < -2t + B$, such that the filling fraction we consider is always $\nu < 1/2q$. This restriction is furthermore justified from the analysis of the band structure in the normal phase conducted above, where we have shown that, for both even and odd superlattice periodicity, for values of the Fermi energy within this interval, one obtains the effectively spinless regime, with only one pair of Fermi points, creating the condition for having topological superconductivity in the system (figures 5.6, 5.7 and 5.8).

Furthermore, in the analysis that follows, we choose to set $\mu = -2t$ since it is the optimal point for observing the topological phase of the system, and since the criterion for the conventional wire in this particular point has the simple form $B = \Delta$.
We hereby mention that, as analogous to what we have observed in the previous model, a modulation on the Rashba SOC induces a renormalization of the bandwidth, and $t \to \bar{t}$. Therefore, in the following, we will be careful to set $\mu = -2\bar{t}$ as the modulation of the SOC changes.

In figure 5.10 we have plotted, in the $\frac{A}{\lambda}/\Delta$ plane, the critical line separating the trivial and the topological superconducting phase. The dashed red line indicates the critical point $B = \Delta$ in which the phase transition occurs where no locally varying SOC is present. Figure 5.10(a) shows the diagram for $q = 4$ atomic sites in one unit cell, while figure 5.10(b) for $q = 5$. Because of the periodicity of the superlattice cell, the two diagram show different features.

The diagram in figure 5.10(a) is symmetric with respect to the horizontal line, at $A/\lambda = 1/2$, which, as one can see in 5.10(a) , is a peculiar line. In fact, when choosing to place four atomic sites in a unit cell, due to the form of $\theta(x_n)$ and the SOC terms, acting on the bond between nearest neighbours in the Hamiltonian 5.1 , we have that when $A/\lambda = 1/2$, the terms above are zero, leading to a total zero SOC on the system. As we can see in the diagram, the gap closing along this line occurs at $B = \Delta$ (it is on the dashed vertical line). However, because of

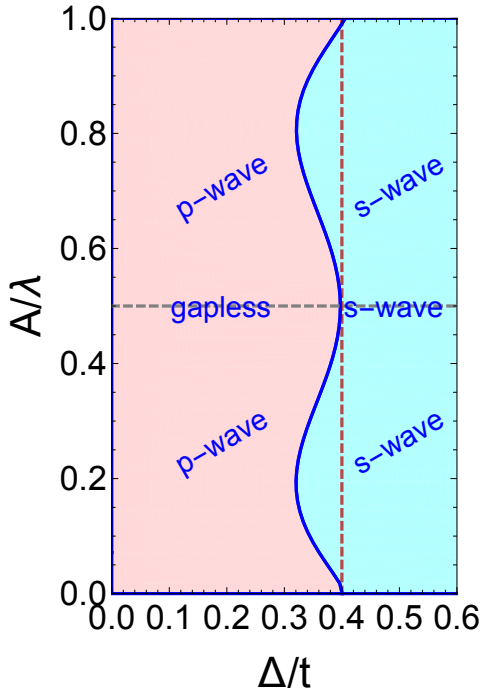

(a) Phase diagram for $q = 4$ atomic sites in a unit superlattice cell. The strength of the Rasha SOC is set at $\alpha_r/t = 0.4$

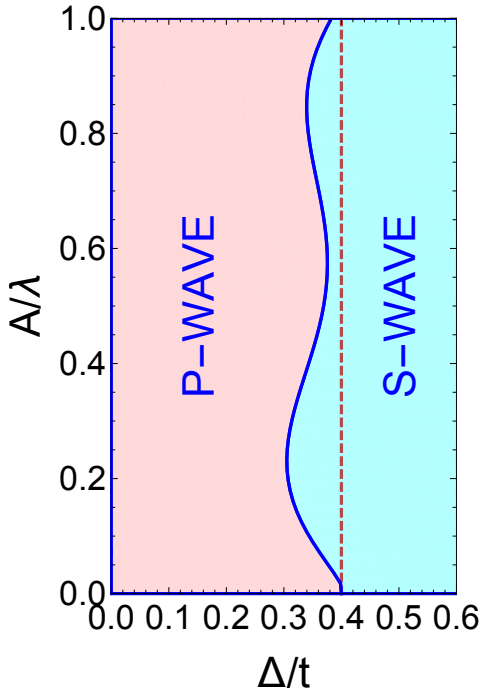

(b) Phase diagram for $q = 5$ atomic sites in a unit superlattice cell. The strength of the Rasha SOC is set at $\alpha_r/t = 0.3$

Figure 5.10: The vertical dashed line indicates the value $\Delta = B$, delimiting the regions where the system exhibits trivial superconductivity (right side) and topological superconductivity (left side) for the conventional wire. The blue lines in both graphs show the lines delimiting the two phases when the non trivial geometry of the semiconducting wire induces a local SOC modifying the phase diagram promoting trivial superconductivity for some $\Delta < B$.

the absence of spin orbit interaction, in the regime $B > \Delta$ there cannot be any superconducting gap opening, therefore the point $B = \Delta$ when $A/\lambda = 1/2$ separates the gapless semimetallic spectrum when $B > \Delta$ and the conventional s-wave gapped spectrum under the the condition $B < \Delta$.

Furthermore, the symmetry of the phase diagram in figure 5.10(a) if mirrored with respect to this line, can be explained if looking at the plots in figure 5.11 of the x and y components of the modulated SOC as a function of A/λ. In 5.11(a) we see the SOC x/y components acting on the bond between the first and the second, and the second and the third atomic sites in the unit cell; while in 5.11(b) we see the SOC component acting on the bonds between third and fourth, and fourth and first (of the neighbouring superlattice cell) atomic sites. Both the plots are symmetric with respect to $A/\lambda = 1/2$, and in fact, the graph in 5.11(b) is indeed the 5.11(a) mirrored with respect to this point.

Due to the specific form of the x and y components in the Hamiltonian 5.1, the SOC component along y is a modulated function with a constant offset, whereas the component along x is a modulated function that mediates to zero (as one can appreciate looking at the blue and red lines in 5.11). The points $A/\lambda = 1/4$ and $A/\lambda = 3/4$, where the enhancing of the trivial phase is higher, the modulated component along x has its maximum, while the component with the constant offset along y is rapidly decreasing. This fact seems to suggest that one can reach similar conclusions to the ones for the previous model: in a first approximation, one can say that the major contribution on the modified phase diagram comes from the modulated part. Despite this encouraging agreement between the two models, in order to fully understand the physical contribution of the SOC rotating in the x-y plane, a deeper analysis of the system at tight binding and continuum limit is required.

In the phase diagram for $q = 4$ there is another special point: $A/\lambda = 1$. In here, as in $A/\lambda = 0$

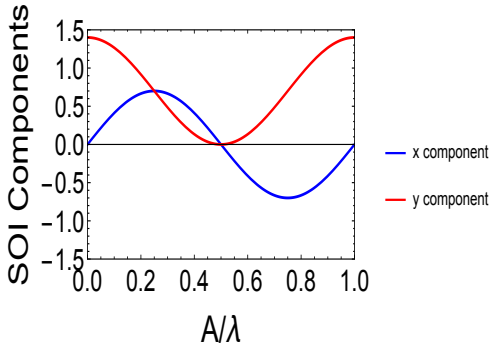

(a) Plot of the x and y components of the modulated SOC on the first and the second bonds between atomic sites inthe superlattice unit cell, as a function of A/λ.

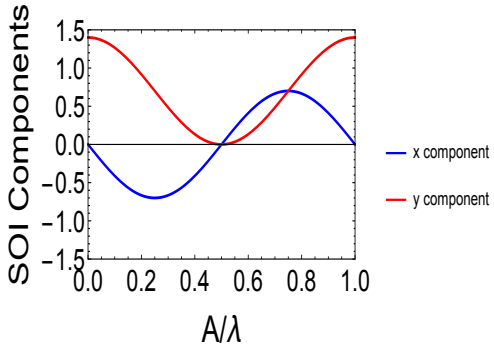

(b) Plot of the x and y components of the modulated SOC on the third and fourth bonds between atomic sites in the superlattice unit cells,as a function of A/λ.

Figure 5.11: The figure show the components along x and y on the bond between nearest neighbouring atomic sites as a function of A/λ. The parameter α_r which tunes the amplitude of the modulation on the SOC, is set at $0.7t$.

the only contribution of the SOC is along the y direction and it is constant for all the bonds, meaning that for these specific values of A/λ we recover the phase diagram of the conventional wire, without any effect of the curvature on the spin orbit coupling, and in fact, the bulk gap closes at the critical point $B = \Delta$.

The diagram for $q = 5$ atomic sites in the superlattice unit cell shows different features compared to the previous, as there is no value for A/λ in which the modulated SOC on the bonds between nearest neighbouring sites goes to zero. Thus, for no other point in the diagram except for A/λ equal zero, the gap closes for $B = \Delta$, and there is no symmetry line in the diagram. Nevertheless, the enhancing of the trivial phase still has its maximum at $A/\lambda = 1/4$.
What remains indeed a common feature of the two diagrams 5.10(a) and 5.10(b) is that the modulation on the SOC, induced by a curved shape of the semiconducting nanowire, enhances the region in the phase diagram where the system is in the trivial superconducting phase.

Another common feature between this model for the curved wire and the model analysed in the previous chapter is displayed in the figures 5.12(a) and 5.12(b) which show the same phase diagrams as above but with the different coloured lines indicating the phase transitions for different values of the Rashba SOC strength α_r. As one appreciates from the diagrams, increasing α_r amplifies the enhancement of the s-wave region.

To further verify that the enhancement of the trivial superconducting phase promoted by the curvature induced local SOC, we plot the phase diagram in the plane B/Δ.
In order to enlighten the widening of the s-wave phase, in figure 5.13 we have plotted the difference between the line $B = \Delta$ separating the trivial and the topological phase when $A/\lambda = 0$ (represented by the x-axis in the figure i.e the line) and the line separating the two phases when A/λ has a non trivial value. Here, as before, we appreciate the enhancement of the trivial phase as all the part of the diagram below the line delimiting the phase transition which was in the p-wave regime when the SOC did not have local contributions, is now s-wave.
Moreover, looking at 5.13(a) and 5.13(b), we appreciate that, as varying A/λ, the enhancement of the s-wave region is maximum when $A/\lambda = 1/4$ and then it decreases for higher values, which is consistent with the non monotonic diagram in figure 5.10. Figures 5.13(c) and 5.13(d), obtained fixing $A/\lambda = 1/4$ and varying the amplitude α_r/t, show instead that the enhancing of s-wave region increases monotonically as once increases the parameter α_r/t, in agreement once again with the trend of the different curves in 5.10.

As a last remark, we consider the curve separating the two phases in the B/Δ plane for

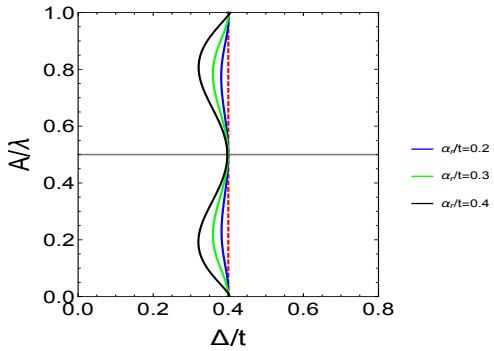

(a) Phase diagram for $q = 4$ atomic sites in a unit superlattice cell. The strength of the Rasha SOC is set at $\alpha_r/t = 0.4$

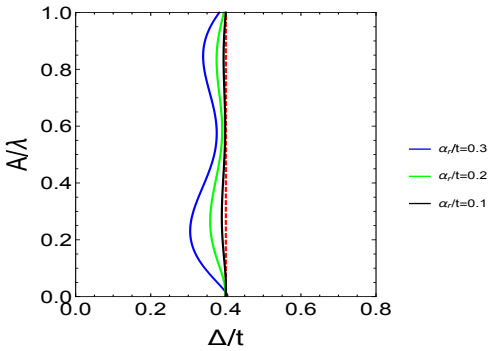

(b) Phase diagram for $q = 5$ atomic sites in a unit superlattice cell. The strength of the Rasha SOC is set at $\alpha_r/t = 0.3$

Figure 5.12: The vertical dashed line indicates the value $\Delta = B$, delimiting the regions where the system exhibits trivial superconductivity (right side) and topological superconductivity (left side) when no modulation on the SOC is introduced. The coloured lines in both graphs show the lines delimiting the two phases when the non trivial geometry of the semiconducting wire induces a local SOC modifying the phase diagram promoting trivial superconductivity for some $\Delta < B$.

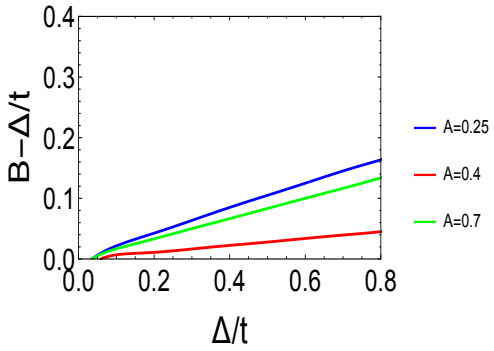

(a) Plot of the phase diagram in the plane B/Δ for q=4 atomic sites in the unit cell. Different curves are obtained varying A/λ.The amplitude of the modulation is set as $\alpha_r/t = 0.4$

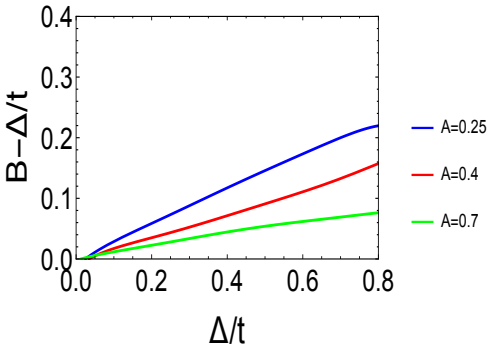

(b) Plot of the phase diagram in the plane B/Δ for q=5 atomic sites in the unit cell.The amplitude of the modulation is set as $\alpha_r/t = 0.3$

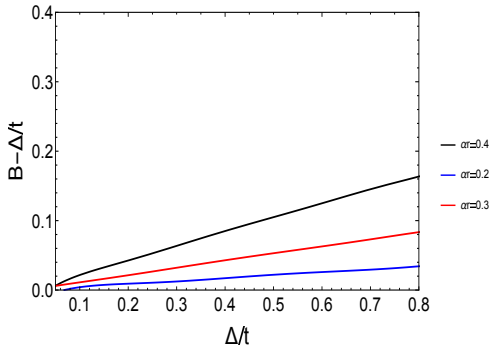

(c) Plot of the phase diagram in the plane B/Δ for q=4 atomic sites in the unit cell.The amplitude of the modulation α_r/t is varied, and $A/\lambda = 1/4$.

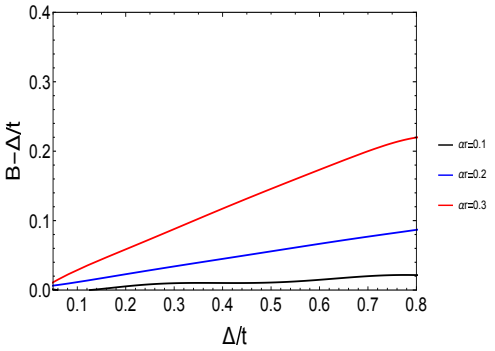

(d) Plot of the phase diagram in the plane B/Δ for q=5 atomic sites in the unit cell.The amplitude of the modulation α_r/t is varied, and $A/\lambda = 1/4$.

Figure 5.13: In figure, the diagrams showing the enhancement of the trivial phase due to the curvature induced locally varying Rashba SOC. The x-axis represents the critical line when the contribution on the SOC is only constant. When the phase transition occurs for $B = \Delta$, the plane represented in figure is all in the p-wave phase, while here, the lower part of the coloured curves is in the s-wave phase.

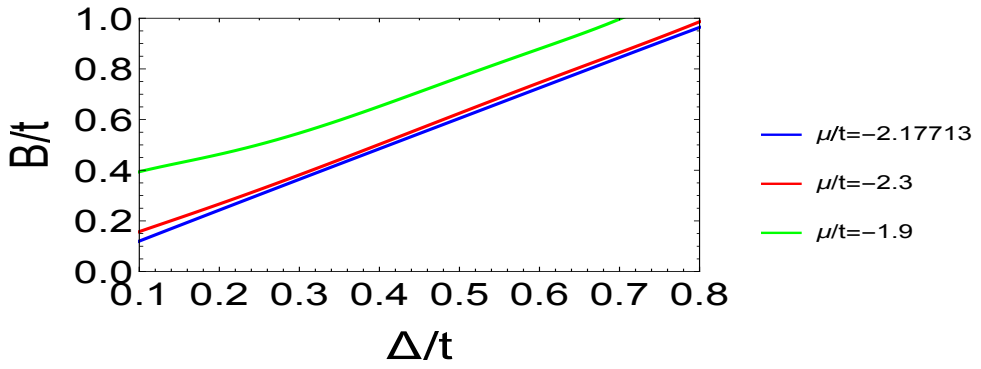

Figure 5.14: Figure shows the critical line for the topological phase transition in the plane B/Δ. The superlattice periodicity is $q = 4$ and $\alpha_r/t = 0.3$, $A/\lambda = 0.25$.

different values of the Fermi energy within the two lowest energy bands. In figure 5.14 we observe that the line separating the two phases obtained when the chemical potential μ is set at the energy value of the Kramer invariant point (which changes as one introduces a locally varying SOC as mentioned before), is the minimum of the sets of curves showing the phase diagrams at different values of the chemical potential. This implies that setting the value of the Fermi level exactly at the Kramer invariant point, represents an optimal condition for analysing the phase transition, exactly as we found for the previous model.

5.2.1 Superconducting Phase Analysed in the Open Chain

In this section, we include the plots of the eigenvalues for the open finite chain, which show the presence of Majorana zero energy modes at the ends of the chain.
Figure 5.15 is a further proof of the enlarging of the s-wave phase induced by the local canting of the spins due to the curvature. In fact, the plot obtained for $B > \Delta$ in 5.15(a) shows the gap at zero energy due to the superconducting pairing, where no zero energy odes are present, meaning that the system is still in the trivial phase, as the gap in the bulk bands has not closed yet.
However, figure 5.15(b) shows that for a higher magnetic field, the Majorana bound state localized at zero energy appear, ensuring that the transition to the toploogical phase still occurs, it just requires higher magentic field.

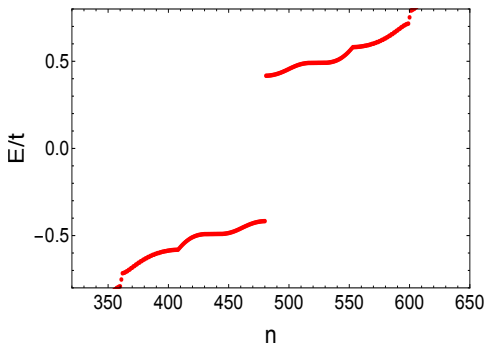

(a) Plot of the eigenvalues of the open chain. For this plot, $B/t = 0.3$ and $\Delta/t = 0.2$. The figure shows the gap at zero energy, meaning that the system is in the s-wave superonducting phase.

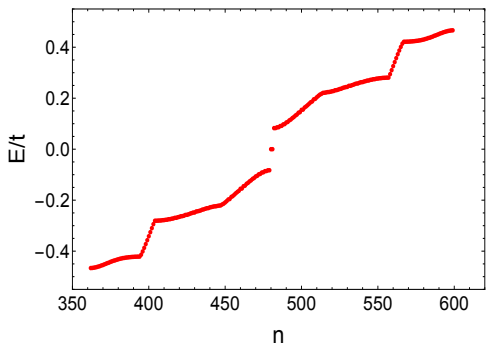

(b) Plot of the eigenvalues of the open chain. In this plot, $B/t = 0.45$ and $\Delta/t = 0.2$. In this case, we observe the Majorana bound states localized at zero energy.

Figure 5.15: The figures were obtained by diagonalizing an open chain with 240 sites, with superlattice periodicity $q = 4$.

Chapter 6

Conclusions

In the introduction we mentioned that the zero energy modes arising at the boundaries of a topological superconductor are Majorana modes. In one dimensional topological superconductors, the Majorana zero energy modes are bound states localized at the end of the chain. The Kitaev model represents a fundamental theoretical toy model for topological p-wave superconductivity in a one dimensional chain, and many ways to practically reproduce this model have been explored. In this thesis, we focused on the set up proposed in [23], constituted by a semiconductor-superconductor heterostructure in presence of an external magnetic field. The semiconductor is a 1D nanowire with Rashba spin orbit coupling, while the adjacent superconductor is a conventional bulk superconductor. In this system, it is possible to practically realize topological p-wave superconductivity in the interface between the superconductor and the semiconducting wire. We showed that the superconducting gap closes at the critical point in parameter space. Consequently, the system is driven in the topological phase, with a degenerate ground state and the zero energy modes at the ends. We derived the criterion for the gap closing, and produced a phase diagram showing the two distinct topological phases separated by the critical line.

With the purpose of understanding how the latter phase diagram is modified by considering a wire with a non trival geometric shape, we first studied the properties of this curved semiconducting wire, in presence of Rashba SOC. We found that the bent nanowire can be modelled by an effective one dimensional $\boldsymbol{k} \cdot \boldsymbol{p}$ Hamiltonian with locally varying Rashba spin orbit coupling. Before studying the system with the curvature-induced local spin canting, and in order to first understand the effect of a local SOC, we consider a simplified toy model for a straight wire with the addition of a modulated Rashba SOC along one direction. Indeed, the latter can be practically realized as the Rashba SOC can be tuned by modifying the layers of material composing the semiconductor. It is therefore possible, for example via gating, to generate an inhomogeneous electric potential, inducing a locally varying spin orbit coupling.
This model has the advantage that one can separate the contributions of the modulated and the constant Rashba SOC, which are instead difficult to disentangle when considering the curve-shaped nanowire, we therefore started by studying this toy model. By looking a the system where only a local component of the SOC was present, we have found that the s-wave (trivial) area in the phase diagram was enhanced. Indeed, we have showed that, at first order in perturbation theory, the presence of the local SOC renormalizes the g factor in the Zeeman term, decreasing the effective magnetic field experienced by the electron travelling through the semiconductor, which allows s-wave Cooper pairing for smaller values of Δ. Furthermore, the enhancing of the trivial superconducting phase is amplified as one increases the parameter controlling the strength of the constant Rashba SOC. The latter is an outstanding result since it implies that, as opposed to the case of the conventional wire, the strength of the SOC influences the occurrence of the phase transition. We conclude that, when the system for the conventional wire with additional modulated SOC is considered, the topological phase is suppressed by the presence of the modulated component of the SOC, and this suppression depends also on the

strength of the constant SOC.

When studying the model with local SOC arising from the curved geometry of the wire, we find results in agreement with the ones obtained for the previous model. In fact, the phase diagrams show the same enhancing of the trivial superconducting phase as one increases the strength of the Rashba SOC. Furthermore, a non monotonic phase diagram as a function of the curvature amplitude is obtained.

Both the dependence of the phase transition on the strength of the SOC and the non monotonic diagram have not been fully understood yet. As a future goal, we have proposed to understand such behaviours: in our ideas, the first could be understood by taking into account higher orders in perturbation theory, whereas for the second, the first step would be to study the full Hamiltonian describing the system in the continuum limit (since we have only managed to study the system at tight binding so far).

Finally, we recall that, after studying the two systems in the bulk, we diagonalized the tight binding Hamiltonian for the open chain, in order to verify the bulk edge correspondence, and we indeed find that the Majorana zero energy modes are present in the p-wave phase of the system with two-fold degenerate ground state.

Even though the analysis conducted in this thesis does not seem to suggest bent nanostructures as possible simplified ways to practically realize Majorana modes in 1D systems, we must point out that this analysis have been conducted only for specific value of the chemical potential and that the effect we observed was explained only perturbatively at low energies. Therefore, in order to make definitive assumptions on the practical implication on the observation of Majorana modes in curved nanostructures, further analysis are required.

Acknowledgements

Writing this thesis has been for me a very long journey. Looking back at the months I dedicated to this project, I can certainly say that they have been one of the most difficult and challenging period of my life. Nevertheless, in these months, I grew up as never before, I learned as never before and I got to know myself, my limits as never before, and I will be forever thankful for having this chance.
Many people played an important role during my journey, and I would like to thank all of them as if it was not for them, I would not have achieved all that I have.
At first, I would like to thank my supervisors Carmine Ortix and Niccoló Scopigno, who gave me the opportunity to start a research project within their group. I thank them for their guidance and I thank them because they were always available for me, always ready to give new advices, to show me new directions to explore, and to reply to the most stupid questions, without ever making me feel ashamed for asking them. More importantly, I thank them for understanding the tough moments I went through, and for giving me all the support they could. Apart from teaching me new physics, and always give me helpful physical insights on the topic of my research, they taught me how to face complicated situations without ever giving up or loosing the passion for what you are doing, and this lesson will accompany me for the rest of my life, no matter which path I decide to follow.
Furthermore, I would like to thank other members of their group, in particular Raffaele Battilomo, Sander Kooi and Guido van Miert, for their help and the inspiring discussions we had, and all the professors of the ITP Utrecht for the knowledge they transmit to their students every year.

Since non of this would have happened without the support of my family and my friends, I would like to thank my mother Sandra, my father Gabriele, my brother Andrea and all the friends that have been next to me during these years: both the 'old' friends back in Italy, who managed to be always present in my life despite the distance, and the 'new' friends I met in Utrecht, who were a constant support, and without whom I would never have found the strength to pursue my goals till the end.

Bibliography

[1] K. v. Klitzing, G. Dorda, and M. Pepper. New method for high-accuracy determination of the fine-structure constant based on quantized hall resistance. *Phys. Rev. Lett., vol. 45, pp. 494–497*, 1980.

[2] Pedram Roushan. *Visualizing Surface States of Topological Insulators with Scanning Tunneling Microscopy.* PhD thesis, 2011.

[3] J. M. Kosterlitz and D. J. Thouless. Ordering, metastability and phase transitions in two-dimensional systems. *Journal of Physics C: Solid State Physics, Volume 6, Number 7*, 1973.

[4] J.M. Kosterlitz and D.J. Thouless. Long range order and metastability in two dimensional solids and superfluids.(application of dislocation theory). *Journal of Physics C: Solid State Physics, vol 5, n. 11*, 1972.

[5] D. J. Thouless, M. Kohmoto, M. P. Nightingale, and M. den Nijs. Quantized hall conductance in a two-dimensional periodic potential. *American Physical Society*, 1982.

[6] M. Nakahara. *Geometry, Topology and Physics.* IOP Publishing Ltd, 2003.

[7] M. Kohmoto. Topological invariant and the quantization of the hall conductance. *Annals of Physics volume 160 issue 2*, 1985.

[8] D. J. Thouless, M. Kohmoto, M. P. Nightingale, and M. den Nijs. Quantized hall conductance in a two-dimensonal periodic potential. *Physical review letters volume 49 number 6*, 1982.

[9] J.C. Avila, Schulz-Baldes, and C. H.and Villegas-Blas. Topological invariants of edge states for periodic two-dimensional models. *Math. Phys., Anal. Geom*, 2012.

[10] Gian Michele Graf and Marcello Porta. Bulk-edge correspondence for two-dimensional topological insulators. *Communications in Mathematical Physics volume 324 issue 3*, 2013.

[11] C. L. Kane and E. J. Mele. Z 2 topological order and the quantum spin hall effect. *Phys. Rev. Lett. 95, 146802*, 2005.

[12] Z.J.Li, Y.Liu, S.C.White, P.Wahl, X.M.Xie, M.H.Jiang, and C.T.Lin. Single crystal growth and transport properties of cu-doped topological insulator bi2se3. *Physics Procedia*, 2012.

[13] G. Volovik. *The Universe in a Helium Droplet.*

[14] A.Y. Kitaev. Unpaired majorana fermions in quantum wires. *Physics-Uspekhi, 44, 131*, 2001.

[15] N. Read and D. Green. Paired states of fermions in two dimensions with breaking of parity and time-reversal symmetries and the fractional quantum hall effect. *Physical Review B*, 2000.

[16] Jason Alicea. New directions in the pursuit of majorana fermions in solid state systems. 2012.

[17] J. Alicea. Topological invariant and the quantization of the hall conductance. *Annals of Physics volume 160 issue 2*, 2013.

[18] Tudor D. Stanescu and Sumanta Tewari. Majorana fermions in semiconductor nanowires: Fundamentals, modeling and experiment. *Arxive*, May,2013.

[19] D.A Ivanov. Non-abelian statistics of half-quantum vortices in p-wave superconductors. *Physical Review Letters*, 2000.

[20] C. Nayac and M. Freedman S. Das Sarma S.H. Simon, A. Stern. Non-abelian anyons and topological quantum computation. *Reviews of Modern Physics*, 2008.

[21] Panagiotis Kotetes. Classification of engineered topological superconductors. *New Journal of Physics, Volume 15*, 2013.

[22] Ning Ma. Majorana fermions in condensed matter: An outlook. *Physica B, Volume 512*, 2017.

[23] Jay D. Sau, Sumanta Tewari, Roman M. Lutchyn, Tudor D. Stanescu, and S. Das Sarma. Non-abelian quantum order in spin-orbit-coupled semiconductors: Search for topological majorana particles in solid-state systems. *Physical Review Letters B*, 2010.

[24] Sasa Gazibegovic, Diana Car, Hao Zhang, Stijn C. Balk, John A. Logan, Michiel W. A. de Moor, Maja C. Cassidy, Rudi Schmits, Di Xu, Guanzhong Wang, Peter Krogstrup, Roy L. M. Op het Veld, Kun Zuo, Yoram Vos, Jie Shen, Daniël Bouman, Borzoyeh Shojaei, Daniel Pennachio, Joon Sue Lee, Petrus J. van Veldhoven, Sebastian Koelling, Marcel A. Verheijen, Leo P. Kouwenhoven, Chris J. Palmstrøm, and Erik P. A. M. Bakker. Epitaxy of advanced nanowire quantum devices. *Nature 548*, 2017.

[25] Konig M, Wiedmann S, Brüne C, Roth Aand Buhmann H, Molenkamp LW, and Zhang SC. Qi XL. Quantum spin hall insulator state in hgte quantum wells. *Science*, 2007.

[26] B. Andrei Bernevig, Taylor L. Hughes, and Shou-Cheng Zhang. Quantum spin hall effect and topological phase transition in hgte quantum wells. *Science, 314, 1757*, 2006.

[27] Schmidt OG1 and Eberl K. Nanotechnology. thin solid films roll up into nanotubes. *Nature*, 2001.

[28] V. Ya Prinz, Seleznev V. A., Gutakovsky A. K., Chehovskiy A. V., V. V. Preobrazhenskii, and T. A. Putyatoand, M. A. Gavrilova. Free-standing and overgrown ingaas//gaas nanotubes, nanohelices and their arrays. *Physica*, 2000.

[29] V. Ya Prinz, A. V. Chekhovskiy, V. V. Preobrazhenskii, B. R. Semyagin, and A. K. Gutakovsky. A technique for fabricating ingaas/gaas nanotubes of precisely controlled lengths. *Nanotechnology*, 2002.

[30] Charles M. Lieber. Semiconductor nanowires: A platform for nanoscience and nanotechnology. *MRS Bulletin, 36(12), 1052-1063*, 2011.

[31] P. Gentile, M. Cuoco, and Carmine Ortix. Edge states and topological phases generated by curving a nanowire with rashba spin-orbit coupling. *Physical Review Letters*, 2015.

[32] Peter Kes Dirk Van Delft. The discorvery of superconductivity. *Physics Today*, 2010.

[33] L. Cooper. Bound electron pairs in a degenerate fermi gas. *Physical review journals archive*, 1956.

[34] H. Bruus and K: Flensberg. *Many Body Quantum Theory in Condensed Matter PHysics.*

[35] S. Bachmann, W. De Roeck, and M. Fraas. Adiabatic theorem for quantum spin systems. *Physical Review Letters*, 2017.

[36] Alexander Altland and Martin R. Zirnbauer. Nonstandard symmetry classes in mesoscopic normal-superconducting hybrid structures. *The American Physical Society*, 1997.

[37] Alexei Kitaev. Periodic table for topological insulators and superconductors. *arXiv*, 2009.

[38] A. Kitaev. Unpaired majorana fermions in quantum wires. *Physics-Uspekhi, Volume 44*, 2000.

[39] G. Moore and N. Read. Nonabelions in the fractional quantum hall effect. *Nuclear Physics B*, 1991.

[40] Roman M. Lutchyn, Jay D. Sau, and S. Das Sarma. Majorana fermions and a topological phase transition in semiconductor-superconductor heterostructures. *arXiv*, 2010.

[41] V. Ya Prinz, V. A. Seleznev, Gutakovsky, and V. V.and Putyato M. A.and Gavrilova T. A. Chehovskiy, A. V.and Preobrazhenskii. Free-standing and overgrown ingaas//gaas nanotubes, nanohelices and their arrays. *Physica E: Low-dimensional Systems and Nanostructures, Volume 6, Issue 1, p. 828-831.*, 2000.

[42] Oliver G. Schmidt. Thin solid films roll up into nanotubes. *Nature*, 2001.

[43] Paola Gentile, Mario Cuoco, and Carmine Ortix. Curvature-induced rashba spin-orbit interaction in strain-driven nanostructures. *SPIN Vol 03 No 03*, 2013.

[44] L. H. Thomas. The motion of the spinning electron. *Nature, vol 117*, 1926.

[45] E. Wigner. On unitary representations of the inhomogeneous lorentz group. *Annals of Mathematics, vol 40*, 1939.

[46] P.O. Löwdin. Studies in perturbation theory. X. Lower bounds to energy eigenvalues in perturbation-theory ground state. *Physical Review Journal archive*, 1965.

[47] E.O. Kane. Energy band structure in p-type germanium and silicon. *Journal of Physics and Chemistry of solids*, 1956.

[48] E.O. Kane. Band structure of indium antimonide. *Journal of Physics and Chemistry of Solids*, 1957.

[49] Carmine Ortix. Quantum mechanics of a spin-orbit coupled electron constrained to a space curve. *Physical Review letters*, 2015.

[50] H. Jensen and H. Koppe. Quantum mechanics with constraints. *Annals of Physics 63, 586-591*, 1971.

[51] R. C. T. da Costa. Quantum mechanics of a constrained particle. *Phys. Rev. A 23, 1982*, 1981.

[52] Giulio Ferrari and Giampaolo Cuoghi. Schrödinger equation for a particle on a curved surface in an electric and magnetic field. *Phys. Rev. Lett. 100, 230403*, 2008.

[53] Carmine Ortix, Suwit Kiravittaya, Oliver G. Schmidt, and Jeroen van den Brink. Curvature-induced geometric potential in strain-driven nanostructures. *Phys. Rev. B 84, 045438*, 2011.

[54] Dirk J. Struik. *Lectures on Classical Differential Geometry.* Dover Publications Inc, Massachusetts Institute of Technology, 1988.

[55] Sean Carroll. *Spacetime and Geometry: An Introduction to General Relativity.* Pearson, 2013.

[56] Pei-Qing Jin, You-Quan Li, and Fu-Chun Zhang. Su(2)xu(1) unified theory for charge, orbit and spin currents. *J. Phys. A: Math. Gen. 39 (2006) 7115-7123*, 2006.

[57] M.S Shikakhwa. Pure gauge spin-orbit couplings. *The European Physics Journal Plus*, 2016.

[58] M. A. H. Vozmediano, M.I. Katsnelson, and F. Guinea. Gauge fields in graphene. *Physics Reports 496, 109*, 2010.

[59] Bertrand Berche, Nelson Bolívar, Alexander López, and Ernesto Medina. SU(2) x U(1) unified theory for charge, orbit and spin currents. *Physics of Condensed Matter*, 2015.

Appendix A

Diagonalization of the BdG Hamiltonian

In here we include some details about the diagonalisation of

$$H_{BdG} = \boldsymbol{\Psi}_{\boldsymbol{k}}^{\dagger} \boldsymbol{H}_{\boldsymbol{k}} \boldsymbol{\Psi}_{\boldsymbol{k}}. \tag{A.1}$$

The Bogoliubov operators are defined via unitary transformation as

$$\begin{pmatrix} \alpha_{\boldsymbol{k},\uparrow} \\ \alpha_{-\boldsymbol{k},\downarrow}^{\dagger} \end{pmatrix} = \begin{pmatrix} u_{\boldsymbol{k}}^{*} & v_{\boldsymbol{k}} \\ -v_{\boldsymbol{k}}^{*} & u_{\boldsymbol{k}} \end{pmatrix} \begin{pmatrix} c_{\boldsymbol{k},\uparrow} \\ c_{-\boldsymbol{k},\downarrow}^{+} \end{pmatrix}$$

where

$$\boldsymbol{U}^{-1} = \begin{pmatrix} u_{\boldsymbol{k}}^{*} & v_{\boldsymbol{k}} \\ -v_{\boldsymbol{k}}^{*} & u_{\boldsymbol{k}} \end{pmatrix}.$$

Applying the unitary transformation to the Matrix form of the Hamiltonian above we have

$$H_{BdG} = \boldsymbol{\Psi}_{\boldsymbol{k}}^{\dagger} \boldsymbol{U}\boldsymbol{U}^{\dagger} \boldsymbol{H}_{\boldsymbol{k}} \boldsymbol{U}\boldsymbol{U}^{\dagger} \boldsymbol{\Psi}_{\boldsymbol{k}}$$

which is equivalent to

$$H_{MF} = \begin{pmatrix} \alpha_{\boldsymbol{k},\uparrow}^{\dagger} & \alpha_{-\boldsymbol{k},\downarrow} \end{pmatrix} \begin{pmatrix} u_{\boldsymbol{k}}^{*} & v_{\boldsymbol{k}} \\ -v_{\boldsymbol{k}}^{*} & u_{\boldsymbol{k}} \end{pmatrix} \begin{pmatrix} \epsilon_{\boldsymbol{k}} & \Delta \\ \Delta^{*} & -\epsilon_{\boldsymbol{k}} \end{pmatrix} \begin{pmatrix} u_{\boldsymbol{k}} & -v_{\boldsymbol{k}} \\ v_{\boldsymbol{k}}^{*} & u_{\boldsymbol{k}}^{*} \end{pmatrix} \begin{pmatrix} \alpha_{\boldsymbol{k},\uparrow} \\ \alpha_{-\boldsymbol{k},\downarrow}^{+} \end{pmatrix}$$

for the unitarity of the transformation.
From linear algebra we thus have the identity

$$\boldsymbol{U}_{\boldsymbol{k}}^{\dagger} \boldsymbol{H}_{\boldsymbol{k}} \boldsymbol{U}_{\boldsymbol{k}} = \boldsymbol{D}$$

which in our case reads

$$\begin{pmatrix} u_{\boldsymbol{k}}^{*} & v_{\boldsymbol{k}} \\ -v_{\boldsymbol{k}}^{*} & u_{\boldsymbol{k}} \end{pmatrix} \begin{pmatrix} \epsilon_{\boldsymbol{k}} & \Delta \\ \Delta^{*} & -\epsilon_{\boldsymbol{k}} \end{pmatrix} \begin{pmatrix} u_{\boldsymbol{k}} & -v_{\boldsymbol{k}} \\ v_{\boldsymbol{k}}^{*} & u_{\boldsymbol{k}}^{*} \end{pmatrix} = \begin{pmatrix} \lambda_{1\boldsymbol{k}} & 0 \\ 0 & \lambda_{2\boldsymbol{k}} \end{pmatrix}.$$

In the previous, the $\lambda_{1,2\boldsymbol{k}}$ are the eigenvalues of the matrix $\boldsymbol{H}_k$ which can be easily shown to be the 2.8: $\lambda_{\boldsymbol{k}} = \pm\sqrt{\epsilon_{\boldsymbol{k}}^2 + |\Delta|^2}$.
The $\lambda_{1,2\boldsymbol{k}}$ give the excitation spectrum of the Hamiltonian in terms of the Bogoliubov quasiparticles operators $\alpha_{\boldsymbol{k}}$ and $\alpha_{\boldsymbol{k}}^{\dagger}$. Solving for the eigenvectors of the problem, recalling $\lambda_{1\boldsymbol{k}} = -\lambda_{2\boldsymbol{k}}$, we find

$$\begin{aligned} u_{\boldsymbol{k}} &= \frac{\Delta}{(\epsilon_{\boldsymbol{k}} - \lambda_{\boldsymbol{k}})} v_{\boldsymbol{k}}^{*} \\ u_{\boldsymbol{k}}^{*} &= -\frac{(\epsilon_{\boldsymbol{k}} + \lambda_{\boldsymbol{k}})}{\Delta} v_{\boldsymbol{k}} \end{aligned} \tag{A.2}$$

Combining this with the normalization relation $|u_{\boldsymbol{k}}|^2 + |v_{\boldsymbol{k}}|^2 = 1$, we obtain the relations 2.7

$$|u_{\boldsymbol{k}}|^2 = \frac{1}{2}\left(1 + \frac{\epsilon_{\boldsymbol{k}}}{\lambda_{\boldsymbol{k}}}\right); |v_{\boldsymbol{k}}|^2 = \frac{1}{2}\left(1 - \frac{\epsilon_{\boldsymbol{k}}}{\lambda_{\boldsymbol{k}}}\right) \tag{A.3}$$

Appendix B

Finite Differences method to derive the tight binding Hamiltonian

In here we go through the discretization of the Hamiltonian 3.36 explicitly using the finite differences formula

$$\Delta_a f(x) = \frac{f(x+a) - f(x-a)}{2a} \tag{B.1}$$

for each term appearing in the Hamiltonian.
We start with the kinetic term

$$H_{kin} = \int ds \Psi^\dagger(s) \frac{\partial_s^2}{2m^*} \Psi(s)\}, \tag{B.2}$$

which contains a second order derivative, thus applying the formula $B.1$ at second order and setting the lattice spacing $a = 1$, the $B.2$ becomes

$$H_{kin} = -t \sum_i \Psi_i^\dagger \Psi_{i+1} + \Psi_i^\dagger \Psi_{i-1} = -t \sum_i \Psi_i^\dagger \Psi_{i+1} + h.c \tag{B.3}$$

where t is the hopping term defined as $t = \frac{\hbar^2}{2m^*}$
Note that in the previous, we have omitted the spin indexes, and since the kinetic energy does not act on spin space, the term above just comes with a $\delta_{\sigma,\sigma'}$.
Let us now consider the spin-orbit coupling term

$$H_{SOI} = -\frac{i\alpha_r}{2} \sum_{\sigma,\sigma'} \int ds \Psi^\dagger(s)_{\sigma,\sigma'} [\tau_N(s)\partial_s + \partial_s \tau_N(s)] \Psi(s)_{\sigma,\sigma'} \tag{B.4}$$

Recalling $\widehat{\boldsymbol{N}}(s) = \{\cos\theta(s), \sin\theta(s), 0\}$ and $\boldsymbol{\tau}$ is the vector of the Pauli matrices, we have in the preceding

$$\begin{aligned} H_{SOI} = -\frac{i\alpha_r}{2} \sum_{\sigma,\sigma'} \int ds \Psi^\dagger(s)_{\sigma,\sigma'} [\tau_x(\cos\theta(s)\partial_s + \partial_s \cos\theta(s)) \\ + \tau_y(\sin\theta(s)\partial_s + \partial_s \sin\theta(s))] \Psi(s)_{\sigma,\sigma'}. \end{aligned} \tag{B.5}$$

In order to discretize the term containing the derivative of a product, we use the product formula for the finite difference, which reads

$$\Delta(f \cdot g) = f\Delta g + g\Delta f + \Delta f \Delta g \tag{B.6}$$

this is the same formula we also use to discretize the product appearing in Hamiltonian 4.1 for the model describing a wire with externally modulated Rashba SOC. the term in τ_x after

applying the finite differences formula reads

$$\sum_{\sigma,\sigma'}\sum_{i}\Psi^{\dagger}_{i,\sigma,\sigma'}\tau_x[\sin\theta_i\frac{(\Psi_{i+1,\sigma,\sigma'})+\Psi_{i-1,\sigma,\sigma'}}{2}+\frac{(\sin\theta_{i+1}\Psi_{i+1,\sigma,\sigma'})+(\sin\theta_{i-1}\Psi_{i-1,\sigma,\sigma'})}{2}]$$
$$=\sum_{\sigma,\sigma'}\sum_{i}\Psi^{\dagger}_{i,\sigma,\sigma'}\tau_x\left[\frac{(\sin\theta_i+\sin\theta_{i+1})}{2}\right]\Psi_{i+1,\sigma,\sigma'}+h.c \tag{B.7}$$

the term in τ_y is obtained in the exact same way and it reads

$$\sum_{\sigma,\sigma'}\sum_{i}\Psi^{\dagger}_{i,\sigma,\sigma'}\tau_y\left[\frac{(\cos\theta_i+\cos\theta_{i+1})}{2}\right]\Psi_{i+1,\sigma,\sigma'}+h.c. \tag{B.8}$$

the terms in between the square brackets in $B.7$ and τy express the strength and the direction in the x,y plane of the Rashba SOI on the bond between nearest neighbouring atomic sites. Now let us recall from 3.38 and 3.39 can determine $\theta(s)$ as

$$\theta(s)=-\int^{s}\kappa(s^{'})ds^{'}=A\left(\frac{2\pi}{\lambda}\right)^2\int^{s}\sin\frac{2\pi s^{'}}{\lambda}ds^{'}=-\frac{A}{\lambda}2\pi\cos\frac{2\pi s}{\lambda}. \tag{B.9}$$

When discretizing, $\theta(s)\to\theta_i$, where the i indicate the atomic positions on the lattice. Thus, the full SOI term in discrete space reads

$$H_{SOI}=-\frac{i\alpha_r}{2}\sum_{\sigma,\sigma'}\sum_{i}\Psi^{\dagger}_{i,\sigma,\sigma'}\tau_y\left[\frac{(\cos\theta_i+\cos\theta_{i+1})}{2}\right]\Psi_{i+1,\sigma,\sigma'}$$
$$+\Psi^{\dagger}_{i,\sigma,\sigma'}\tau_x\left[\frac{(\sin\theta_i+\sin\theta_{i+1})}{2}\right]\Psi_{i+1,\sigma,\sigma'}+h.c. \tag{B.10}$$

With this notation, the tight binding Hamiltonian reads

$$H=-t\sum_{\sigma,\sigma'}\sum_{i}\Psi^{\dagger}_{i,\sigma}\Psi_{i+1,\sigma'}\delta_{\sigma,\sigma'}-\frac{i\alpha_r}{2}\sum_{\sigma,\sigma'}\sum_{i}\Psi^{\dagger}_{i,\sigma,\sigma'}\tau_y\left[\frac{(\cos\theta_i+\cos\theta_{i+1})}{2}\right]\Psi_{i+1,\sigma,\sigma'}$$
$$+\Psi^{\dagger}_{i,\sigma,\sigma'}\tau_x\left[\frac{(\sin\theta_i+\sin\theta_{i+1})}{2}\right]\Psi_{i+1,\sigma,\sigma'}+h.c. \tag{B.11}$$

Appendix C

Matrix Form of the momentum space tight binding Hamiltonians

In here we write down the explicit matrix form of the matrix H_k for the two models described in chapter three for superlattice periodicities $q = 3$ and $q = 4$, when the total Hamiltonian reads $H = \sum_k \boldsymbol{C}_k H_k \boldsymbol{C}_k$ and the vector $\boldsymbol{C}$ is defined as in the chapter:

$$\boldsymbol{C}_k = \left(c_{n_1,k,\uparrow}, c_{n_1,k,\downarrow}, c_{n_2,k,\uparrow}, ..., c_{n_q,k,\downarrow}\right)^T \tag{C.1}$$

Starting from the momentum space tight binding Hamiltonian of the serpentine-shaped wire 3.45 and putting it in matrix form as above, the explicit form for $q = 3$ reads .

$$\begin{pmatrix} 0 & 0 & -t & \alpha_r\Lambda - e^{ik}t & -e^{ik}t & -e^{ik}\alpha_r[\Lambda^*+\beta] \\ 0 & 0 & -\alpha_r\Lambda & -t & e^{ik}t\alpha_r[\Lambda^*+\beta] & -e^{ik}t \\ -t & -\alpha_r\Lambda & 0 & 0 & -t & \alpha_r[\Lambda+\beta] \\ \alpha_r\Lambda^* & -t & 0 & 0 & -\alpha_r[\Lambda^*+\beta] & -t \\ -e^{-ik}t & e^{-ik}\alpha_r[\Lambda+\beta] & -t & -\alpha_r[\Lambda^*+\beta] & 0 & 0 \\ -e^{-ik}\alpha_r[\Lambda+\beta] & -e^{-ik}t & \alpha_r[\Lambda^*+\beta] & -t & 0 & 0 \end{pmatrix}. \tag{C.2}$$

where $\Lambda = 2(\cos(\pi A) + i\sin(\pi A))$ and $\beta = (\cos(2\pi A) - \sin(2\pi A))$.

For $q = 4$ it is instead given by

$$\begin{pmatrix} 0 & 0 & -t & +\alpha_r\Lambda & 0 & 0 & -e^{ik}t & -\alpha_r e^{ik}\Lambda \\ 0 & 0 & -\alpha_r\Lambda^* & -t & 0 & 0 & -\alpha_r e^{ik}\Lambda^* & -e^{ik}t \\ -t & -\alpha_r\Lambda & 0 & 0 & -t & \alpha_r\Lambda & 0 & 0 \\ \alpha_r\Lambda^* & -t & 0 & 0 & -\alpha_r\Lambda^* & -t & 0 & 0 \\ 0 & 0 & -t & -\alpha_r\Lambda & 0 & 0 & -t & \alpha_r\Lambda^* \\ 0 & 0 & \alpha_r\Lambda^* & -t & 0 & 0 & -\alpha_r\Lambda^* & -t \\ -e^{-ik}t & e^{-ik}\alpha_r\Lambda^* & 0 & 0 & -t & -\alpha_r\Lambda & 0 & 0 \\ -e^{-ik}\alpha_r\Lambda^* & -e^{-ik}t & 0 & 0 & \alpha_r\Lambda & -t & 0 & 0 \end{pmatrix}. \tag{C.3}$$

where we have defined $\Lambda = 1 + \cos(2\pi A) + i\sin(2\pi A)$

The matrix form for the tight binding Hamiltonian in k-space of the wire with two orthogonal Rashba SOC, a constant one along the y-direction and the externally modulated one along the z-direction, is obtained by re-writing the 4.3 in terms of the vector C.1. The explicit form of H_k for $q = 3$ is given by

$$\begin{pmatrix} 0 & 0 & -t - \frac{i\alpha_m}{2} & -\alpha_r & -e^{ik}t - \frac{1}{4}e^{ik}\alpha_m & e^{ik}\alpha_r \\ 0 & 0 & \alpha_r & -t + \frac{i\alpha_m}{2} & -e^{ik}\alpha_r & -e^{ik}t + \frac{1}{4}e^{ik}\alpha_m \\ -t + \frac{i\alpha_m}{2} & \alpha_r & 0 & 0 & -t + \frac{i\alpha_m}{4} & -\alpha_r \\ -\alpha_r & -t - \frac{i\alpha_m}{2} & 0 & 0 & \alpha_r & -t - \frac{i\alpha_m}{4} \\ -e^{-ik}t + \frac{1}{4}e^{-ik}\alpha_m & -e^{-ik}\alpha_r & -t - \frac{i\alpha_m}{4} & \alpha_r & 0 & 0 \\ e^{-ik}\alpha_r & -e^{-ik}t - \frac{1}{4}e^{-ik}\alpha_m & \alpha_r & -t + \frac{i\alpha_m}{4} & 0 & 0 \end{pmatrix}. \tag{C.4}$$

For $q = 4$ is given by .

$$\begin{pmatrix}
0 & 0 & -t-\frac{i\alpha_m}{2} & -\alpha_r & 0 & 0 & -e^{ik}t-\frac{i}{2}e^{ik}\alpha_m & e^{ik}\alpha_r \\
0 & 0 & \alpha_r & -t+\frac{i\alpha_m}{2} & 0 & 0 & -e^{ik}\alpha_r & -e^{ik}t+\frac{i}{2}e^{ik}\alpha_m \\
-t+\frac{i\alpha_m}{2} & \alpha_r & 0 & 0 & -t-\frac{i\alpha_m}{2} & -\alpha_r & 0 & 0 \\
-\alpha_r & -t-\frac{i\alpha_m}{2} & 0 & 0 & \alpha_r & -t+\frac{i\alpha_m}{2} & 0 & 0 \\
0 & 0 & -t+\frac{i\alpha_m}{2} & \alpha_r & 0 & 0 & -t+\frac{i\alpha_m}{2} & -\alpha_r \\
0 & 0 & -\alpha_r & -t-\frac{i\alpha_m}{2} & 0 & 0 & \alpha_r & -t-\frac{i\alpha_m}{2} \\
-e^{-ik}t+\frac{i}{2}e^{-ik}\alpha_m & -e^{-ik}\alpha_r & 0 & 0 & -t-\frac{i\alpha_m}{2} & \alpha_r & 0 & 0 \\
e^{-ik}\alpha_r & -e^{-ik}t-\frac{i}{2}e^{-ik}\alpha_m & 0 & 0 & -\alpha_r & -t+\frac{i\alpha_m}{2} & 0 & 0
\end{pmatrix} \tag{C.5}$$

Note that in all the preceding, we have set $\phi = 0$ for simplicity.